

*MRBP official file copy
Do Not Remove*

AFWAL-TR-85-4013

ADA165065



THE AXIAL COMPRESSIVE STRENGTH OF HIGH PERFORMANCE POLYMER
FIBERS (U)

S. J. DeTeresa

University of Massachusetts
Amherst, MA 01003

March 1985

Interim Report for Period March 1982 - December 1984

Approved for public release; distribution unlimited.

MATERIALS LABORATORY
AIR FORCE WRIGHT AERONAUTICAL LABORATORIES
AIR FORCE SYSTEMS COMMAND
WRIGHT-PATTERSON AIR FORCE BASE, OHIO 45433


Best Available Copy

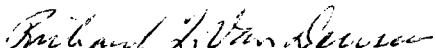
20040218345

When Government drawings, specifications, or other data are used for any purpose other than in connection with a definitely related Government procurement operation, the United States Government thereby incurs no responsibility nor any obligation whatsoever; and the fact that the Government may have formulated, furnished, or in any way supplied the said drawings, specifications, or other data, is not to be regarded by implication or otherwise as in any manner licensing the holder or any other person or corporation, or conveying any rights or permission to manufacture use, or sell any patented invention that may in any way be related thereto.


This report has been reviewed by the Office of Public Affairs (ASD/PA) and is releasable to the National Technical Information Service (NTIS). At NTIS, it will be available to the general public, including foreign nationals.

This technical report has been reviewed and is approved for publication.


WALTER W. ADAMS
Project Scientist


RICHARD L. VAN DEUSEN
Chief, Polymer Branch

FOR THE COMMANDER


ROBERT L. RAPSON, Acting Chief
Nonmetallic Materials Division

"If your address has changed, if you wish to be removed from our mailing list, or if the addressee is no longer employed by your organization please notify AFWAL/MLBP, Wright-Patterson AFB OH 45433 to help us maintain a current mailing list."

Copies of this report should not be returned unless return is required by security considerations, contractual obligations, or notice on a specific document.

Unclassified

SECURITY CLASSIFICATION OF THIS PAGE

REPORT DOCUMENTATION PAGE

1a. REPORT SECURITY CLASSIFICATION Unclassified			1b. RESTRICTIVE MARKINGS										
2a. SECURITY CLASSIFICATION AUTHORITY			3. DISTRIBUTION/AVAILABILITY OF REPORT Unlimited										
2b. DECLASSIFICATION/DOWNGRADING SCHEDULE													
4. PERFORMING ORGANIZATION REPORT NUMBER(S)			5. MONITORING ORGANIZATION REPORT NUMBER(S) AFWAL-TR-85-4013										
6a. NAME OF PERFORMING ORGANIZATION Univ of Massachusetts		6b. OFFICE SYMBOL (If applicable)	7a. NAME OF MONITORING ORGANIZATION Materials Laboratory (AFWAL/MLBP)										
6c. ADDRESS (City, State and ZIP Code) Polymer Science and Engineering Dept Amherst, MA 01003			7b. ADDRESS (City, State and ZIP Code) AFWAL/MLBP Wright-Patterson AFB OH 45433										
8a. NAME OF FUNDING/SPONSORING ORGANIZATION Materials Laboratory		8b. OFFICE SYMBOL (If applicable)	9. PROCUREMENT INSTRUMENT IDENTIFICATION NUMBER F33615-82-5068										
8c. ADDRESS (City, State and ZIP Code) AFWAL/MLBP Wright-Patterson AFB OH 45433			10. SOURCE OF FUNDING NOS. <table border="1"><thead><tr><th>PROGRAM ELEMENT NO.</th><th>PROJECT NO.</th><th>TASK NO.</th><th>WORK UNIT NO.</th></tr></thead><tbody><tr><td>62102F</td><td>2419</td><td>01</td><td>40</td></tr></tbody></table>		PROGRAM ELEMENT NO.	PROJECT NO.	TASK NO.	WORK UNIT NO.	62102F	2419	01	40	
PROGRAM ELEMENT NO.	PROJECT NO.	TASK NO.	WORK UNIT NO.										
62102F	2419	01	40										
11. TITLE (Include Security Classification) The Axial Compressive Strength of High													
12. PERSONAL AUTHOR(S) S. J. DeTeresa													
13a. TYPE OF REPORT Interim		13b. TIME COVERED FROM Mar 82 TO Dec 84		14. DATE OF REPORT (Yr., Mo., Day) March 1985									
15. PAGE COUNT 201													
16. SUPPLEMENTARY NOTATION													
17. COSATI CODES <table border="1"><thead><tr><th>FIELD</th><th>GROUP</th><th>SUB. GR.</th></tr></thead><tbody><tr><td>7</td><td>3</td><td>1</td></tr><tr><td>11</td><td>5</td><td>3</td></tr></tbody></table>			FIELD	GROUP	SUB. GR.	7	3	1	11	5	3	18. SUBJECT TERMS (Continue on reverse if necessary and identify by block number) Ordered Polymer PBT Fiber Compressive Strength PPTA Fiber Graphite Fiber Torsion Kink Band	
FIELD	GROUP	SUB. GR.											
7	3	1											
11	5	3											
19. ABSTRACT (Continue on reverse if necessary and identify by block number) <p>An experimental and theoretical study of the axial compressive strengths of high performance polymer fibers is undertaken. Compressive failure of these fibers manifests itself as kink band formation. Techniques permitting the application of small, measurable axial compressive strains to initiate kink banding in fine fibers are introduced. Tensile tests of compressively kinked poly(p-phenylene terephthalamide) (PPTA) fibers reveal only a 10% loss in tensile strength after application of compressive strains much greater than the critical strain required for kink band initiation.</p> <p>The concepts of compressive failure due to elastic microbuckling instabilities in axially compressed extended-chain polymers is proposed. Highly oriented polymer fibers are treated as a laterally interacting collection of fully extended chains. The critical stress required to buckle this collection of chains is calculated to be equal to the minimum longitudinal shear modulus of the fiber. This critical compressive strength is used as a predic-</p>													
20. DISTRIBUTION/AVAILABILITY OF ABSTRACT UNCLASSIFIED/UNLIMITED <input checked="" type="checkbox"/> SAME AS RPT. <input checked="" type="checkbox"/> DTIC USERS <input type="checkbox"/>			21. ABSTRACT SECURITY CLASSIFICATION Unclassified										
22a. NAME OF RESPONSIBLE INDIVIDUAL W. W. Adams			22b. TELEPHONE NUMBER (Include Area Code) (513) 255-9148	22c. OFFICE SYMBOL AFWAL/MLBP									

11. Performance Polymers

tion of the limiting value of fiber compressive strength.

An excellent linear correlation between axial compressive strength and torsion modulus is measured for four extended-chain polymer fibers and for a graphite fiber. These fibers exhibit compressive strengths equal to approximately one-third of their respective torsion moduli.

The relationship between torsion strains and axial normal strains in high performance polymer fibers is also investigated. Torsion of these fibers is found to result in axial contraction, a second-order effect. This axial contraction with twist results in internal axial stresses sufficient to cause compressive failure (kink banding) of the core of the polymer fibers. Furthermore, the length contraction with twist causes a measurable linear increase in torsion modulus with applied axial tensile stress. Consideration of the effect that axial compressive stress has on the fiber torsion modulus leads to the conclusion that an elastic shear instability occurs at a compressive stress equal to the fiber longitudinal shear modulus, the same prediction of compressive strength obtained from elastic microbuckling analysis.

TABLE OF CONTENTS

Chapter		
I.	INTRODUCTION.....	1
1.1	High Performance Organic Fibers for Composite Reinforcement.....	1
1.2	Dissertation Overview.....	5
II.	COMPRESSIVE BEHAVIOR OF POLY(P-PHENYLENE TEREPHTHALAMIDE) FIBERS.....	8
2.1	Background.....	8
2.2	Experimental.....	12
2.3	Results.....	18
2.4	Discussion.....	26
2.5	Conclusions.....	33
III.	AN ELASTIC MICROBUCKLING THEORY TO PREDICT THE AXIAL COMPRESSIVE STRENGTHS OF EXTENDED-CHAIN POLYMERS.....	34
3.1	Background.....	34
3.2	The Energy Method for Determination of Elastic Stability.....	39
3.3	Rigid-Link Elastic-Hinge Model for a Single Extended Polymer Chain.....	46
3.4	Approximate Buckling Load Formula for Long Link-Hinge Chains.....	52
3.5	Buckling of Laterally Interacting Link-Hinge Chains: Predictions of High Performance Fiber Compressive Strength.....	61
3.6	Summary.....	68
IV.	THEORETICAL AND MEASURED AXIAL COMPRESSIVE STRENGTHS OF HIGH PERFORMANCE POLYMER FIBERS.....	70
4.1	Introduction.....	70
4.2	Experimental.....	71
4.3	Results.....	83
4.4	Discussion.....	101
4.5	Conclusions.....	107
V.	COUPLING OF AXIAL NORMAL STRAINS WITH LONGITUDINAL SHEAR STRAINS IN HIGH PERFORMANCE POLYMER FIBERS.....	109
5.1	Background.....	109
5.1.1	Finite Strain Tensor for Simple Shear in Two Dimensions.....	109
5.1.2	Torsion of a Solid Cylindrical Rod.....	113
5.1.3	Prediction of Coupling of Axial Normal Stress with Longitudinal Shear Modulus.....	117
5.2	Experimental.....	124
5.3	Results.....	132
5.4	Discussion and Conclusions.....	146

Chapter

VI.	HELICAL COMPRESSIVE KINK BANDS IN CYLINDRICALLY ORTHOTROPIC MATERIALS: WOOD AND PPTA FIBERS.....	150
6.1	Introduction.....	150
6.2	Background.....	151
6.3	Experimental.....	155
6.4	Results.....	157
6.5	Discussion.....	166
6.6	Conclusions.....	169
VII.	FUTURE WORK.....	172
.....		
	REFERENCES.....	181
APPENDIX I.	CRITICAL BUCKLING LOAD FOR A LINK-HINGE CHAIN WITH THREE HINGES ($p=4$).....	188
APPENDIX II.	APPROXIMATE SHAPE OF LONG LINK-HINGE CHAIN.....	191
APPENDIX III.	CRITICAL BUCKLING LOADS FOR A COLLECTION OF LATERALLY INTERACTING LINK-HINGE CHAINS.....	193
APPENDIX IV.	PUBLICATIONS LIST.....	201

LIST OF TABLES

2.1	Effect of 3% Axial Compressive Strain on Tensile Properties Kevlar 49.....	27
2.2	Effect of Axial Compressive Fatigue on Tensile Strength of Kevlar 49.....	29
3.1	Comparison of Critical Buckling Loads of Link-Hinge Chains Calculated From Exact Analysis and From Approximate Formula.....	51
4.1	Tensile Properties of Fibers.....	84
4.2	Torsion Moduli and Compressive Strengths of fibers.....	88
4.3	Predicted and Measured Axial Compressive Strengths of Fibers.....	98
5.1	Linear Regression Data for Tensile Force Versus Twist Angle Measurements and Calculation of Constant a	134
5.2	Critical Shear Strains to Inelastic Torsion Deformation and Internal Kink Band Formation.....	137
5.3	Linear Regression Data for Apparent Torsion Modulus Versus Axial Tensile Stress Measurement.....	145

LIST OF FIGURES

2.1	Longitudinally distributed axial normal strains in an elastic beam loaded in three-point bending.....	13
2.2	Schematic diagram of compressed Kevlar 49 fiber bonded to a beam which had been loaded in three-point bending..	15
2.3	Longitudinally distributed axial normal strains in an elastic beam loaded in four-point bending.....	19
2.4	Optical micrographs of Kevlar 49 fiber: (a) before and (b) after 3% axial compression due to nylon matrix shrinkage.....	21
2.5	SEM micrographs of Kevlar 49 fiber: (a) as-received, (b) after 3% axial compression, and (c) after 3% axial compression. Compression due to nylon matrix shrinkage.....	22
2.6	Tensile stress-elongation behavior of a Kevlar 49 fiber that had been previously compressed 3%. (Before tensile test, fiber appeared as shown in Figure 2.5b)...	24
2.7	(a) SEM micrograph of previously kinked Kevlar 49 fiber after tensile loading to 75% of tensile strength. (b) Enlargement of region outlined in (a).....	25
2.8	SEM micrograph of tensile fracture surface of previously compressed Kevlar 49 fiber.....	28
3.1	Schematic of ideal kink band.....	37
3.2	Representation of stages of kink band formation. (Adapted equilibrium.....	40
3.3	Rigid ball analogy of the three types of mechanical equilibrium.....	43
3.4	Illustration of stability problem of a rigid bar supported at its base by an elastic hinge.....	44
3.5	Representation of the link-hinge chain model for an extended polymer chain.....	49
3.6	Postbuckled shapes of: (a) a slender column and (a) a long link-hinge chain.....	53
3.7	(a) Coordinates describing shape of buckled ling-hinge chain. (b) Expanded view of chain in vicinity of hinge i.....	56
3.8	Packing geometry for a collection of interacting and perfectly oriented link-hinge chains.....	63
3.9	Deformations with extension and shear mode buckling of a collection of link-hinge chains. (Adapted from [42]..	65
3.10	Possible shear mode buckling deformations for a collection of long link-hinge chains.....	67
4.1	Chemical structures of liquid-crystalline polymer fibers	
4.2	SEM micrograph of tensile fracture surface of P-75 graphite fiber.....	74
4.3	Schematic of torsion pendulum apparatus.....	77
4.4	Longitudinally distributed axial normal strains in an elastic beam loaded in cantilever bending.....	79
4.5	Schematic of apparatus for cantilever bending and simultaneous optical microscopic observations of a beam having fibers bonded to its surface.....	81
4.6	Tracings of optical micrographs of transverse sections of PE fibers. (a) Filament 1: tensile test sample. (b-e) Filament 2: torsion test samples.....	86

4.7	PBT fiber. Before compression: (a) optical micrograph; (b) SEM micrograph. After axial compression: (c) optical micrograph; (d) SEM micrograph.....	92
4.8	ABPBO fiber. Before compression: (a) optical micrograph; (b) SEM micrograph. After axial compression: (c) optical micrograph; (d) SEM micrograph.....	93
4.9	NTP fiber. Before compression: (a) optical micrograph; (b) SEM micrograph. After axial compression: (c) optical micrograph; (d) SEM micrograph.....	94
4.10	PE fiber. Before compression: (a) optical micrograph; (b) SEM micrograph. After axial compression: (c) optical micrograph; (d) SEM micrograph.....	95
4.11	Correlation between measured axial compressive strengths and torsion moduli for high performance organic fibers...	100
5.1	Simple shear deformation with and without volume loss.....	110
5.2	Simple shear of a material element subjected to a constant axial tensile stress.....	119
5.3	Schematic of apparatus used for torsion modulus-axial tensile stress measurements.....	130
5.4	Tensile force-twist behavior at constant length for PPTA fiber.....	133
5.5	Plot used to determine elastic torsion deformation range for ABPBO fiber.....	136
5.6	Optical micrographs of fibers held twisted at large torsion strains. (a) PPTA $\gamma=40\%$. (b) PBT, $\gamma=20\%$. (c) ABPBO, $\gamma=20\%$. (d) NTP, $\gamma=20\%$	138
5.7	SEM micrograph of NTP fiber held twisted at a surface torsion strain $\gamma=20\%$	140
5.8	(a) Optical and (b) SEM micrographs of highly twisted PE fiber. Fiber between cross polars, parallel to analyzer, in (a).....	142
5.9	Torsion modulus-axial tensile stress behavior of PBT fiber.....	144
6.1	Directions and planes of a cylindrical coordinate system...	152
6.2	(a-c) Optical micrographs of one region of a Kevlar fiber at increasing levels of axial compressive strain.....	158
6.3	(a) SEM micrograph of tensile fracture surface of Kevlar 49 fiber after subsequent compression. (b) Enlargement of area outlined in (a). Arrows point to perpendicular bands on what appear to be radial planes.....	159
6.4	Orthotropic wood block after axial compression.....	161
6.5	(a-g) Helical kink band in axially compressed wood cylinder. Each figure is a photograph taken after rotating the cylinder approximately 45° . (h) End view of cylinder shown in (a-g).....	163
6.6	Schematic of force-displacement profile and corresponding stages of helical band formation for wood cylinder compression.....	164
6.7	(a-c) Top and side views of a transverse section cut from a compressed wood cylinder that had two separate kink bands on its surface.....	165
6.8	Illustration of a compressive kink band in stacked sheets..	168
6.9	Illustration of a helical compressive kink band in a cylinder composed of radially oriented stacked sheets....	170

7.1 Simple shear deformation of a laminate. (a) Shear strain in each phase equal. (b) Shear stress in each phase equal.....	176
A1.1 Postbuckled shape of link-hinge chain with 4 links.....	189
A3.1 Coordinates for extension mode buckling deformation.....	195
A3.2 Coordinates for shear mode buckling deformation.....	199

CHAPTER I

INTRODUCTION

1.1 High Performance Organic Fibers for Composite Reinforcement

In recent years there has been conspicuously active research and development of high performance organic fibers. Organic fibers earn the title "high performance" by virtue of their excellent axial tensile properties. Such fibers are distinguished from more common textile materials by axial tensile moduli and strengths that are an order of magnitude greater than those of the synthetic textiles. Recent reviews elucidate the remarkable properties of high performance organic fibers by direct comparison to the tensile properties of structural metal and glass fibers [1,2]. The organic fibers match the tensile performance of metal and glass fibers when compared on an absolute scale and surpass the inorganic materials when compared on a weight basis.

Although several high performance organic fibers have been studied in the laboratory, only graphite and poly (p-phenylene terephthalamide) (PPTA) fibers have achieved commercial success. Because of their relatively low densities, the major application of these two types of organic fibers has been the reinforcement of structural composites, where weight savings is a prime concern. It appears that current research with other organic fibers is aimed at competing with carbon and PPTA fibers for the lightweight structural composite materials market.

The high performance organic fibers which have been produced to date can be divided into three classes: graphite fibers, synthetic rigid polymer fibers, and fibers of chain-extended flexible polymers.

Graphite fibers are currently the most widely used material for reinforcement of high performance composites because they exhibit the highest tensile moduli (200-600 GPa) of all the commercial fibers. The tensile strengths of graphite fibers are in the range of 2-3 GPa, which compare favorably to those of high performance polymer fibers. The excellent tensile properties of graphite fibers arise from a structure that consists of axially oriented graphitic microfibrils that have the strong and stiff graphite crystal basal plane oriented parallel to the long axis of the microfibrils [3,4].

The synthetic rigid polymer fibers are represented by only one commercial material: the PPTA fibers produced by E.I. DuPont de Nemours & Co. under the trade name Kevlar^R. The commercial development of synthetic rigid polymers as a whole has been hampered by production costs and problems with the synthesis of high molecular weight material. All of the rigid polymer fibers are made of polymers which exhibit liquid crystalline order in either a solution (lyotropic) or a melt (thermotropic) state. The inherent chain stiffness of both lyotropic and thermotropic liquid crystalline polymers is partially due to the high content of para-substituted aromatic groups in the chain backbone of these polymers.

Examples of lyotropic liquid crystalline polymers which have been spun into high performance fibers are: PPTA and poly (p-benzamide)

(PBA) [5,6], the aromatic polyamide-hydrazides produced by Monsanto Co. [7] and the aromatic heterocyclic polymers developed through the Air Force Materials Laboratory Ordered Polymers Program [8]. Thermotropic liquid crystalline polymer fibers that exhibit high performance properties have been developed by Eastman Kodak Co. [9], E.I. DuPont de Nemours & Co. [10], and Celanese Co. [11].

Because of the ability of some rigid-rod polymers to establish liquid crystalline order, uniaxial orientation of either ordered solutions or ordered melts is easily induced during fiber spinning and maintained during subsequent solidification. Therefore, the excellent tensile properties of rigid-rod polymer fibers result from almost perfect orientation of stiff polymer chains along the fiber axis.

The "class" of high performance organic fibers of chain-extended flexible polymers is essentially comprised of one material: highly oriented polyethylene (PE). This commodity polymer has been transformed into a high performance material by processes that involve stretching the coiled polymer chains along one direction to an almost fully extended conformation. The estimates of the theoretical axial modulus of a fully-extended PE chain are high [12] and PE fibers and films exhibiting values of tensile modulus that are close to theoretical estimates have been produced by efficient drawing methods. The two types of drawing processes that have received the most attention are gel-spinning [13] and solid state deformation [14,15]. PE fibers produced by gel-spinning techniques have tensile moduli and strengths exceeding 100 GPa and 2.5 GPa, respectively. Fibers produced by the gel-spinning process

are about to achieve commercial status [16]. The substantial tensile properties of high performance PE fibers can be attributed to the alignment of highly extended polymer chains along the fiber axis.

The production of all high performance organic fibers requires that the direction of strongest molecular bonding, whether it be within graphitic planes or along extended polymer chain axes, be aligned parallel to the fiber axis. A consequence of having strong bonds oriented along the fiber axis is that only weaker molecular bonds, i.e., secondary bonding forces between graphite planes or between extended polymer chains, are aligned laterally. Therefore, all of the high performance organic fibers are highly anisotropic materials.

Experience with graphite fiber-reinforced composites shows that they suffer from low impact strength, susceptibility to catastrophic failure and poor damping characteristics [17]. Improvements in all of these properties have been realized with composites reinforced by PPTA fibers [17]. Indeed, composites reinforced by both graphite and PPTA fibers (hybrid composites) have been fabricated in order to ameliorate the problems associated with the brittle nature of graphite fiber composites [17,18].

Polymer fibers have lower tensile moduli than graphite fibers and many applications of structural composites are oftentimes stiffness-critical, demanding the highest modulus materials. However, recent developments with poly (p-phenylene benzobisthiazole) (PBT) fibers have demonstrated that it is possible to attain tensile moduli exceeding 300 GPa with a polymer fiber [19].

A critical problem with polymer fibers, which limits their use in composites, is their relatively poor axial compressive strength. Kevlar fiber-reinforced composites exhibit longitudinal compressive strengths that are only 20% of their longitudinal tensile strengths [17]. A recent study with PBT fibers indicates that these polymer fibers also suffer from a weakness in axial compression [19]. There are few studies of the compressive characteristics of high performance polymer fibers in the open literature. Consequently, there is no clear explanation of the mechanism(s) of compressive failure, and the problem of limited axial compressive strengths of polymer fibers remains, at present, unsolved.

In this dissertation, the axial compressive behavior of several high performance fibers is investigated with the intent of elucidating the failure mechanism(s) that lead to compressive strengths which fall short of "high performance."

1.2 Dissertation Overview

The goals of this study are: to investigate the mode(s) of failure of high performance polymer fibers under axial compression; to propose a mechanism(s) for failure under axial compression and attempt to predict the compressive strengths of polymer fibers; and to suggest ways to improve the compressive characteristics of high performance polymer fibers.

In Chapter II, the axial compressive behavior of PPTA fibers is investigated. Techniques for compressing single fibers are introduced

and the mode of failure is examined by microscopy. Combining the results obtained here with those reported by other workers provides the necessary evidence to propose a microbuckling instability mechanism for compressive failure of PPTA fibers.

Chapter III begins with a review of compressive failure mechanisms previously proposed for a wide range of materials. By analogy to compressive strength theories for fiber-reinforced composites, an analysis of the elastic microbuckling of polymer chains and/or microfibrils is presented. A potential energy balance analysis is used to calculate critical stresses for the onset of compressive buckling instabilities in an idealized model of a polymer fiber. These critical stresses are used as theoretical estimates of the axial compressive strengths of extended-chain polymer fibers.

The predicted compressive strengths obtained from the microbuckling analysis are compared to measured fiber compressive strengths in Chapter IV. Three lyotropic and one thermotropic liquid crystalline polymer fibers, a gel-spun PE fiber and a graphite fiber are examined.

Chapter V is a discussion of the coupling between axial and shear stresses and strains in anisotropic polymer fibers. This coupling is experimentally verified by the observations of fiber axial compressive failure due to fiber torsion and the linear dependence of fiber torsional rigidity on axial tensile stresses. Consideration of the effects of axial compressive stresses on the fiber torsional rigidity leads to the conclusion that an instability occurs at the same compressive stress

that is predicted by the microbuckling analysis presented in Chapter III.

In Chapter VI, the formation of helical compressive kink bands in Kevlar 49 fibers is compared with similar band formation in compressed wood. The formation of these helical bands is shown to be a consequence of the particular cylindrically orthotropic symmetry common to these materials.

CHAPTER II

COMPRESSIVE BEHAVIOR OF POLY (P-PHENYLENE TEREPHTHALAMIDE) FIBERS

2.1 Background

The well-known Achilles' heel of PPTA fiber-reinforced composites is their relatively low longitudinal compressive strength [17]. The ratio of longitudinal tensile to compressive strength of these composites is approximately 5:1. Compressive stress-strain curves for unidirectional PPTA fiber composites exhibit elastic-plastic behavior with yield at approximately 0.3% compressive strain [17].

Attempts to improve the compressive strength of a composite reinforced by one particular PPTA fiber, Kevlar^R 49, via fiber pretensioning and pretwisting or modification of the fiber-matrix interface and matrix properties were unsuccessful [20]. Microscopic examination of compressed PPTA fiber-reinforced composites revealed the formation of kink bands within the fibers [20,21]. It has therefore been proposed that the compressive strengths of PPTA fiber composites are limited by the fiber compressive strength [20-22].

The structure of PPTA fibers, especially the Kevlar fibers, has been the subject of numerous papers [23-35]. Studies have shown that there is excellent orientation of rigid PPTA chains along the fiber axis [23,24]. Consequently, fiber tensile moduli that approach theoretical estimates have been measured [23,25,26].

X-ray diffraction studies reveal that PPTA fibers are highly crystalline and exhibit diffraction characteristics that are indicative of a paracrystalline structure [23,27]. A monoclinic unit cell with the chain axis parallel to the c-axis and the plane of hydrogen bonding between chains nearly parallel to the b-axis has been established for PPTA fibers [23,25].

The b-axis of the unit cell, and therefore the hydrogen-bonded planes or sheets, is oriented along the radial direction of the fiber. This organization of the PPTA crystal into a radial sheet structure gives PPTA fibers a cylindrically orthotropic symmetry [28-30].

The morphology of PPTA fibers at the supramolecular scale has not been firmly established. The fibers exhibit a periodic transverse banding with a periodicity of roughly 250 nm [27,28,31,32] that has been attributed to regular pleats in the radially oriented hydrogen-bonded sheets [28]. Others have proposed that periodic transfer defect planes, spaced 200 nm [33,34] or 50 nm [27] apart, are superimposed upon the pleated sheets. It is believed that these defect planes are formed by the aggregation of chain ends [27,34].

Both X-ray and electron diffraction studies indicate that there are axially oriented crystallites in PPTA fibers which are approximately 7 nm wide [23,31]. Fiber etching and degradation studies show that there may be another structural unit, called a rod-like crystallite, that is also axially oriented, but nearly 60 nm wide [33,34]. Also, it has been suggested that PPTA fibers have a fibrillar structure, with fibrils roughly 600 nm in diameter [27].

PPTA fibers are inhomogeneous materials due to the existence of a skin that has been estimated to be 0.1-1.0 μm thick [27,33,34]. Most evidence shows that the skin does not exhibit periodic transverse banding and is less susceptible to degradation than the fiber core [27,33]. These results suggest that the skin exhibits higher PPTA chain orientation and a more perfect structure than the core.

The existence of voids in PPTA fibers has been revealed by staining techniques and scattering measurements [27,35]. The voids appear to be needle-shaped, with the long axis oriented parallel to the fiber axis [35]. The total void content in PPTA fibers must be less than 5%, since the densities of these fibers are typically 95% of the density of the PPTA crystal unit cell [23,25].

The first attempt to characterize the compressive properties of PPTA fibers was reported by Greenwood and Rose [22]. By measuring the geometry of the elastica using Kevlar 49 fibers, they were able to determine that the fibers apparently yielded at bending strains of about 0.7%. This apparent plasticity corresponded to the formation of kink bands at oblique angles to the fiber axis on the compressive side of the bent fiber. Because most polymer matrices have elastic limits in compression greater than 0.7%, it was concluded that the low compressive strength of Kevlar composites can be attributed to the poor compressive strength of the fibers and not to either the matrix or the fiber-matrix interface.

The formation of the kink bands in Kevlar fibers due to compressive strains in bending has been well documented [21,22,36]. Similar

band formation has also been seen in fibers extracted from axially compressed unidirectional composites [20,21,37].

The morphology of compressive kink bands in Kevlar fibers has been investigated using scanning and transmission electron microscopy by Dobb and co-workers [21]. Fibers were compressed by bending techniques and by the longitudinal compression of a Kevlar composite to strains well above the apparent yield point. Some of their results and conclusions that are pertinent to this dissertation are:

- (1) Deviation from elastic behavior with accompanying kink band formation occurred at approximately 0.5% bending strain in the elastica test.
- (2) Kink bands were observed to unfold under tension, indicating that the kink band boundary acts like a hinge.
- (3) Flexural fatiguing of single fibers at an apparent bending strain of 2% resulted in a loss in tensile strength of $\leq 20\%$.
- (4) The tensile fracture morphology of previously compressed fibers was a surface plane oriented at 45° to the fiber axis.
- (5) The formation of compressive kink bands was apparently unrelated to the pleated-sheet structure exhibited by Kevlar fibers.

Takahashi et al. examined sections of compressively kinked Kevlar 29 fibers by X-ray and electron diffraction and electron microscopy [37]. They found preferential formation of kink bands oriented at 55° to the fiber axis on tangential planes, and deformation bands nearly perpendicular to the fiber axis on radial planes. These authors

concluded that the pleat angle of the radial hydrogen-bonded sheets decreases under axial compression.

In this dissertation, techniques for applying uniform axial compressive strains to small diameter fibers are introduced. These techniques require that the fiber be surrounded by a matrix that supports it against buckling and that transmits uniform axial compressive loads to the fiber. The axial compression of fibers embedded in matrices has been used previously to study the compressive fracture and buckling modes of fine fibers [38-41]. In these studies fiber compression was induced by: matrix contraction during casting from solution [38], differential thermal shrinkage [39,40], compression of a fiber-containing matrix block parallel to the fiber axis [41], and shrinkage of a matrix polymerized around the fibers [38].

2.2 Experimental

In this work a new method for applying known and uniform compressive strains to fine filaments is introduced. The technique involves bonding fibers to one surface of an elastic rectangular beam after orienting them parallel to the beam length. On subjecting the beam with bonded fibers to three-point bending, tensile and compressive strain distributions that vary linearly along the length of the beam as shown in Figure 2.1 are induced. Assuming there is good bonding of the fibers to the beam, the strain in a fiber at any point along its length should be equal to the surface strain of the beam at the same location. For small deflections, the equation for the longitudinal surface strain

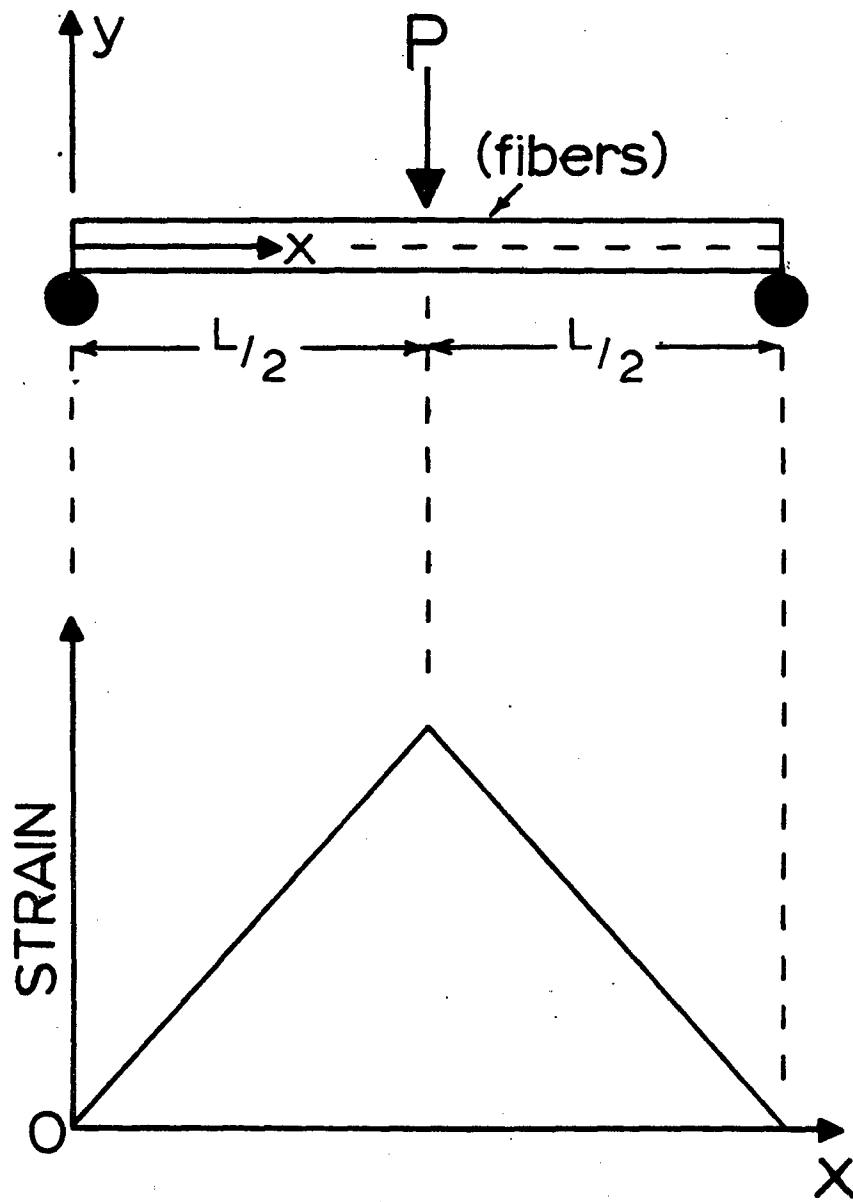


Figure 2.1. Longitudinally distributed axial normal strains in an elastic beam loaded in three-point bending.

distribution ϵ in a beam bent into a three-point configuration is:

$$\epsilon = (1 - \frac{d}{L/2})\epsilon_m \quad (2.1)$$

d = distance along beam length measured from midpoint

L = span length of beam

ϵ_m = maximum strain on beam surface (occurs at midpoint)

The axial compressive strain that initiates kink band formation is determined by locating the region along the bonded fiber length where kink bands first occur. A schematic diagram of a compressed Kevlar 49 fiber bonded to a beam that had been previously loaded in three-point bending is shown in Figure 2.2. Because maximum compressive strains occur at the beam midpoint (i.e., the point of load application) in three-point bending, the length of fiber in this section of the bar exhibits kink banding. The kink bands are fainter and occur less frequently at distances along the fiber away from the midpoint. The distance d along the fiber from the beam midpoint to the region where the last fiber kink band is observed is recorded. The axial compressive strain that initiates kink banding is calculated using (2.1). This compressive strain is defined as the critical compressive strain ϵ_c .

It is recognized that the strain in the bent beam also varies through the beam thickness from zero at the neutral axis to a maximum on the outer surfaces. However, the relative thickness of beam to fiber is so large (250:1) that the variation in strain across the fiber diameter can be neglected.

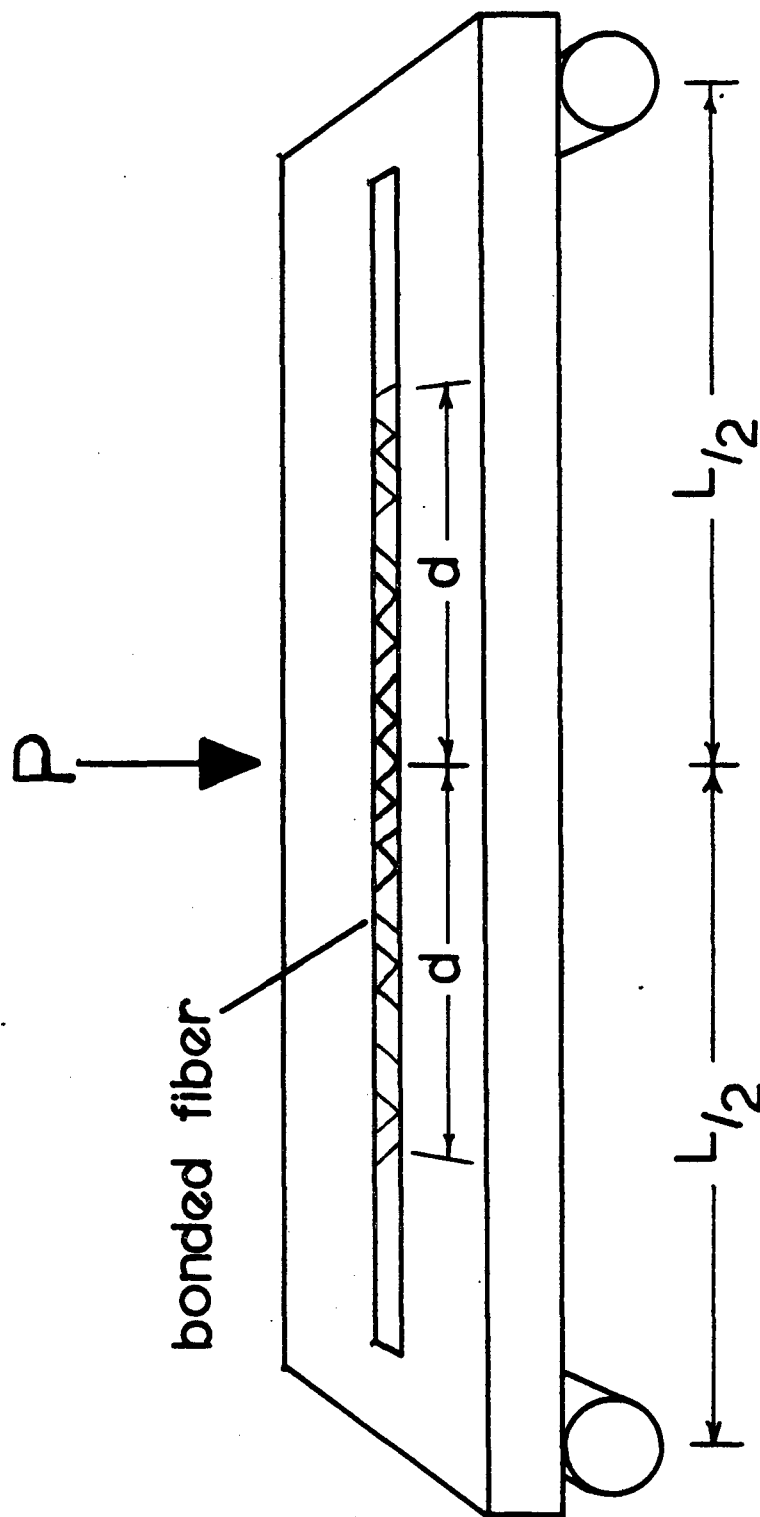


Figure 2.2. Schematic diagram of compressed Kevlar 49 fiber bonded to a beam which had been loaded in three-point bending.

Filaments of Kevlar 49 (diameter = 12.2 μm) were separated from a 380 denier yarn. The fibers had no sizing or finish and were used in all tests without any special pretreatment.

To prepare test specimens, single Kevlar fibers were first aligned with ends taped to one side of a clear polycarbonate tensile bar which had been milled down to a uniform cross-section of 1/8 in. x 1/2 in. By hanging a 0.5 g weight from one end of the fiber, the fiber could be affixed to the bar under a calculated tensile pre-strain of 0.03%. The fibers were then bonded to the polycarbonate bar by applying several layers of a clear acrylic spray (Krylon^R Acrylic Spray Coating, Borden, Inc.). After allowing 24 hours for the coating to dry, the bars with bonded fibers were loaded in three-point bending in an Instron to a maximum strain on the beam surface (ϵ_m) of 1.0% at the load point. After loading, the bars were removed from the Instron and the bonded fibers were examined for kink formation. The advantage of bonding fibers to a transparent polycarbonate bar with a clear acrylic spray is that they can be observed in situ with an optical microscope directly after loading. Also, the shrinkage of the thin acrylic film during drying (solvent evaporation) is prevented by the relatively thick bar to which it is bonded.

A matrix shrinkage technique was used to obtain fibers in a compressed state for optical microscopy and scanning electron microscopy (SEM) studies and tensile tests. Single Kevlar 49 fibers were embedded in a matrix of nylon-6 ($M_n=18,000$) by solvent-casting a film of the nylon around fibers mounted with minimal tension on a glass plate. A

solution of 10% (w/w) nylon-6 in 88% formic acid gave good quality films approximately 50 μm thick when cast over a hot plate heated to about 80°C. With solvent evaporation the nylon film shrank, subjecting the Kevlar fiber to hydrostatic compression.

Observations of cast films containing fibers using an optical microscope revealed that kink bands only formed in the embedded Kevlar fiber after the film was separated from the glass plate on which it was cast. These observations implied that due to an adhesion of the nylon film to the glass plate, most of the film axial shrinkage occurred only after it was carefully peeled off the plate. Using ink markers on the nylon film, it was determined that the nylon matrix shrinkage along the embedded fiber axis was approximately 3%.

Compressed fibers were removed from the surrounding nylon matrix by dissolving the matrix with formic acid. Compressed and isolated fibers were carefully mounted onto cardboard tabs with epoxy and tensile-tested at an initial gauge length of 50 mm and a crosshead rate of 0.1 cm/min. Each fiber sample was loaded twice: first, to approximately 75% of the anticipated breaking strength and then, after immediate unloading, to fracture. Samples of compressed fibers before and after tensile testing were examined using scanning electron microscopy (SEM).

The effect of axial compressive fatigue on the tensile strength of Kevlar fibers was investigated using a variation of the elastic beam compression technique. Bonding fibers to the compressive side of a beam which is then loaded in four-point bending causes the length of fiber between the two loading points to be subjected to a constant axial

compressive strain. This constant strain region in four-point beam bending is shown schematically in Figure 2.3.

Single filaments of Kevlar 49 were bonded under a known tensile pre-strain to milled tensile bars as already outlined. However, for these tests glass-filled polyphenylene oxide/polystyrene blend tensile bars were used in place of polycarbonate bars in an attempt to avoid stress cracking of the bar during fatigue bending. Fibers were loaded in compression between a minimum strain of 0.1% and maximum strain of 0.4%, 0.8% or 1.2% for 1, 10, and 100 cycles. After loading, the fibers were recovered for SEM observations and tensile testing by soaking the bars in acetone to dissolve the acrylic film.

Fiber samples were examined using an ETEC Autoscan SEM after coating with a $\sim 200\text{\AA}$ layer of gold in a Polaron E5100 SEM sputter-coating unit. For tensile tests, all fibers were mounted onto cardboard tabs with epoxy and tested in an Instron Universal Testing Machine. A small Zeiss optical microscope with polarizers was used to observe fibers embedded in nylon-6 films.

2.3 Results

A critical compressive strain of 0.53% ($\pm 0.02\%$) was determined from beam bending measurements on ten Kevlar 49 fiber samples. This value of ϵ_c has been corrected for the tensile pre-strain applied to fibers during mounting onto polycarbonate bars. Some of the bars were loaded more than once to the 1% maximum strain (ϵ_m). After repeated loadings to this same level of strain, no change was observed in d and

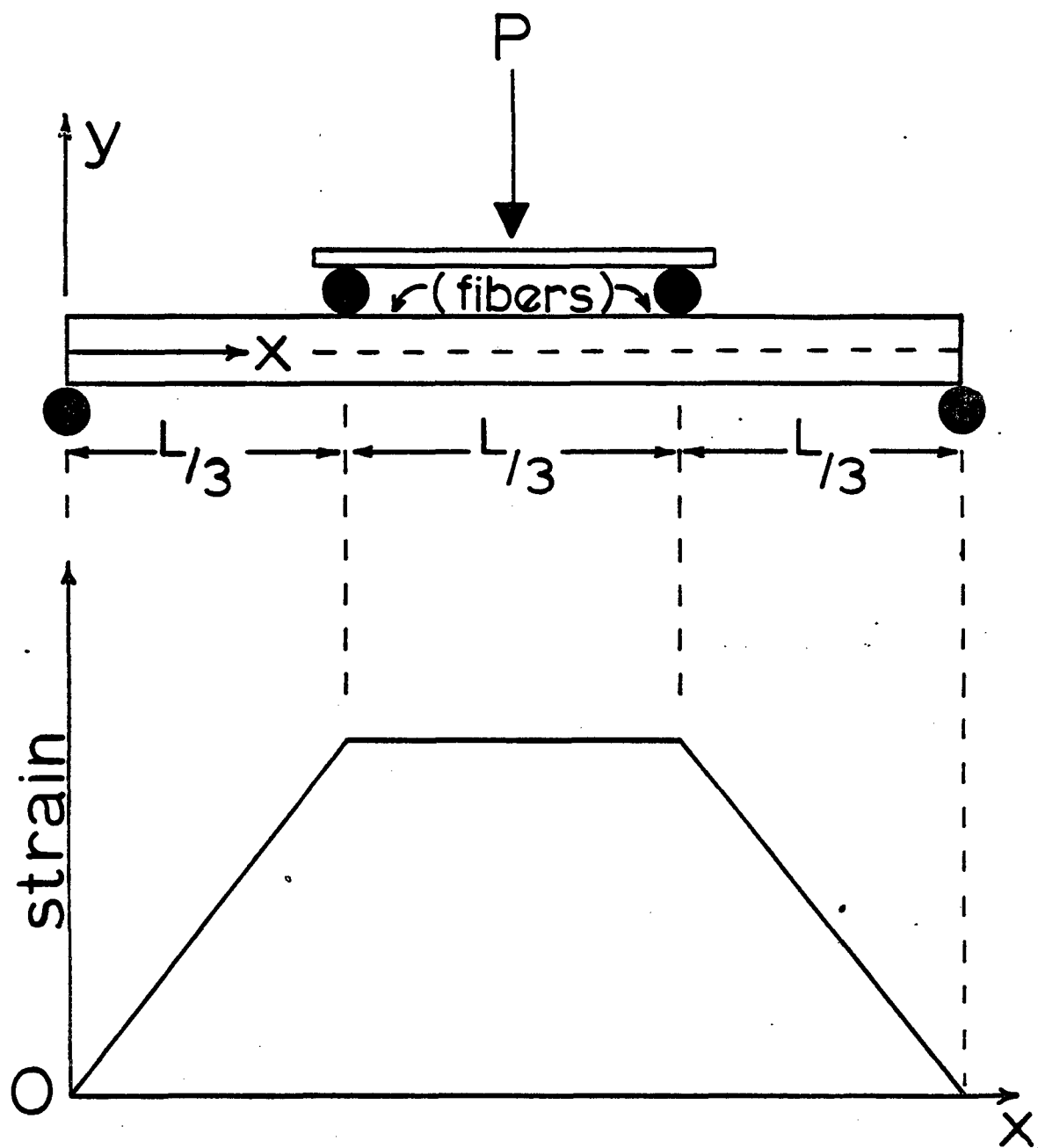


Figure 2.3. Longitudinally distributed axial normal strains in an elastic beam loaded in four-point bending.

therefore in ϵ_c . However, in the length of fiber which exhibited kink banding, the kink bands appeared to increase in both number and severity with repeated loadings.

The compressive kink bands appear as black V-shaped bands when viewed with an optical microscope. An optical micrograph of these kink bands is shown in Figure 2.4. It should be emphasized that the bonded fibers were examined after compression in the unloaded state. Because kink bands were seen in the fiber after unloading the bar, this indicates that slip occurred at the fiber-matrix interface and/or that permanent deformation occurred in the fiber at the kink boundary.

An axial compressive strength of 0.7 GPa is calculated for Kevlar 49 from the product of ϵ_c and the axial compressive modulus. For this calculation it is assumed that the fiber is linear-elastic to ϵ_c and that the axial tensile and compressive moduli are identical and equal to 130 GPa. That the moduli are equivalent is demonstrated indirectly by the measured equivalent tensile and compressive moduli of Kevlar composites [17] and by the elastica test in which Kevlar fiber conforms to the loop geometry predicted for linear-elastic materials [22].

The surfaces of Kevlar 49 fibers as-received and after compression due to shrinkage of a surrounding solvent-cast nylon matrix are shown in Figure 2.5. After approximately 3% axial compressive strain the fibers exhibited surface helical kink bands having a pitch angle of 60° . Both left- and right-handed helices were observed, which propagated for various distances along the fiber axis. These helical bands corresponded to the V-shaped bands observed for a compressed fiber using optical

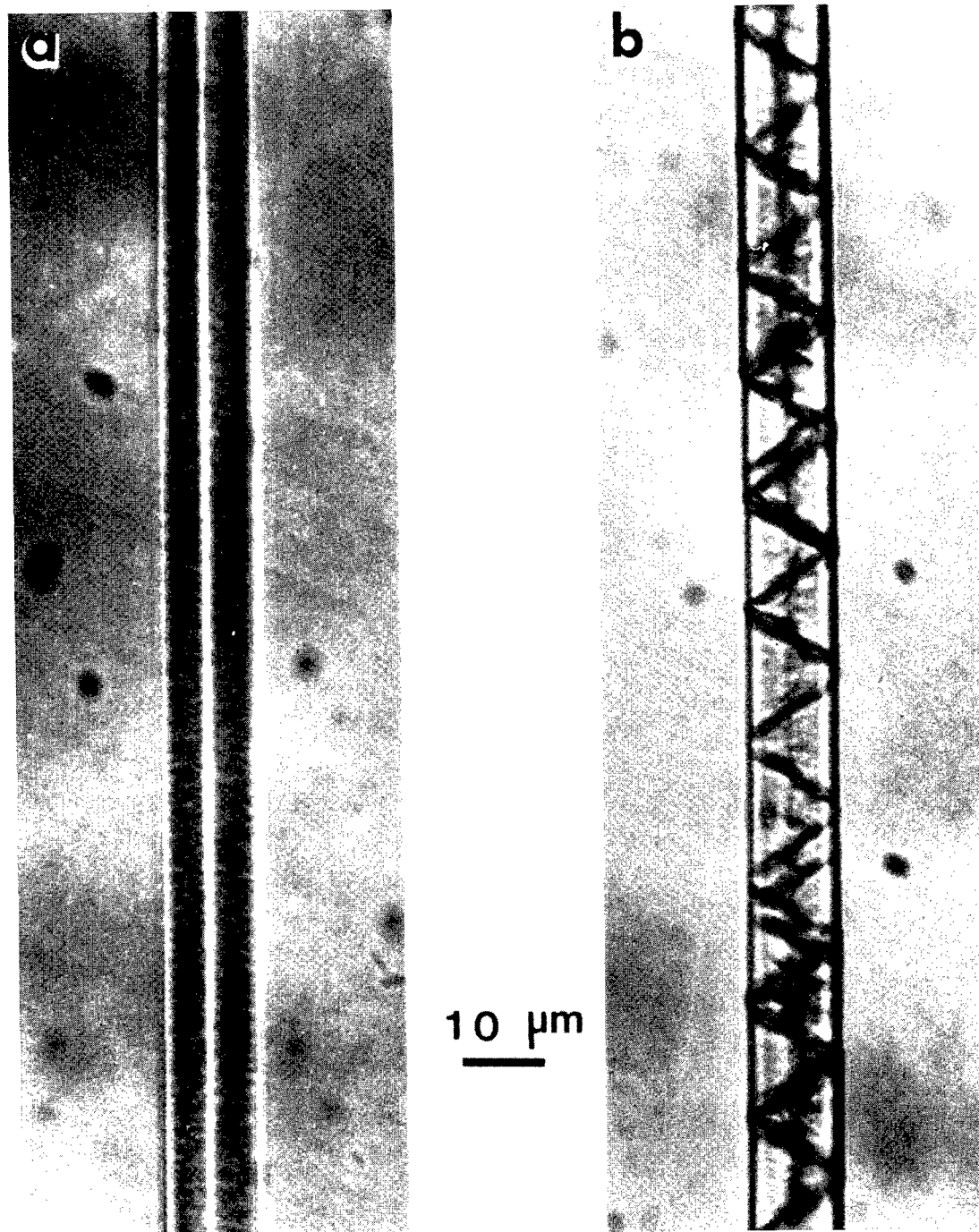
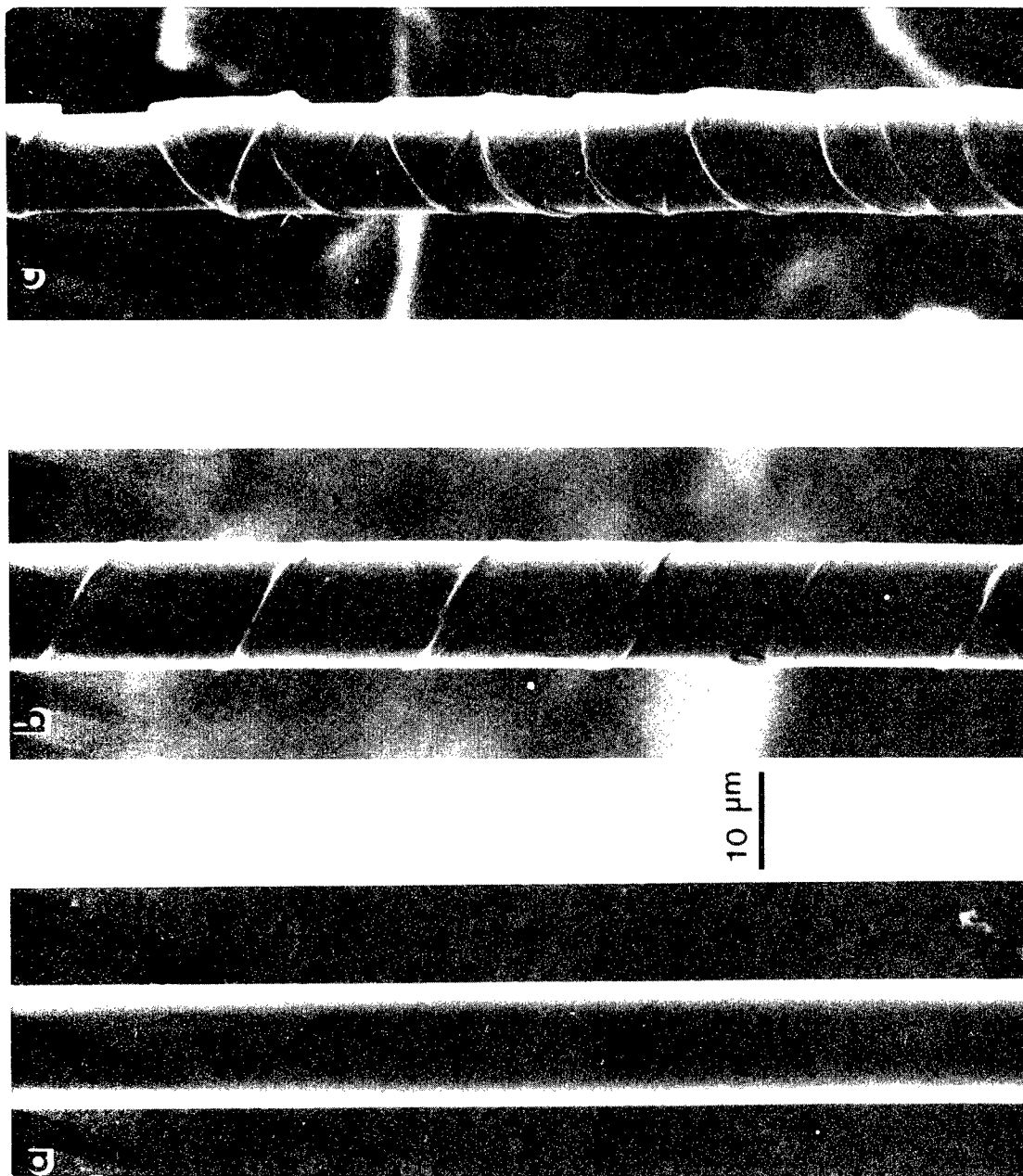


Figure 2.4

Optical micrographs of Kevlar 49 fiber: (a) before and (b) after 3% axial compression due to nylon matrix shrinkage.



SEM micrographs of Kevlar 49 fiber (a) as-received, (b) after 3% axial compression, and (c) after >3% axial compression. Compression due to nylon matrix shrinkage.

Figure 2.5

microscopy. At slightly higher compressive strains the bands became sharper and more numerous, as shown in Figure 2.5c. At this level of compression there were lateral shifts of fiber segments, similar to slip bands observed in metals. It also appears that fiber material piled up at the kink boundaries with no evident change in the surface texture between the bands. None of the compressed fibers gave any indication of surface cracking or splitting within the limits of SEM resolution. Interestingly, the single Kevlar fibers could sustain axial compressive strains of up to 3% without exhibiting the sinusoidal microbuckling instabilities normally associated with fiber-reinforced composite compressive failure [42].

Fibers recovered from the solvent-cast nylon matrix were in a permanently compressed state because kink bands were observed after removal of the matrix-induced compressive load. The tensile behavior of such compressed fibers is illustrated in Figure 2.6. The dramatic change in the shape of the stress-strain curve from that of the as-received Kevlar 49 fiber was seen with initial tensile loading. The fiber extended at a nearly constant and low stress to approximately 2% elongation. With further extension there was a large upturn in the curve as the apparent fiber modulus increased. After removing the tensile load, the fibers were found to have attained a new gauge length $2.0 \pm 0.5\%$ greater than the initial 50 mm length. SEM micrographs of previously kinked fibers after the first tensile loading are shown in Figure 2.7. These pictures reveal that the kinks have unfolded, appearing only as stretch marks or depressions on the fiber surface.

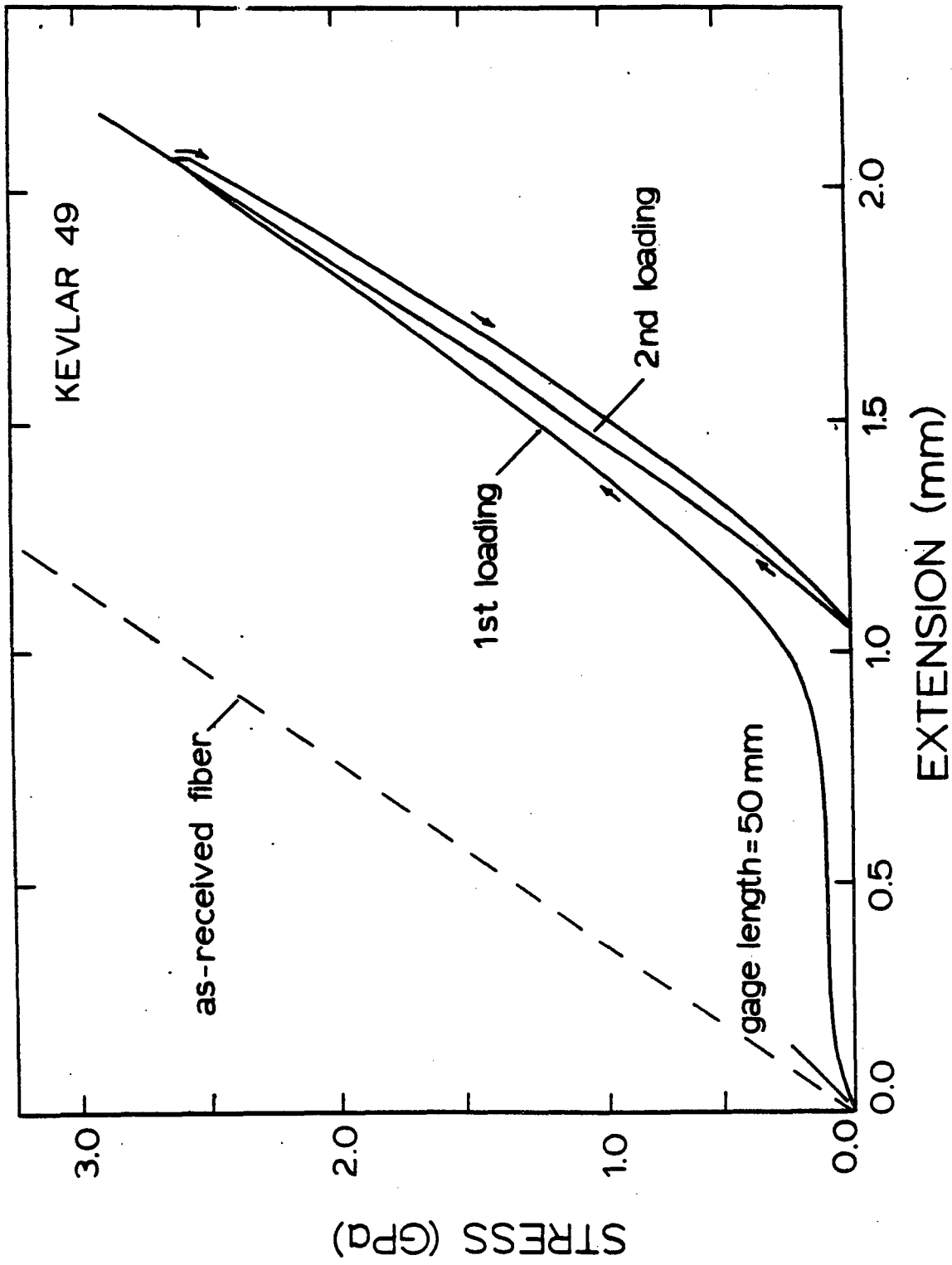


Figure 2.6

Tensile stress-elongation behavior of a Kevlar 49 fiber that had been previously compressed 3%. (Before tensile test, fiber appeared as shown in Figure 2.5b).

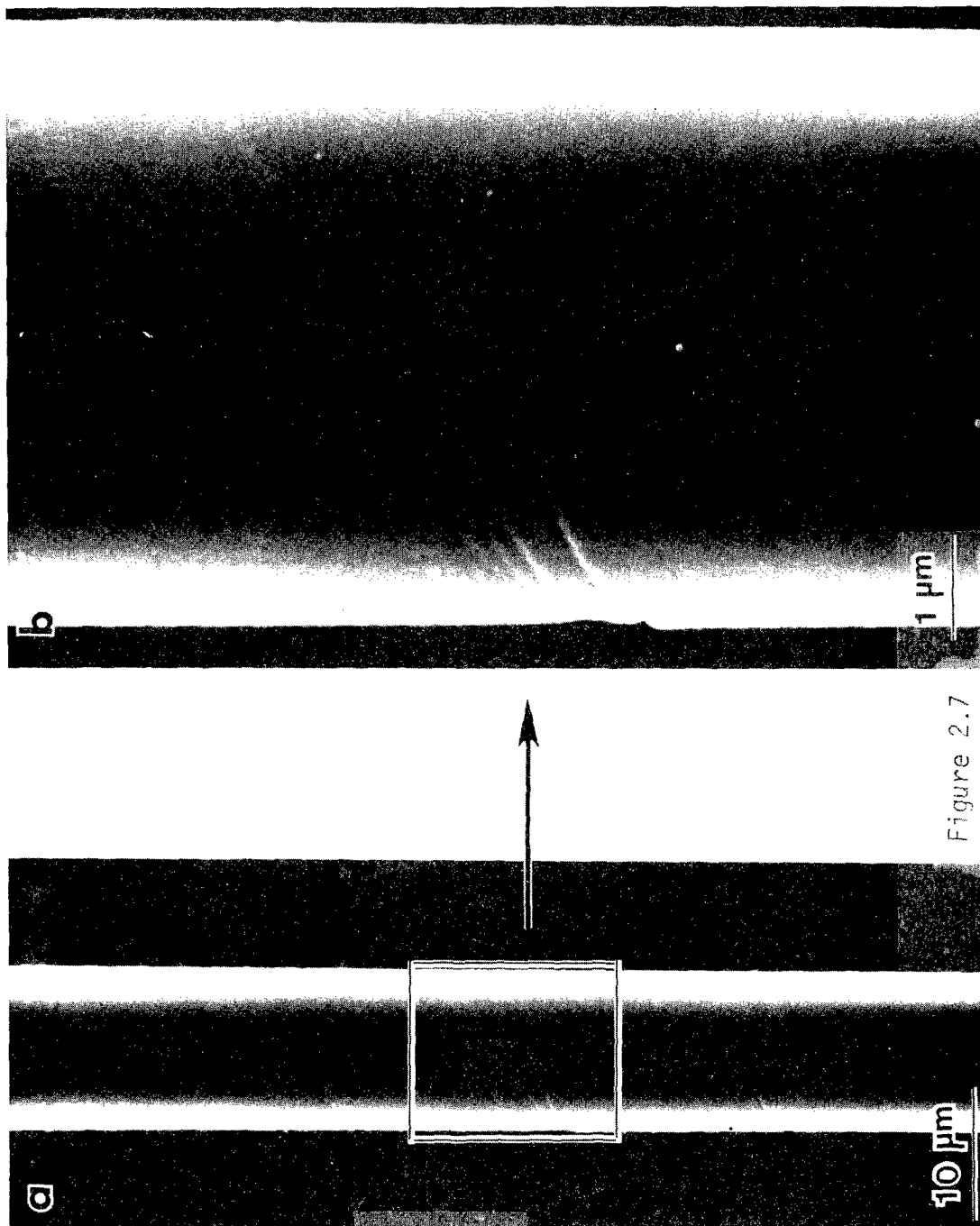


Figure 2.7

(a) SEM micrograph of previously kinked Kevlar 49 fiber after tensile loading to $\sim 75\%$ of tensile strength. (b) Enlargement of region outlined in (a).

The tensile stress-strain curve measured upon reloading the fibers to break is almost indistinguishable from the curve obtained for as-received fiber (Figure 2.6). The tensile properties of previously compressed and as-received Kevlar 49 fibers are summarized in Table 2.1. Surprisingly, the only permanent effect of prior compressive kinking on the tensile properties is a small loss in tensile strength.

The tensile fracture surface of a previously compressed fiber loaded in tension to failure is shown in Figure 2.8. The longitudinal splitting is identical to that observed for as-received fibers also fractured in tension [33,43]. Examination of the fibers at high magnifications gave no indication that tensile failure initiated from a kinked region.

Further proof that the recoverable tensile properties of Kevlar fibers are relatively insensitive to axial compression is the small measured loss in tensile strength of fibers subjected to compressive fatigue using the four-point beam bending technique. The tensile strengths of these fibers listed in Table 2.2 show that even after 100 cycles to 1.2% compressive strain there is only a 10% loss in strength. Faint helical kink bands were observed only on isolated fibers which had been compressed to maximum strains of 0.8% and 1.2%.

2.4 Discussion

A 0.5% critical axial compressive strain measured for Kevlar 49 using the beam bending technique is comparable to strain values calculated at the apparent yield point in the fiber elastica tests. However,

Table 2.1

Effect of 3% Axial Compressive Strain on
Tensile Properties of Kevlar 49

Fiber History	Tensile Modulus (GPa)	Elongation at Break (%)	Tensile Strength (GPa)
As-received	125	2.5	3.2
Compressed* 3%	125	2.5	2.7

*Taken from second loading curve (see Figure 2.6). Values represent an average of eight tests.

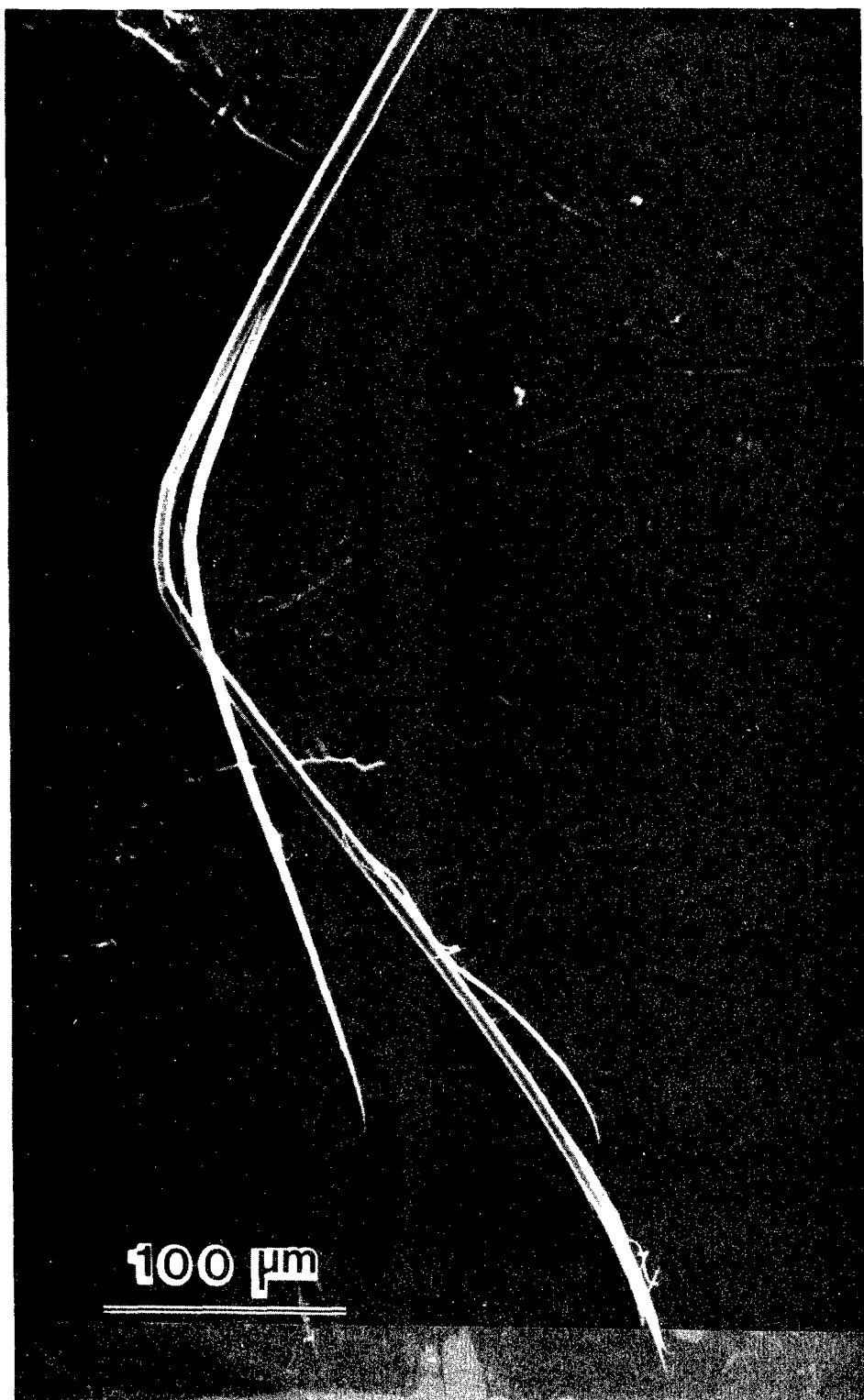


Figure 2.8

SEM micrograph of tensile fracture surface of previously compressed Kevlar 49 fiber.

Table 2.2

Effect of Axial Compressive Fatigue on
Tensile Strength of Kevlar 49

Maximum Compressive Strain (%)	<u>Tensile Strength</u>		
	Number of Compression Cycles		
	1	10	100
0.4	3.3	3.1	3.2
0.8	3.0	3.1	3.0
1.2	3.3	3.3	2.9

As-received Kevlar 49: 3.3 GPa

this value for ϵ_c was determined in the beam bending tests from the appearance of permanent and therefore visible kink bands in unloaded fibers. Therefore the value of ϵ_c reported here represents an upper limit for the strain to kink formation. This could partially account for the discrepancy between ϵ_c and the reported 0.3% compressive yield point for unidirectional Kevlar 49 composites.

No sinusoidal microbuckling instabilities were observed for the nylon matrix-compressed single Kevlar filaments with up to 3% axial strain. This observation implies that the microbuckling theories of unidirectional composites which can satisfactorily predict the compressive strengths of composites based on isotropic fibers may have no bearing on the compressive strength of Kevlar composites. Moreover, this would explain the differences found by Rosen and co-workers between measured Kevlar composite compressive strengths and the predicted strengths calculated using a fiber microbuckling theory which was modified to account for fibers having a low shear modulus [20]. Therefore, the proposal that the low compressive strength of PPTA fiber composites is due to the limited axial compressive strength of the fibers [20-22] is supported by the results obtained here for uniform axial compression of the PPTA fibers.

Although the compressive strength of Kevlar 49 appears poor in comparison with the strengths of glass and graphite fibers, it is significantly better than the compressive yield strengths of most polymers. For instance, commercial nylons exhibit yield strengths in compression

of approximately 0.1 GPa compared to 0.7 GPa measured here for Kevlar 49.

A small and nearly constant tensile load is required to unfold the kink bands of compressed Kevlar 49 fibers. The draw region at this load persists until the point of extension where all the compression set is eliminated; i.e., until the kinks unfold completely. Once the kinks unfold and the fiber segments realign, the initial as-received fiber modulus can be regained. The large difference in stiffness between kinked and straightened fibers indicates that the compressive buckling and kinking occurs throughout the fiber cross-section rather than on the fiber surface alone. Since there is little evidence of fiber splitting and loss of tensile properties after the application of as much as 3% compressive strain or after compressive fatiguing, it seems unlikely that much chain scission occurs during kink band formation. It is conceivable that the formation of kink bands occurs by bond bending and rotation, and by chain slippage. Such kink formation may be viewed as the buckling of microfibrils or of the PPTA chains themselves. Also, because the kink bands tend to take on a helical shape at the fiber surface, there may be a propagation of the band from some nucleation or defect point.

Although the kink bands seem to form almost reversibly, SEM observations show that there is always some permanent surface damage which remains after unfolding the kink bands. These residual bands probably act as defect regions that greatly reduce the fiber compressive strength and compressive modulus in subsequent loadings.

Among the results obtained in this study, a few appear to conflict with the results obtained by Dobb et al. [21]. The degree of structural damage due to kink band formation in Kevlar 49 is much less than seen by these other workers. In their study, flexural fatigue of Kevlar 49 fibers was performed at maximum bending strains that were identical to the ultimate tensile strain of the fiber. Therefore, the significant loss in tensile strength of Kevlar 49 fibers measured by Dobb et al. after flexural fatiguing could be attributed to tensile failure during bending. Furthermore, the tensile fracture of previously compressed Kevlar along a plane oriented at 45° to the fiber axis observed by these workers was never seen in this study for fibers broken in tension after a 3% compressive strain was applied. It would appear that the Kevlar 49 fibers studied by Dobb et al. had been compressed severely enough to cause massive structural damage within the fiber kink band. Consequently, it is not surprising that these workers could not find any relationship between the pleated sheet structure of Kevlar fibers and the formation of kink bands in severely compressed fibers.

The observation of helical bands on the surface of axially compressed Kevlar fibers and the correspondence of these bands to V-shaped bands observed by optical microscopy in the present study suggests that the extent of detectable damage within the core of compressively kinked fibers is minimal. It is reasonable to conclude that the core of the fiber probably accommodates axial compressive deformation via an increase in the pleat angle of the radially oriented sheets as suggested by Takahashi et al. [37].

2.5 Conclusions

A new technique that allows the application of small and known axial compressive strains to fine fibers was used to determine that kink bands initiate in Kevlar 49 fibers at approximately 0.5% strain. This critical fiber compressive strain and corresponding calculated compressive strength of 0.7 GPa are similar to the compressive strains and stresses in Kevlar 49 fibers at the compressive and flexural yield points of their composites [17]. Possibly better agreement between composite data and beam bending measurements of critical compressive strains could be obtained by examining the bonded fibers in the loaded or compressed state; i.e., by maintaining the bent configuration of the beam during microscopic observations of the bonded fiber.

Although the compressive strength of Kevlar 49 fiber appears low relative to other high performance fibers, it is several times larger than the compressive strengths of most polymers.

The effect of axial compression on the recoverable tensile properties of Kevlar 49 fiber was surprisingly small. The axial compressive failure of the highly anisotropic Kevlar 49 fiber is perceived to be due to microbuckling of microfibrils or extended PPTA chains with the resultant formation of visible kink bands.

C H A P T E R I I I
AN ELASTIC MICROBUCKLING THEORY TO PREDICT THE AXIAL
COMPRESSIVE STRENGTHS OF EXTENDED-CHAIN POLYMERS

3.1 Background

The mechanisms of material failure under uniaxial compression are not as easily perceived as are mechanisms for shear and tensile failure. The sliding of parallel planes of atoms past one another or the separation of two parallel planes of atoms are conceptually satisfying mechanisms for shear and tensile failure, respectively. Indeed, theoretical predictions of material shear [44] and tensile [45] strengths have been calculated based on such mechanisms of failure. Material failure under uniaxial compression has been observed to occur by several modes, most of which involve shear deformations.

The most common mode of uniaxial compressive failure for isotropic materials is plastic deformation (slip) or fracture along material planes oriented at 45° to the load direction. Stress analysis for axial compressive loading shows that shear stresses within the material are maximum along these obliquely oriented planes. Therefore, failure under compression along lines oriented at 45° to the axis of loading is interpreted as simple shear failure. This maximum shear stress criterion for failure requires only that the magnitude of the applied stress reach some critical value for failure to occur. Therefore, a material which fails by this mechanism should do so at the same level of compressive and tensile stress.

The mechanism of compressive failure of anisotropic materials depends on both the material symmetry and the direction of compressive load application with respect to this symmetry. In some anisotropic materials there are directions within particular material planes along which shear deformation occurs most easily. In single crystals these directions and planes of easy shear deformation are called slip systems. If the critical shear stress required to fail or plastically deform the material within a slip system is known, then the compressive stress which "activates" the slip system can be calculated from:

$$\sigma = \frac{\tau_c}{\cos\theta \cos\psi} \quad (3.1)$$

where τ_c = critical (resolved) shear stress

θ = orientation of normal to slip plane w/r compressive load axis

ψ = orientation of slip direction w/r compressive load axis

Equation (3.1) is the critical resolved shear stress criterion and, like the maximum shear stress criterion, it predicts that failure occurs at the same level of either compressive or tensile load.

A modification of the critical resolved shear stress criterion to account for the effects of normal stresses on slip planes leads to predictions of different compressive and tensile stresses for failure [46]. However, despite the different magnitudes of tensile versus compressive stresses required to fail the material by shear slip mechanisms, the appearance of the deformed material, i.e., the slip band, is the same for each type of load.

When anisotropic materials are uniaxially compressed along a direction parallel to planes of easy shear slip, infinitely large compressive stresses are required to cause simple shear failure along these planes. This prediction is easily verified by considering the magnitude of the stress calculated using (3.1) as θ approaches 90° . Under these conditions a new mechanism of failure must prevail; the most commonly observed mode is the formation of kink bands.

First described by Orowan [47], kink bands are deformation bands that result from the cooperative buckling of the planes of easy shear slip. Such bands form by the rotation of planes of easy shear slip away from the compression axis with concomitant shear deformation between these planes. The formation of a kink band by this mechanism is illustrated in Figure 3.1. Although kink bands form when compressive loads are applied parallel to the planes of easy shear slip, this mode of failure does not operate when tensile stresses are applied along the same direction. Therefore, the loading of an anisotropic material parallel to planes of easy shear slip results in different magnitudes of tensile and compressive strengths as well as different modes of failure in tension and compression.

Studies of the axial compressive behavior of high performance PPTA fibers show that the axial compressive strength of these fibers is only 20% of their axial tensile strength [17]. Furthermore, the PPTA fiber fails in axial tension by longitudinal splitting [33,43], but fails in axial compression by kink band formation [17,20,21,37].

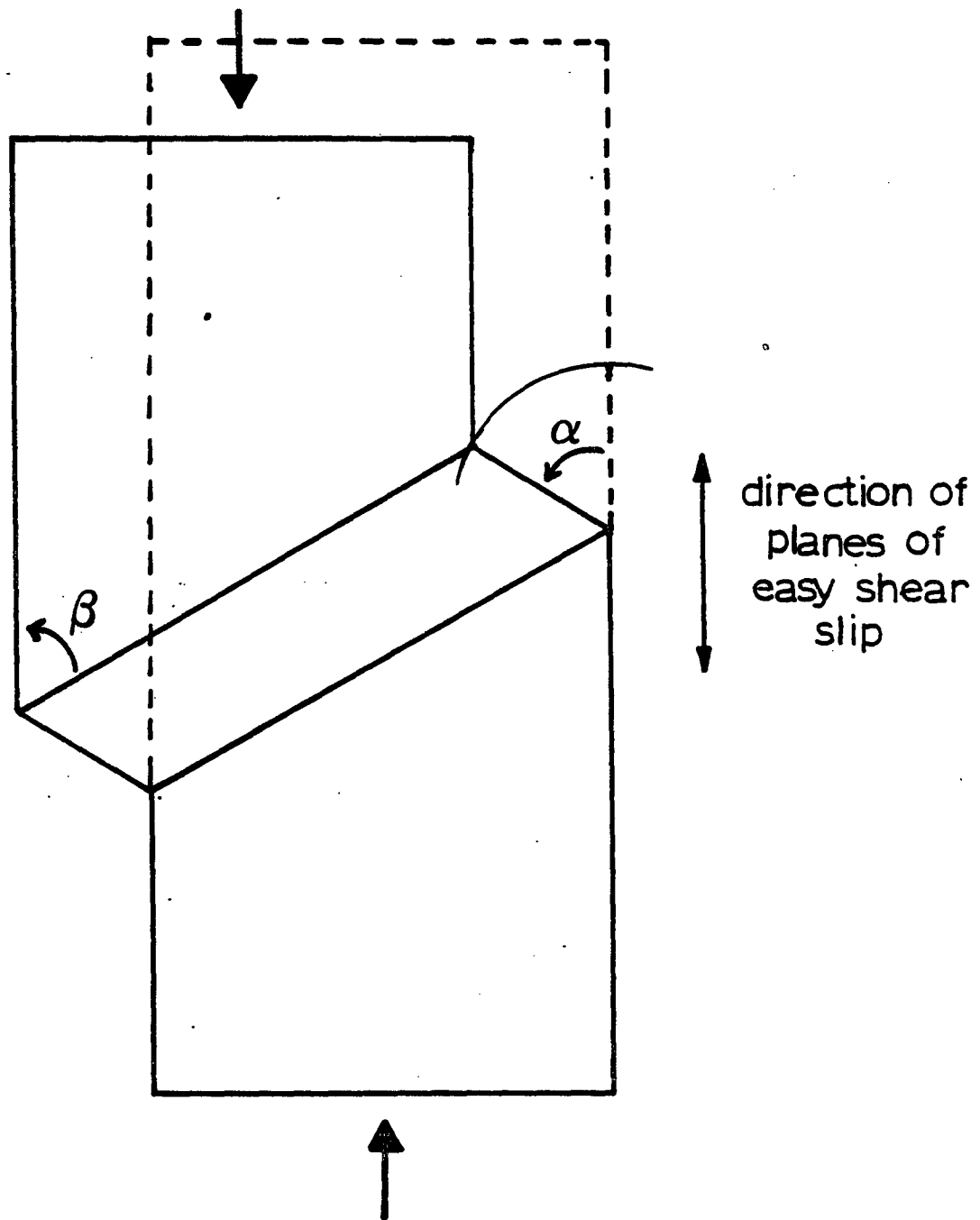


Figure 3.1. Schematic of ideal kink band.

Recognizing that planes of easy shear slip in PPTA fibers must be parallel to the extended PPTA chain axis, and therefore parallel to the fiber axis, it appears that kink band formation in axially compressed PPTA fibers occurs by the mechanism advanced by Orowan.

Orowan proposed the mechanism of kink based formation based on observations of compressed metal single crystals [47]. Zaukelies demonstrated that this mechanism applied to the formation of kink bands in axially compressed oriented nylon, specifically for the compression of nylon crystal planes of easy shear slip [48]. More recently, kink band formation by shear slip between crystallographic planes has been proposed for several axially compressed oriented polymers [37,49-52].

Orowan originally proposed the formation of kink bands by buckling of "lamellae" planes of easy shear slip, emphasizing that these lamellae planes need not be atomic planes [47]. Kink bands have been observed in compressed wood [53,54], rock [55], card decks [56], rubber laminates [57], and fiber-reinforced composites [58-63]. In these anisotropic materials, kink bands formed after compression parallel to material planes of easy shear slip that are much larger than atomic scale. Therefore, it appears that Orowan's theory can be applied to kink band formation due to shear slippage between buckled planes on several levels of structural scale.

To develop a theory for predicting the compressive strengths of materials that fail due to the formation of kink bands, it is necessary to closely examine the stages of kink band development. In all studies where these stages were examined, the results showed that there was a

nucleation of the band in a small region of the compressed material followed by kink band propagation with further compression [21,41,47,50,55-57,59,61-65].

Independent studies of kink band formation in oriented polymers [65], card decks [56], and rubber laminates [57] where the nucleation region was closely examined showed that local material buckling preceded the collapse into a propagating kink band. Indeed, it is remarkable that the schematic representations of the process of kink band formation presented in each study are virtually identical. One of these representations is shown in Figure 3.2.

In this chapter, a theory based on elastic microbuckling instabilities for predicting the axial compressive strengths of extended-chain polymers is developed. In light of the evidence presented for the mechanism of kink band formation, it is believed that the critical compressive stress that initiates local buckling instabilities which subsequently lead to kink band formation in anisotropic materials is the compressive strength of these materials. Critical compressive stresses can be calculated using an energy method for elastic instability analysis. A brief description of the energy method is presented in the following section.

3.2 The Energy Method for Determination of Elastic Stability

The problem of mechanical stability can be approached using an energy method that is completely analogous to thermodynamic stability

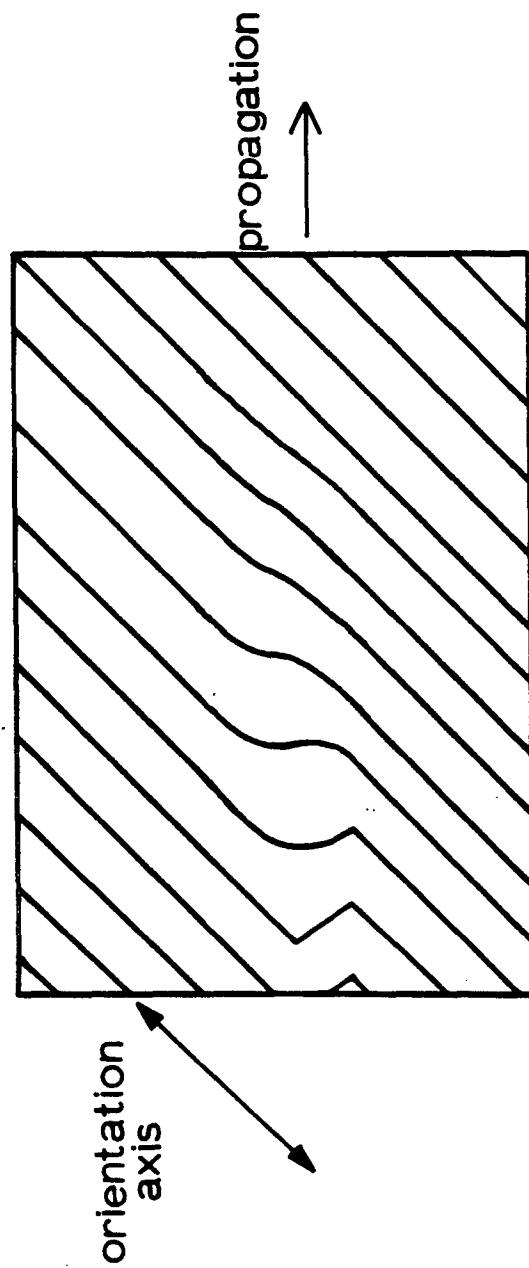


Figure 3.2. Representation of stages of kink band formation. (Adapted from [65])

criteria for phenomena such as phase transitions. The following discussion of mechanical stability will be limited to static equilibria of linear-elastic systems.

The stability of a structure subjected to external loads can be analyzed by assuming modes of deformation and the existence of a function V called the total potential. This function is defined as the sum of the internal potential energy U (strain energy) and the potential energy Ω of the external forces that act on the structure:

$$V = U + \Omega \quad (3.2)$$

The work done on the structure by the external forces is defined as a loss in potential energy:

$$\Omega = -W \quad (3.3)$$

Therefore (3.2) can be written as:

$$V = U - W \quad (3.4)$$

For static equilibrium of the structure, the change in the total potential V with respect to any deformation must be zero:

$$\partial V = \partial U - \partial W = 0 \quad (3.5)$$

Only the assumed deformation modes which satisfy (3.5) are allowable. Furthermore, the equilibrium condition (3.5) gives discrete or critical values of external loads that deform the structure into these allowable modes.

The type of equilibrium (stable, metastable or unstable) for each deformation mode and critical load can be ascertained from the second variation of the total potential V . The three types of equilibrium are

illustrated by the rigid ball analogy shown in Figure 3.3. The critical loads which result in a loss of stability are obtained in this manner.

To understand this method of determining mechanical stability, consider the collapse, due to a compressive load, of a rigid bar that is supported at its base by a linear-elastic hinge. This problem is illustrated in Figure 3.4. Under an axial load P the bar should remain vertical. However, if a small perturbation causes the bar to rotate away from the vertical through a small angle α , a critical value of P exists which makes the structure unstable to such perturbations.

The total potential of the structure shown in Figure 3.4 is:

$$V = \frac{k}{2} \alpha^2 - P \Delta \ell \quad (3.6)$$

where the first term on the right side of (3.6) is the strain energy of the elastic hinge and the second term is the work done by load P through the distance $\Delta \ell$. From the geometry of the problem illustrated in Figure 3.4, it is seen that this distance $\Delta \ell$ is:

$$\Delta \ell = \ell(1 - \cos \alpha) \quad (3.7)$$

which, for small α , is approximated by:

$$\Delta \ell \approx \frac{\ell \alpha^2}{2} \quad (3.8)$$

Substitution of (3.8) into (3.6) yields:

$$V = \frac{k \alpha^2}{2} - \frac{P \ell \alpha^2}{2} \quad (3.9)$$

The equilibrium of the system is given by:

$$\frac{\partial V}{\partial \alpha} = (k - P \ell) \alpha = 0 \quad (3.10)$$


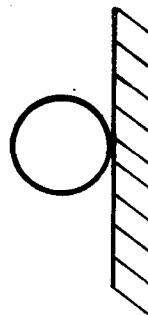
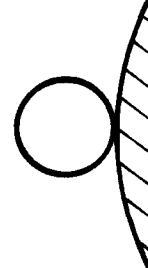
Total potential	Equilibrium		
$V = U - W$	$\partial V = \partial U - \partial W = 0$		
	Stability		
	$\partial^2 V$		
			
stable $\partial^2 V > 0$	metastable $\partial^2 V = 0$	unstable $\partial^2 V < 0$	

Figure 3.3. Rigid ball analogy of the three types of mechanical equilibrium.

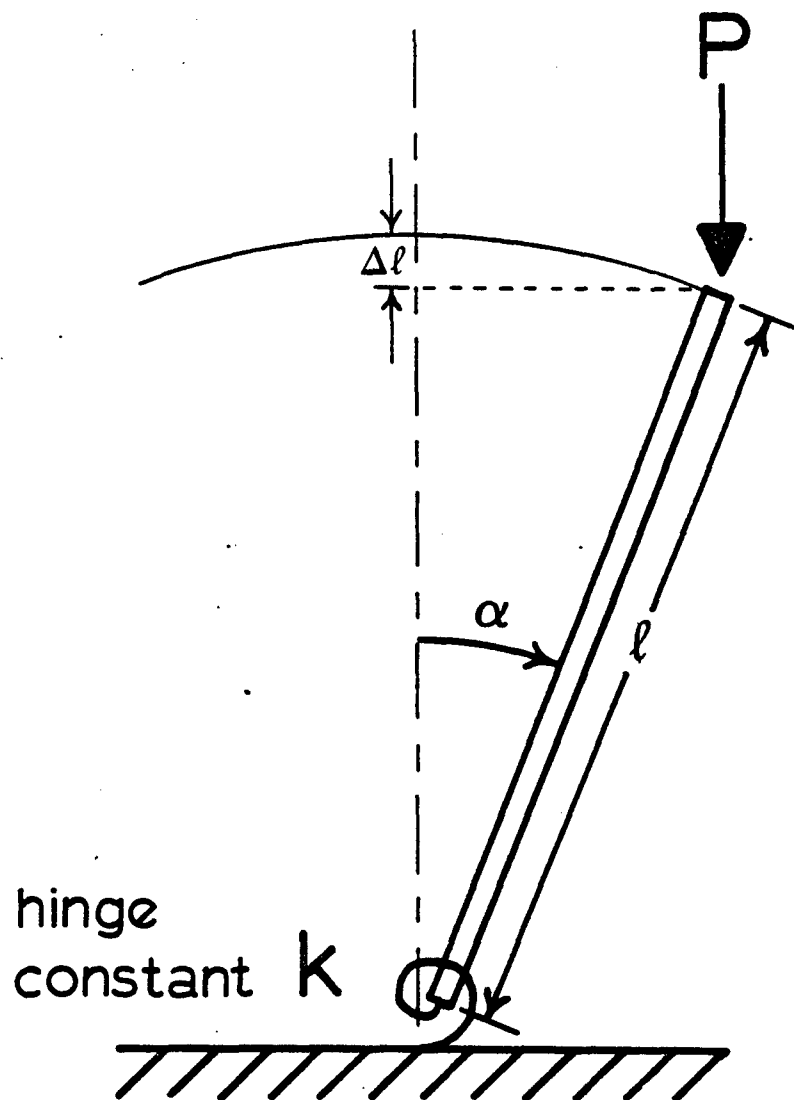


Figure 3.4. Illustration of stability problem of a rigid bar supported at its base by an elastic hinge.

Equation (3.10) is satisfied when $\alpha=0$ or $P = \frac{k}{\ell}$. These two equilibrium conditions correspond to the cases where the bar remains vertical for any load P or the bar rotates to any arbitrary angle α at a particular value of P , respectively. The existence of two equilibrium deformation modes at the critical load $P=k/\ell$ is referred to as a bifurcation point.

Analysis of the second variation of the total potential given by:

$$\frac{\partial^2 V}{\partial \alpha^2} = (k - P\ell) \quad (3.11)$$

shows that the system becomes metastable when the load reaches the critical value $P_{cr} = k/\ell$. The metastable condition dictates that all rotations α are energetically equal and therefore, small perturbations of the bar under load P_{cr} can result in large rotations, i.e., collapse. Furthermore, the equilibrium condition corresponding to the bar remaining vertical at any load becomes an unstable equilibrium when $P > P_{cr}$ as verified by inspection of (3.11).

The steps involved in the energy analysis of elastic stability can be summarized as follows:

1. Given a structure that is subjected to external forces, assume probable modes of deformation.
2. Write the total potential function V (3.4) of the system for the assumed deformation modes.
3. Determine the values of the external loads and the modes of deformation which satisfy the equilibrium condition (3.5).
4. Establish the type of equilibrium for each loading condition determined in step 3 from the second variation of V , thereby determining which are the critical loads that result in loss of stability.

In the following sections, a simple mechanical model is introduced to predict the compressive buckling loads of a single, extended polymer chain. Analysis of this model leads to a relationship between the bending rigidity of an extended chain and the force constants for bond angle deformations. The results for a single chain are then applied to a collection of such chains that interact through lateral bonding. The load required to buckle this collection of oriented chains is calculated as an estimate of the axial compressive strength of high performance polymer fibers.

3.3 Rigid-Link Elastic-Hinge Model for a Single Extended Polymer Chain

The mechanical modelling of chemical bonds between atoms and molecules with springs has been a popular concept (refer to any standard Physical Chemistry text). Indeed, the calculations of theoretical moduli of extended polymer chains involve treating the chain as a series of elastic springs connected by elastic hinges. One of the first calculations of axial modulus of long chain molecules was made by Mark [66], and since then has been performed by many others for several polymers. Force constants for the springs and hinges are obtained from infrared spectroscopy measurements of force constants for bond stretching and bond angle bending, respectively. For small deflections about equilibrium positions, the bonding potential energy profile is assumed to be parabolic so that forces are proportional to deflections. This assumption of linear springs results in equivalent calculated tensile and compressive moduli.

Under compression, a long and stiff polymer chain can become unstable and buckle in a manner similar to the buckling of a long slender column. Buckling of a chain can occur by bending of bond valence angles and/or bond rotation (torsion). Even if these deformations were only slight deviations from equilibrium positions, the summation of them all along a large section of the chain could result in significant chain axis curvature. The force constants for each type of deformation provide a measure of the resistance of an extended chain to buckling and the total effect could be considered a "bending rigidity" of the chain. If it is possible to obtain a measure of this bending rigidity, then the application of classical instability analysis can provide an estimate of the compressive load required to initiate chain buckling.

As in calculations of theoretical moduli, buckling loads are to be calculated for static conditions by assuming bond lengths, bond angles, and force constants remain at their respective equilibrium values. The actual values of equilibrium bond lengths and angles and the orientations of bonds with respect to the chain axis differ for each polymer, and to take these specific geometric factors into consideration is beyond the scope of this dissertation. It is emphasized that consideration of these factors will improve the predictive power of the model, but to introduce the concept of elastic buckling instabilities in fully-extended polymer chains under axial compression the following simplifying assumptions will be applied to the model. The polymer chain consists of p rigid links of equal length ℓ oriented along the chain axis,

which are connected by $p-1$ linear-elastic hinges of equal stiffness k . A representation of the model is shown in Figure 3.5.

In the model, covalent bonds have been replaced with rigid links for two reasons. First, tabulated values of force constants indicate that bond stretching constants are at least an order of magnitude greater than torsion and bending constants [25,67]. Therefore, most of the deformation in a compressed and buckled chain is primarily due to bond angle changes. Second, the axial deformation of a buckled chain is negligible compared to the displacement due to bending the chain. Therefore, the contour length of a chain does not change with buckling. This assumption of "axial rigidity" is also made in the classical analysis of column buckling.

The elastic hinges represent both the bending of valence bond angles and bond rotation. If bending deflections are small, the hinges can be considered linear-elastic.

To calculate a critical buckling load for a link-hinge chain having p links and $p-1$ hinges using the energy method, it is assumed that buckling occurs by lateral displacement of the chain from the load axis. This lateral displacement is defined by values of angular rotation α_i for each hinge as shown in Figure 3.7.

Next, the total potential V is set equal to the difference between the sum of strain energies for all the deformed hinges and the work done by load P through the total axial displacement that results from chain buckling. The equilibrium of the potential V is determined with respect

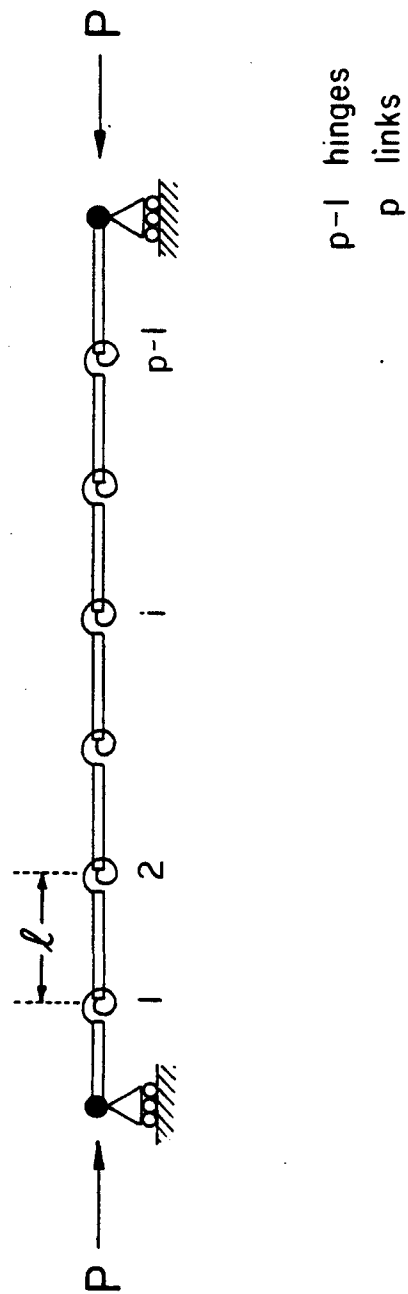


Figure 3.5. Representation of the link-hinge chain model for an extended polymer chain.

to each hinge rotation; i.e., the equations obtained from $\frac{\partial V}{\partial \alpha_i}$ are all set equal to zero. Therefore, the equilibrium condition yields a system of $p-1$ linear and homogeneous equations with variables α_i and coefficients that are functions of P , k and ℓ . The determination of the loads P which satisfy the equilibrium condition is an eigenvalue problem with $p-1$ degrees of freedom. The $p-1$ eigenvalues of P obtained from the non-trivial solution of the $p-1$ linear and homogeneous equations are the compressive loads that cause buckling. The minimum positive eigenvalue is the critical buckling load P_{cr} . An example of the application of the energy method to the buckling of a chain with four links is given in Appendix I.

The calculated critical loads for any value of p are all of the form:

$$P_{cr} = A_p \left(\frac{k}{\ell} \right) \quad (3.12)$$

where the coefficient A_p is a function of p only. Values of A_p for p ranging from 2 to 7 are given in Table 3.1. These results show that the critical buckling load decreases with increasing chain length.

In performing the calculation of critical loads by energy analysis of each hinge, it becomes evident that the computation difficulty increases rapidly with increasing model chain size. In other words, for a chain with p links the determinant of a $(p-1) \times (p-1)$ matrix must be found, and after setting this determinant equal to zero the roots of the resulting $(p-1)$ th order polynomial must be determined. So that the buckling analysis may be applied to polymer chains where p is very

Table 3.1

Comparison of Critical Buckling Loads of Link-Hinge Chains
Calculated From Exact Analysis and From Approximate Formula

p	A_p	$(\frac{\pi}{p})^2$	$\frac{A_p}{(\pi/p)^2}$
2	2	2.4674	0.811
3	1	1.0966	0.912
4	0.5858	0.6169	0.950
5	0.3820	0.3948	0.968
6	0.2680	0.2742	0.977
7	0.1981	0.2014	0.983

$$p_{cr}^{exact} = A_p \left(\frac{k}{\ell} \right)$$

$$p_{cr}^{approx} = \left(\frac{\pi}{p} \right)^2 \left(\frac{k}{\ell} \right)$$

large, a single approximate relationship between the critical buckling load and the values p , k , and ℓ is derived in the next section.

3.4 Approximate Buckling Load Formula For Long Link-Hinge Chains

Intuitively, it appears that the buckled shape of a long link-hinge chain (p large) should be similar to the shape of a buckled elastic column of the same length and with the same end restraints. This analogy is illustrated in Figure 3.6.

Timoshenko and Gere [68] have shown that the strain energy of a buckled slender column (Figure 3.6a) is given by:

$$U = \frac{EI}{2} \int_0^L \left(\frac{d^2 v}{dx^2} \right)^2 dx \quad (3.13)$$

where EI is the bending rigidity of the column and $v=v(x)$ is the curve describing the lateral displacement (deformation) of the buckled column.

The work due to load P acting through the axial displacement that results from buckling is:

$$W = P\Delta\ell = \frac{P}{2} \int_0^L \left(\frac{dv}{dx} \right)^2 dx \quad (3.14)$$

In classical buckling instability analysis of a slender column with pinned ends, the deformation pattern due to buckling is a sine wave that is described by:

$$v(x) = B \sin\left(\frac{\pi x}{L}\right) \quad (3.15)$$

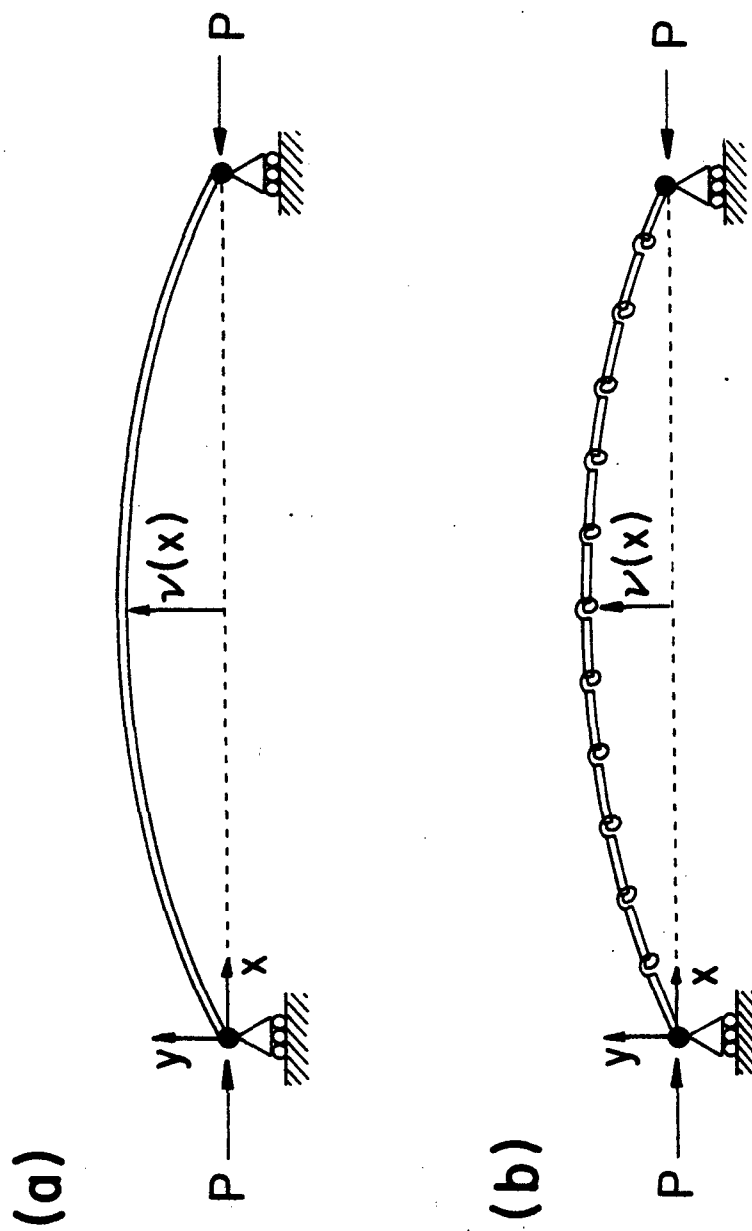


Figure 3.6. Postbuckled shapes of: (a) a slender column and (b) a long link-hinge chain.

Substitution of (3.15) into (3.13) and (3.14) yields:

$$U = \frac{EI\pi^4 B^2}{4L^3} \quad (3.16)$$

$$W = \frac{P\pi^2 B^2}{4L} \quad (3.17)$$

The variation of these quantities with respect to the assumed deformation mode (3.15) is simply the variation taken with respect to B , the amplitude of the sine wave that describes that lateral deflection of the buckled column:

$$\partial U = \frac{EI\pi^4 B}{2L^3} \partial B \quad (3.18)$$

$$\partial W = \frac{P\pi^2 B}{2L} \partial B \quad (3.19)$$

At equilibrium:

$$\frac{\partial V}{\partial B} = \left(\frac{EI\pi^4}{2L^3} - \frac{P\pi^2}{2L} \right) B = 0 \quad (3.20)$$

which is satisfied when either $B=0$ (no buckling) or when the load reaches the value:

$$P_{cr} = \frac{\pi^2 EI}{L^2} \quad (3.21)$$

Equation (3.21) is the well-known Euler formula for the buckling load of a slender column with pinned ends. It is readily verified from the second variation of V that this load P_{cr} results in a metastable

equilibrium for any deflection, i.e., any value B . Furthermore, loads greater than the value given by (3.21) result in unstable equilibrium if the column remains undeflected ($B=0$).

The analogy between buckling of slender columns and buckling of long link-hinge chains is made by assuming that the shape (deformation) of the buckled chain approaches that of the buckled column as the number of chain links p increases. The shape of the buckled chain is described by the angles $\alpha_i = \alpha(x_i)$ that are defined with respect to the coordinate system depicted in Figure 3.7.

Referring to Figure 3.7b, it is seen that the strain energy of bending at hinge i is:

$$U_i = \frac{k}{2}(\alpha_i - \alpha_{i-1})^2 \quad (3.22)$$

The strain energy for the whole link-hinge chain is:

$$U = \sum_{i=1}^{p-1} U_i = \frac{k}{2} \sum_{i=1}^{p-1} (\alpha_i - \alpha_{i-1})^2 \quad (3.23)$$

The axial displacement due to bending at hinge i is:

$$\Delta l_i = l(1 - \cos \alpha_i) \quad (3.24)$$

which, for small α_i , becomes:

$$\Delta l_i \approx l \left(\frac{\alpha_i^2}{2} \right) \quad (3.25)$$

Therefore, the total axial displacement due to buckling is:

$$\Delta l = \sum_{i=1}^{p-1} \Delta l_i = \frac{1}{2} \sum_{i=1}^{p-1} l \alpha_i^2 \quad (3.26)$$

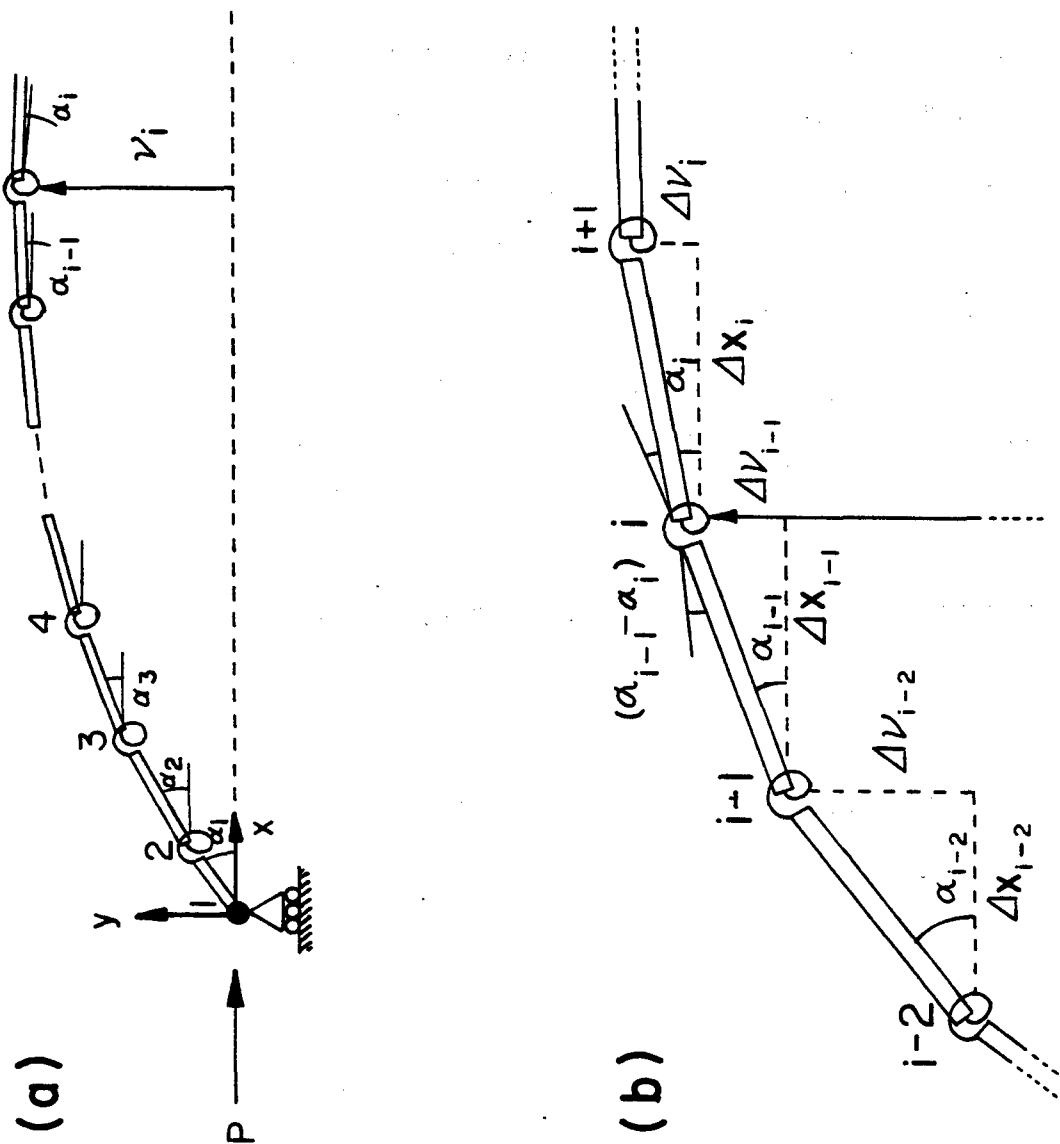


Figure 3.7

(a) Coordinates describing shape of buckled link-hinge chain. (b) Expanded view of chain in vicinity of hinge i .

The work due to load P acting through this total displacement is:

$$W = P\Delta\ell = \frac{P}{2} \sum_{i=1}^{p-1} \ell \alpha_i^2 \quad (3.27)$$

From examination of Figure 3.7b it is clear that:

$$\ell \cos \alpha_i = \Delta x_i \quad (3.28)$$

which, for small α_i , becomes:

$$\ell \approx \Delta x_i \quad (3.29)$$

If (3.23) is multiplied by (ℓ/ℓ) , the result is:

$$U = \left(\frac{\ell}{2}\right) \frac{k}{2} \sum_{i=1}^{p-1} (\alpha_i - \alpha_{i-1})^2 = \frac{k}{2\ell} \sum_{i=1}^{p-1} (\alpha_i - \alpha_{i-1})^2 \ell \quad (3.30)$$

and substitution of (3.29) yields:

$$U = \frac{k}{2\ell} \sum_{i=1}^{p-1} (\alpha_i - \alpha_{i-1})^2 \Delta x_i \quad (3.31)$$

Similarly substitution of (3.29) into (3.27) yields:

$$W = \frac{P}{2} \sum_{i=1}^{p-1} \alpha_i^2 \Delta x_i \quad (3.32)$$

Recalling the definition of a Riemann integral:

$$\lim_{n \rightarrow \infty} \sum_{i=1}^n f(w_i) \Delta x = \int_a^b f(x) dx \quad (3.33)$$

where w_i is any point in the subinterval $[x_{i-1}, x_i]$, then in the limit of an infinite number of links p , equations (3.31) and (3.32) converge to the following definite integrals:

$$U = \frac{k}{2\ell} \int_0^L (\alpha_i - \alpha_{i-1})^2 dx \quad (3.34)$$

$$W = \frac{p}{2} \int_0^L \alpha_i^2 dx \quad (3.35)$$

It is verified from inspection of Figures 3.6 and 3.7 that any analytical expression $v(x)$ that defines the shape of the buckled link-hinge chain must be related to the quantities $\alpha_i = \alpha(x_i)$. Therefore, in the limit of $p \rightarrow \infty$, the terms in (3.34) and (3.35) that are functions of α_i can be replaced by functions of $v(x)$. The details of the derivation of the relationship between the analytical function $v(x)$ and the angular deformations $\alpha_i = \alpha(x_i)$ are presented in Appendix II. The results show that in the limit of $p \rightarrow \infty$, the first and second derivatives of $v(x)$ are:

$$\left. \frac{dv}{dx} \right|_{x_i} = \alpha_i \quad (3.36)$$

$$\left. \frac{d^2 v}{dx^2} \right|_{x_i} = \frac{\alpha_i - \alpha_{i-1}}{\ell} \quad (3.37)$$

Substitution of (3.37) into (3.34) yields:

$$U = \frac{k\ell}{2} \int_0^L \left(\frac{d^2 v}{dx^2} \right)^2 dx \quad (3.38)$$

which, after substitution of (3.15), gives:

$$U = \frac{k\ell\pi^4 B^2}{4L^3} \quad (3.39)$$

Substitution of (3.36) into (3.35) yields:

$$W = \frac{P}{2} \int_0^L \left(\frac{dv}{dx} \right)^2 dx \quad (3.40)$$

which, after substitution of (3.15), gives:

$$W = \frac{P\pi^2 B^2}{4L} \quad (3.41)$$

After taking the variation of strain energy (3.39) and work (3.41) with respect to the amplitude B of the sine wave that describes the deformation, the equilibrium condition is given by:

$$\frac{\partial V}{\partial B} = \left(\frac{k\ell\pi^4}{2L^3} - \frac{P\pi^2}{2L} \right) B = 0 \quad (3.42)$$

Equation (3.42) is satisfied when $B=0$ or when:

$$P_{cr} = \frac{\pi^2 k\ell}{L^2} \quad (3.43)$$

This axial load sets up a metastable equilibrium in the link-hinge chain, and higher loads cause the undeflected chain ($B=0$) to become unstable.

Equation (3.43) gives the approximate value of critical load required to buckle a long link-hinge chain. This equation is completely analogous to the formula for the buckling load of a slender column (3.21). Direct comparison of (3.43) with (3.21) shows that the bending rigidity of the link-hinge chain is $k\ell$. The dimensions of this product are equivalent to those of column bending rigidity EI , namely (force)(length)².

The validity of using the approximate equation to predict the critical buckling load of the link-hinge chain can be demonstrated by

comparing values of P_{cr} calculated using (3.43) with the exact values calculated in Section 3.3 for several values of p . By noting that $L=p\ell$, where L is the overall chain length, equation (3.43) can be modified to give:

$$P_{cr} = \left(\frac{\pi}{p}\right)^2 \left(\frac{k}{\ell}\right). \quad (3.44)$$

This equation allows a direct comparison between the coefficient $(\pi/p)^2$ and the coefficient A_p defined in equation (3.12). The values of these coefficients are given in Table 3.1. Clearly the agreement is very good even for chains of only seven links.

The derived approximate formula (3.43) is significant because it allows calculation of critical buckling loads for a polymer chain (given the imposed assumptions) from bond bending and torsion force constants, bond lengths, and total chain length. It also demonstrates that the bending rigidity of such a chain is a function of the resistance to bond angle deformation and the length of the bonds along the chain axis.

Inspection of (3.43) will reveal that the buckling loads diminish rapidly with chain length. This result, which neglects the effects of interchain interaction, predicts extremely low compressive strengths for polymer chains of only average molecular weight. As an example, the compressive strength of PPTA fibers will be calculated using (3.43).

Because a buckled chain can only support a load which is equal to the critical load, the load required to buckle a collection of non-interacting chains, regardless whether the chains buckle one at a time or all at the same instant, is simply the sum of the buckling loads for

each chain. Therefore, the critical stress for buckling a single chain is equal to the buckling stress for any collection of laterally non-interacting chains. A stress calculated in this manner can be used as an estimate of the compressive strength of a fiber having relatively poor lateral strength and stiffness.

Typical force constants for bond angle bending are $k=0.5 \times 10^{-18}$ J-rad⁻¹ [67]. Most covalent bond lengths are approximately 1Å. The average length of a PPTA molecule is 2100Å [33,34] and the cross-sectional area per chain in the unit cell is 20.24Å² [25]. Using (3.43), a critical stress of only 0.06 MPa is calculated. This estimate is compared to the measured compressive strength of 700 MPa (Chapter 2). Clearly, in order to predict the compressive strength of a fiber composed of highly oriented and fully extended chains, interchain interactions must be considered.

3.5 Buckling of Laterally Interacting Link-Hinge Chains: Predictions of High Performance Fiber Compressive Strength

The lateral interactions between linear polymer chains in high performance fibers are usually secondary bonding forces. For small deviations away from equilibrium separation, these lateral bonds can be adequately modelled with linear springs. Therefore, when a polymer chain is subjected to an axial compressive load, its tendency to buckle and deflect laterally will be opposed by forces which are approximately proportional to the magnitudes of the lateral displacements.

A collection of fully extended and well-oriented chains that interact as just described can be treated as elastic columns supported by a linear-elastic foundation. The elastic foundation is a hypothetical matrix that has a stiffness that is the sum of the interactions of all the individual lateral bonds. The application of the energy method for determining the buckling loads for elastically supported columns has been reported by Timoshenko and Gere [68]. Their analysis was applied to a single column supported on only one side by an elastic foundation. The extension of this analysis to the buckling of a collection of columns on a foundation has been reported by several investigators as a prediction of the axial compressive strength of unidirectional fiber-reinforced composites [42,69,70]. A similar analysis will be performed here, following especially the work of Rosen [42], in order to calculate the compressive buckling loads of a collection of link-hinge chains that interact laterally. These loads will be used as theoretical estimates of the axial compressive strengths of high performance polymer fibers.

An element of the collection of link-hinge chains which is to be analyzed for compressive buckling instabilities is shown in Figure 3.8. This lattice of perfectly oriented link-hinge chains, all of length L , is assumed to extend over large lateral distances.

To determine, using the energy method, the loads that initiate buckling instabilities in the collection of chains, probable modes of buckling must first be assumed. The shape of each buckled chain can be described by a series of trigonometric functions which are all periodic over length L . For simplicity it is assumed that the buckled shape of

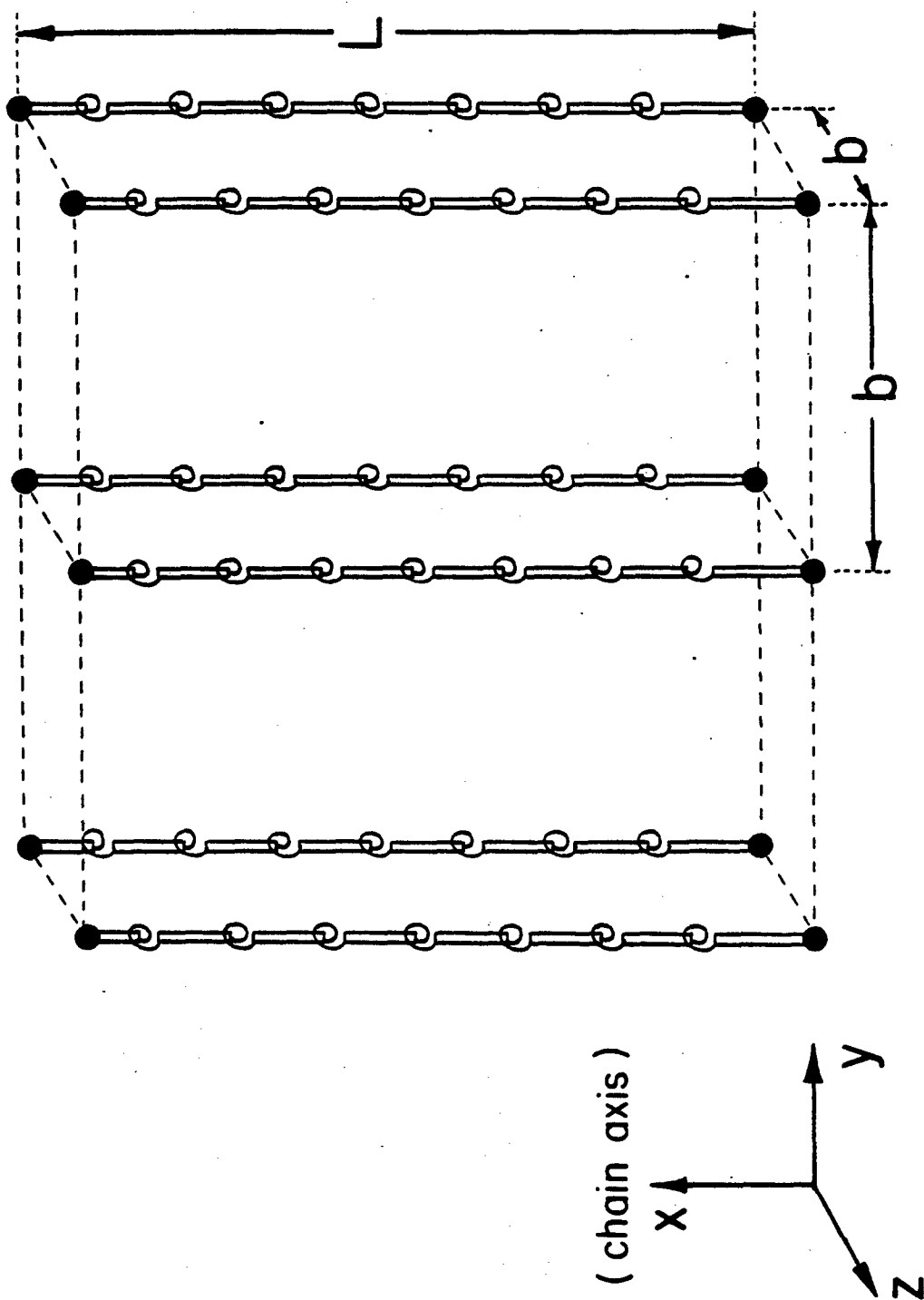


Figure 3.8. Packing geometry for a collection of interacting and perfectly oriented link-hinge chains.

each chain has the same wavelength. Therefore, the only difference between neighboring chains is a phase mismatch. The two extreme cases considered here are when the chains buckle completely in or out of phase as shown in Figure 3.9. These configurations were called extension and shear mode buckling by Rosen because of the nature of deformation in the foundation.

The total potential for the assumed buckling modes is:

$$V = U_1 + U_2 - W \quad (3.46)$$

where U_1 is the strain energy of the buckled chains and U_2 is the additional strain energy of the deformed elastic foundation. The equilibrium condition for this problem is:

$$\partial V = \partial U_1 + \partial U_2 - \partial W = 0 \quad (3.47)$$

The quantities U_1 and W for a single buckled link-hinge chain have been defined earlier (see (3.38) and (3.40)). The equations for the strain energy of the foundation must be derived for each of the two buckling modes. The details of this procedure and the calculation of the critical buckling loads for extension and shear mode buckling are presented in Appendix III. The energy balance is applied to a single chain in the collection, and therefore the calculated critical buckling loads are the loads required to buckle one chain. Because the chain packing within the collection is assumed to be symmetrical and homogeneous, the critical stress for single chain buckling is equal to the critical stress to buckle the whole collection.

The critical stresses for extension mode σ_{cr}^e and shear mode σ_{cr}^s buckling are given by:

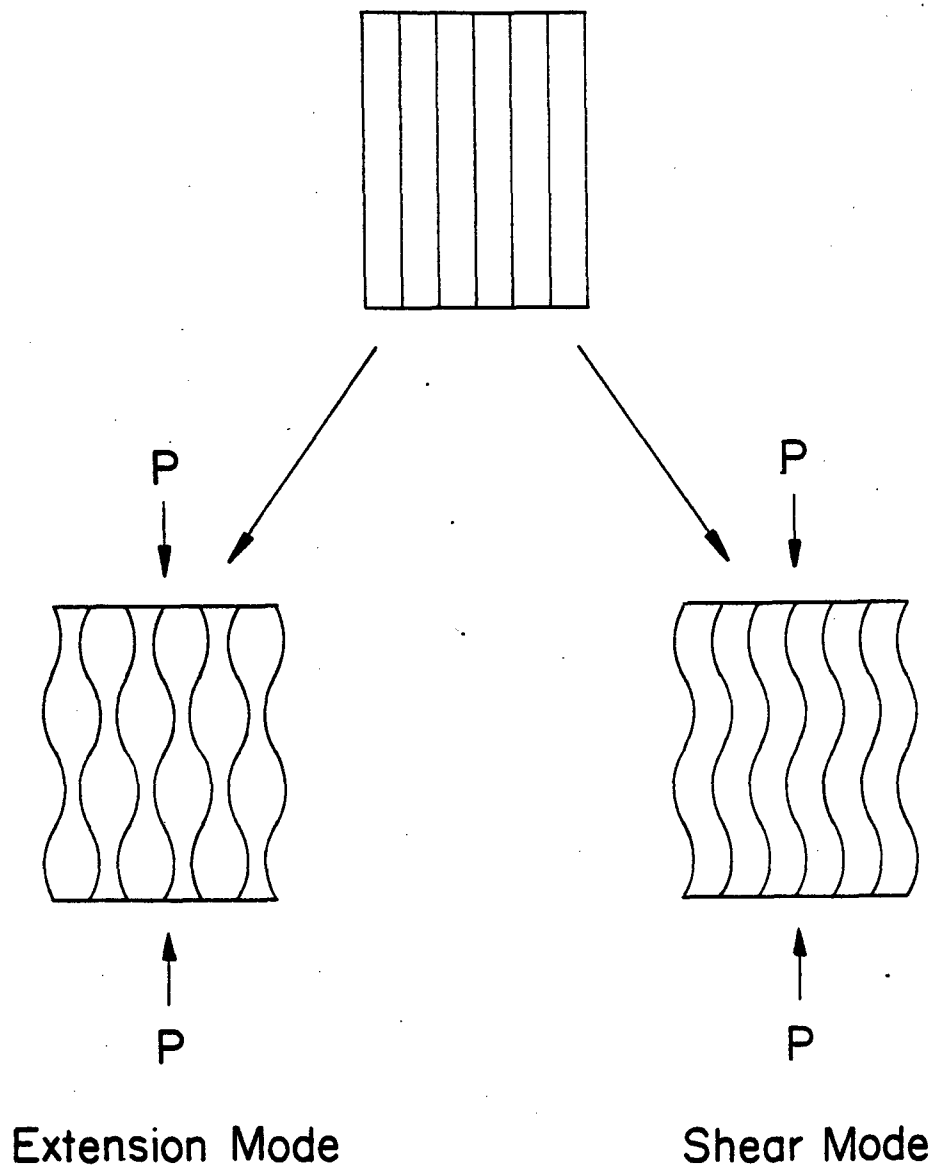


Figure 3.9. Deformations with extension and shear mode buckling of a collection of link-hinge chains. (Adapted from [42])

$$\sigma_{cr}^e = \frac{4\sqrt{E_t k \ell}}{A} \quad (3.48)$$

$$\sigma_{cr}^s = G \quad (3.49)$$

where:

E_t = transverse Young's modulus

A = cross-sectional area per chain

G = longitudinal shear modulus

The values E_t and G are the appropriate elastic constants of the polymer fiber.

These compressive strength predictions are similar to those obtained by Rosen, except for the omission of a "volume fraction" term that is meaningless in the present analysis. The predicted compressive strength of a high performance polymer is the lower value of the strengths given by (3.48) and (3.49).

For the particular case of shear mode buckling, the result (3.49) was obtained by neglecting the bending strain energy of the buckled chain. This condition is valid for long link-hinge chains. Therefore, any assumed buckling pattern that involves only shear deformations of the elastic foundation (i.e., any "in-phase" or cooperative buckling mode) will give the same result for the buckling stress. Examples of several buckling patterns for the collection of long link-hinge chains, which all require a compressive stress equal to the foundation shear modulus to initiate buckling, are illustrated in Figure 3.10. Comparison of these buckling patterns, especially Figure 3.10c, with those observed in the nucleation region of a kink band (Figure 3.2) clearly

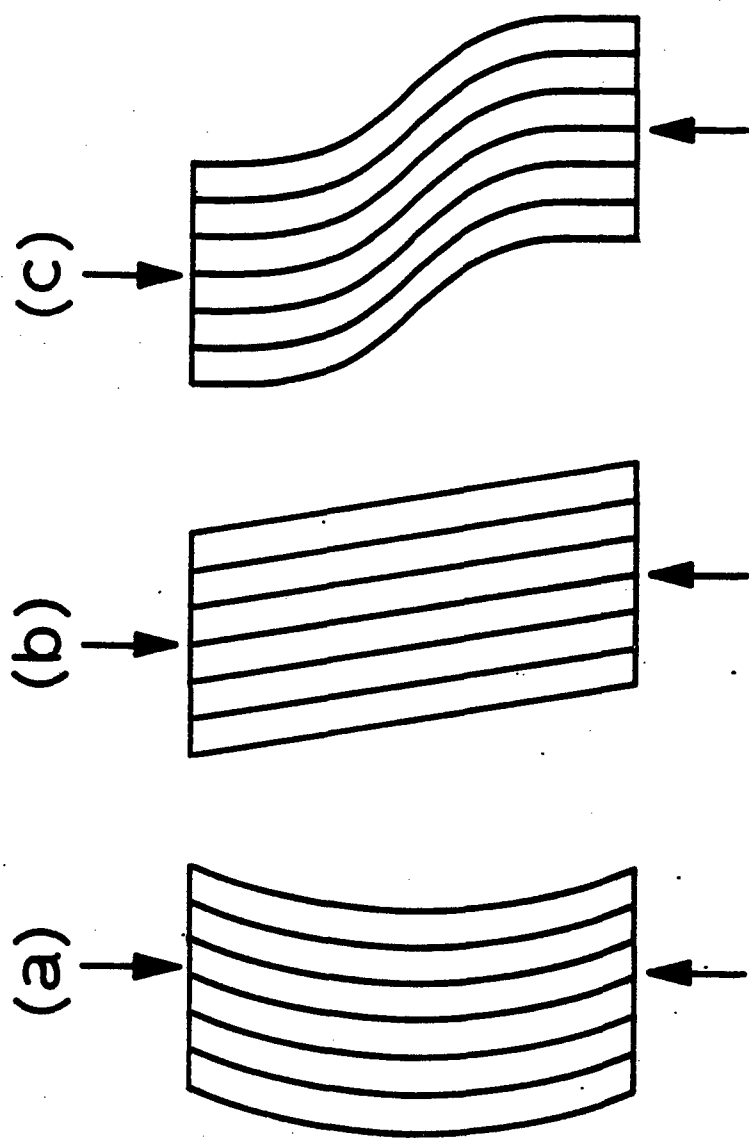


Figure 3.10. Possible shear mode buckling deformations for a collection of long link-hinge chains.

shows the resemblance between experimentally observed deformations and those assumed for shear mode buckling analysis.

3.6 Summary

The use of a rigid link-elastic hinge chain to model the axial compressive behavior of extended polymer molecules permits the calculation of a bending rigidity for single chains. This bending rigidity is the resistance of a polymer chain to bending and buckling, and has been shown to be proportional to valence bond bending and bond torsion force constants. The model can be used to calculate single chain buckling loads for isolated or weakly interacting chains such as in polymer solutions and melts. An example calculation for a PPTA chain gave an estimated buckling stress of only 0.06 MPa. Flow fields which lead to compression or bending of the polymer chains may result in flow instabilities or even chain scission as a result of severe bending.

The compressive stress required to initiate buckling instabilities in a collection of laterally interacting link-hinge chains was calculated as an estimate of the axial compressive strength of high performance polymer fibers. For the case of shear mode buckling, i.e., cooperative buckling of the chains, the compressive strength is predicted to be equal to the longitudinal shear modulus of the fiber.

Examination of several shear mode buckling patterns, all of which require a compressive stress equal to the shear modulus to initiate buckling, showed that this mode of buckling closely resembles the buckling deformation observed for nucleating kink bands [56,57,65].

The analysis presented herein was for the buckling of a collection of polymer chains. The prediction of compressive strength for shear mode buckling was obtained after assuming the support given by the chains against buckling (i.e., the chain bending strain energy) was negligible when compared to the support given by the elastic foundation. This assumption is valid for long chains and it dictates that only the longitudinal shear modulus--and therefore only the lateral interactions between chains, and not the inherent bending rigidity of chains--supports the collection of such chains against buckling. It is easily demonstrated that this prediction also applies to the buckling of long and slender microfibrils, because the buckling load for any single column, chain or microfibril diminishes with the square of the length. Therefore, the analysis of shear mode buckling of a collection of long, slender and rigid microfibrils predicts initiation of buckling at a compressive stress equal to the shear modulus of the "interface" between microfibrils.

The comparison of compressive strengths predicted by the analysis of this simple model with experimentally determined axial compressive strengths of high performance polymer fibers is presented in the following chapter.

CHAPTER IV

THEORETICAL AND MEASURED AXIAL COMPRESSIVE STRENGTHS OF HIGH PERFORMANCE POLYMER FIBERS

4.1 Introduction

The axial compressive load that initiates elastic microbuckling instabilities for laterally interacting extended polymer chains was calculated in Chapter 3, using a simple model for the chains, as an estimate of the axial compressive strength of high performance polymer fibers. Assuming that the degree of interchain interaction can be characterized by the transverse tensile and longitudinal shear moduli of the polymer fiber, the following two equations for critical buckling stresses for a collection of chains were obtained:

$$\sigma_{cr}^e = \frac{4\sqrt{E_t k \ell}}{A} \quad (4.1)$$

$$\sigma_{cr}^s = G \quad (4.2)$$

where E_t = transverse Young's modulus

G = longitudinal shear modulus

A = cross-sectional area of chain

k = force constant for bending or torsion of bonds in backbone of chain

ℓ = covalent bond length in chain backbone

The two calculated critical stresses are for extension mode (uncooperative) buckling σ_{cr}^e and shear mode (cooperative) buckling σ_{cr}^s (see Figure

3.9). The lower of these two calculated stresses is the theoretical estimate of axial compressive strength for any particular fiber.

The validity of these theoretical estimates was examined in this study by measuring the compressive strengths of six high performance fibers.

4.2 Experimental

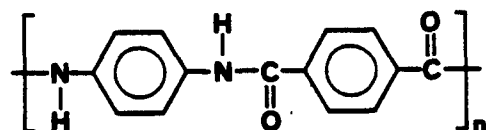
Of the six fibers examined, three are spun from anisotropic solutions of lyotropic liquid crystalline polymers by the dry jet-wet spinning process [5]. These include poly(p-phenylene terephthalamide) (PPTA), poly(p-phenylene benzobisthiazole) (PBT), and poly(2,5-benzoxazole) (ABPBO). All three fibers were tension heat-treated after spinning to improve orientation and thereby increase axial modulus. Kevlar^R 49 was the PPTA fiber selected for this study.

A fiber that is melt-spun from an anisotropic melt of a thermotropic liquid crystalline polymer was also examined. This fiber is a nematic thermotropic polyester (NTP) produced by Celanese Co., and it was also subjected to tension heat-treatment after spinning. The chemical structures of all four liquid crystalline polymers are shown in Figure 4.1.

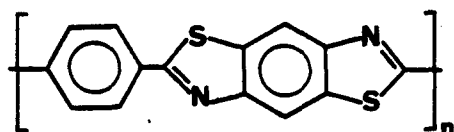
A high modulus/high strength polyethylene (PE) fiber produced by the gel-spinning process [13] was obtained from the Allied Co.

The sixth type of fiber examined is a high-modulus graphite fiber (Union Carbide P-75) that is spun from mesophase pitch. This fiber is stretched during the graphitization process to improve orientation and

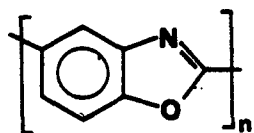
poly (p-phenylene terephthalamide) (PPTA)



poly (p-phenylene benzobisthiazole) (PBT)



poly (2,5-benzoxazole) (ABPBO)



nematic thermotropic polyester (NTP)

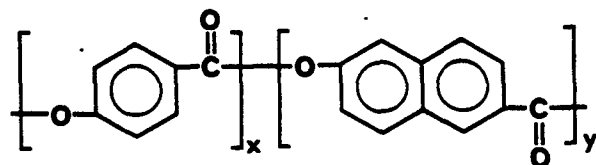


Figure 4.1. Chemical structures of liquid-crystalline polymer fibers.

therefore axial modulus [3,4]. The graphite fiber is included in this study of fiber axial compressive strengths because these fibers generally exhibit a structure of axially oriented microfibrillar graphite ribbons that have the crystalline graphite basal plane oriented parallel to the long axis of the ribbons. In terms of the model proposed for extended chain polymers, the graphite fiber structure can be modelled with laterally interacting extended graphite sheets that may buckle under compression.

The reasons for selecting one particular graphite fiber are two-fold. First, studies of the compressive behavior of graphite fibers show that buckling or kinking occurs only in compressed fibers that have a well-developed and well-oriented graphitic structure [41,71]. These fibers are produced by heat-treatment to 2800°C and they typically exhibit the highest tensile moduli of all graphite fibers. Second, the P-75 fibers appear to have a well-developed radial structure; i.e., the graphite basal planes are oriented predominantly parallel to fiber radii (see Figure 4.2). Therefore, the shear modulus for deformation between graphite basal planes should be nearly equal to the torsion modulus for such fibers. This shear modulus is the estimate of axial compressive strength for graphite fibers that fail due to the shear mode buckling of extended graphite sheets (4.2).

The diameter of fiber samples was measured at several locations along each sample length. The cross-sections of all fibers, except PE, were circular. Therefore, with the exception of PE, all diameters were measured using a laser diffraction technique [72] that yielded values

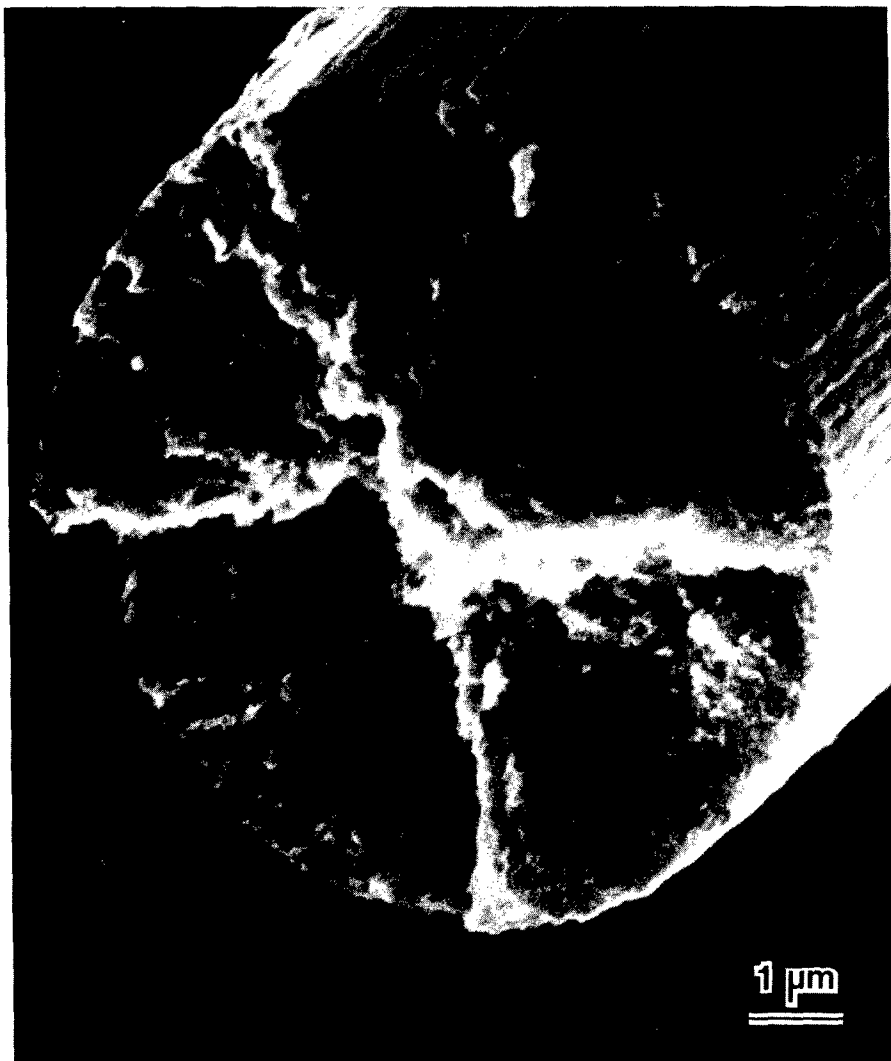


Figure 4.2

SEM micrograph of tensile fracture surface of P-75 graphite fiber.

with a precision of approximately $\pm 2\%$. The diameters obtained from measurements of the laser diffraction pattern are calculated using equations derived for a perfectly reflecting fiber. For some fibers, notably the fine-diameter PPTA, PBT, and ABPBO fibers, the sharpness of the diffraction pattern was enhanced after making the fibers less transparent by coating the samples with a negligibly thin (250\AA) layer of gold using a Polaron sputter coating apparatus. The enhanced diffraction pattern improved the precision of diameter measurements for these three fibers without altering the mean value of diameters measured before and after gold coating. The thin layer of gold on the fiber surface had no measurable effect on the mechanical properties of the fibers.

The PE fibers had an irregular cross-section that varied significantly along sample lengths. The area and shape of each PE fiber sample was determined, after testing, at several locations along the length by embedding the fiber in microtome resin and cutting transverse sections that were subsequently examined using light microscopy. Micrographs of sections cut from locations approximately 2mm apart along the fiber length were used to determine the cross-sectional area of the fiber by a paper-weighing technique. The scale factor for area calibration was obtained from a micrograph of a stage micrometer taken at the same magnification as the fiber cross-section micrographs.

Fibers were mounted onto cardboard tabs with epoxy for mechanical tests [19]. Tensile tests were performed on samples with gage lengths

ranging from 2-8 cm to correct for machine compliance effects [43].

Tensile properties of PE and graphite fibers were obtained from manufacturers.

The torsion modulus of the fibers was measured using a free torsion pendulum [19,74] (see Figure 4.3). The equation for calculating the torsion modulus from measurements of underdamped torsional oscillations of a fiber with circular cross-section is given by:

$$G = \frac{8I_d \ell}{\pi \tau^2 r^4} \left[\pi^2 + \frac{(\ln \Delta)^2}{16} \right] \quad (4.3)$$

where I_d = moment of inertia of disc pendulum

ℓ = sample length

τ = period of oscillation

r = fiber radius

$\ln \Delta$ = logarithmic decrement of amplitude

Torsion pendulum tests were performed at ambient conditions, and damping was noticeable for every fiber tested. However, all values of Δ were found to be >0.5 and therefore, as readily verified from (4.3), the damping had negligible effect on calculated torsion modulus values. Therefore, the torsion modulus was accurately determined using the approximation:

$$G \approx \frac{8\pi I_d \ell}{\tau^2 r^4} \quad (4.4)$$

Fiber samples 2 cm long were set into torsional oscillation by twisting the disc pendulum manually and then carefully releasing the pendulum. This initial twist never exceeded a fiber surface shear

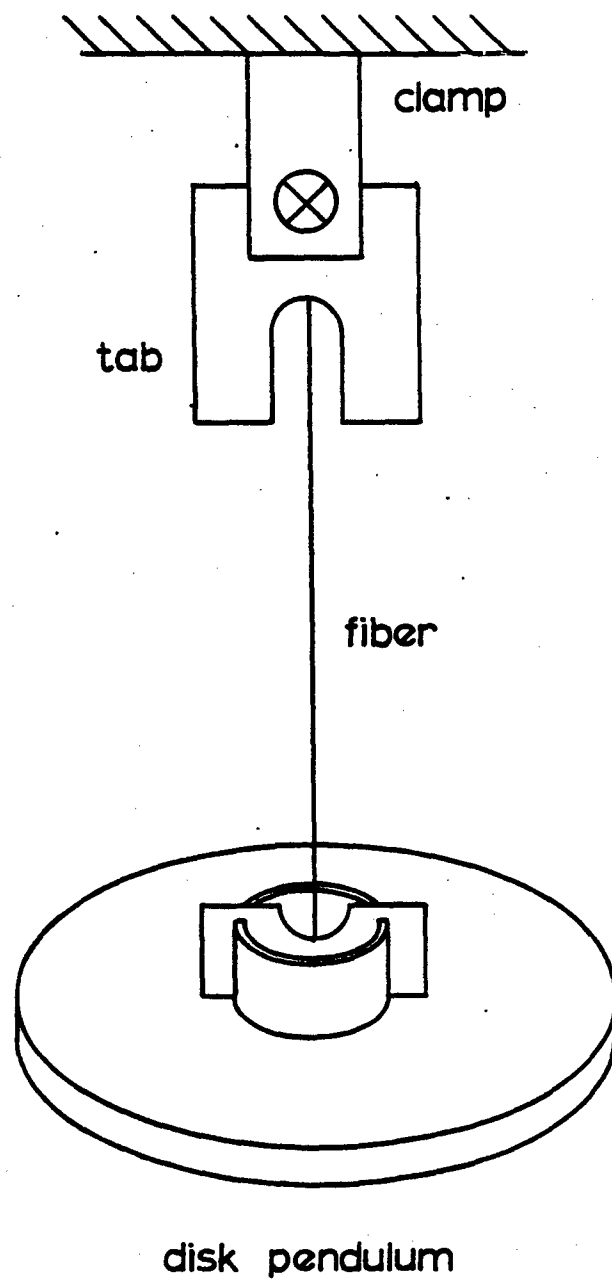


Figure 4.3. Schematic of torsion pendulum apparatus.

strain of 0.5%. The period of oscillation was measured by timing the motion of a mark on the disc pendulum relative to a marked position on a stationary platform placed just beneath the oscillating pendulum.

Two clamp-type aluminum gear blanks were used as disc pendulums. The polar moments of inertia of the two gear blanks were calculated to be 50.3 and 354 g-mm² using dimensions measured with a micrometer (accurate to 1 μ m) and weights measured with an analytical balance. The accuracy of these measurements was checked by using them to calculate densities for aluminum of 2.712 g/cc and 2.717 g/cc, which are in excellent agreement with the actual density of 2.699 g/cc. The large pendulum was used for the PE fiber tests and the small one for all other fiber tests.

The fiber axial compressive strengths were calculated from the product of the compressive strain to kink band formation and the axial tensile modulus. This calculation is based on the assumptions that the fiber is linear-elastic up through the compressive strain for initiation of kink bands and that the axial tensile and compressive moduli are identical. The critical compressive strains to kink band formation were measured using the beam bending technique described in Chapter 2. However, in the tests performed here, fibers bonded to the surface of thick transparent elastic beams were compressed by bending the beam in a cantilever configuration. Cantilever beam bending sets up a linear distribution of longitudinal compressive (and tensile) strains along the beam length as shown in Figure 4.4.

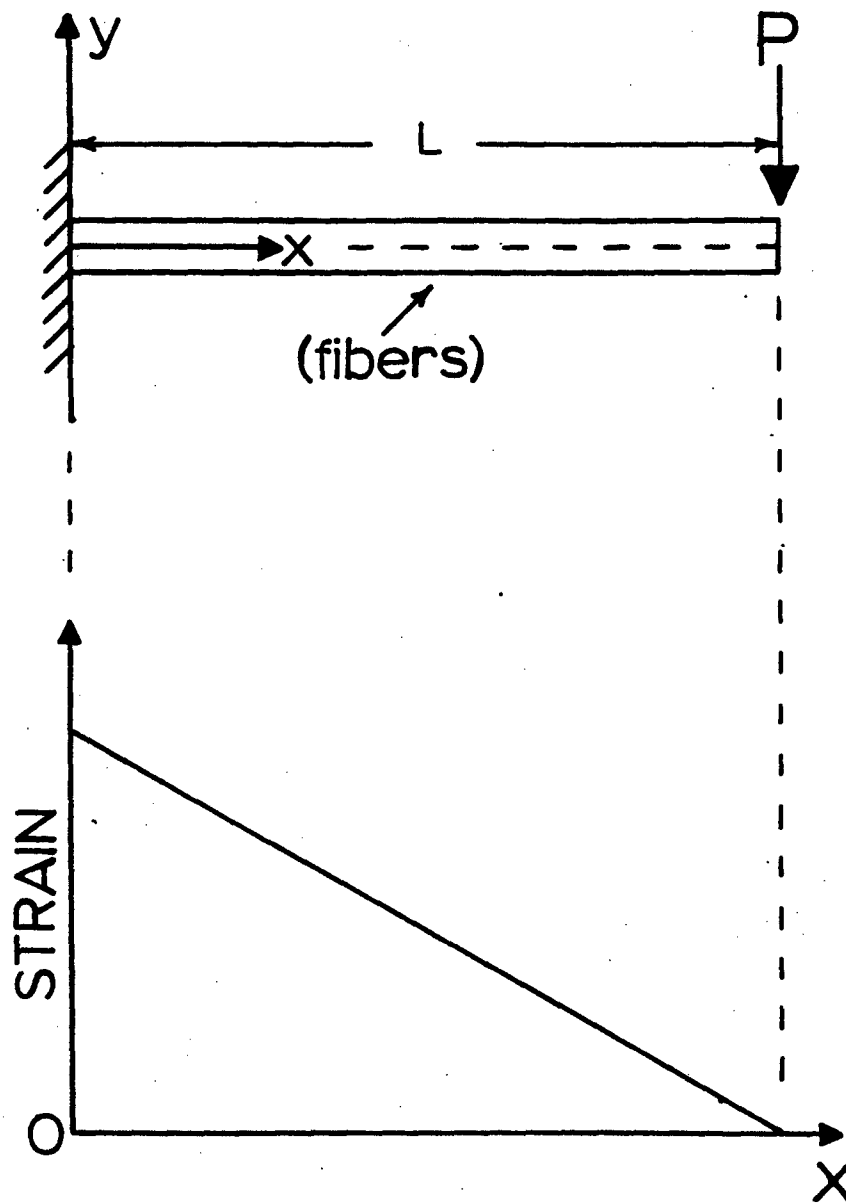


Figure 4.4. Longitudinally distributed axial normal strains in an elastic beam loaded in cantilever bending.

Fibers were examined in the compressed state by holding the beam in the bent configuration during optical microscopic observations. A schematic of a simple rig built for this purpose, which sits on the stage of the optical microscope, is shown in Figure 4.5.

Fibers were mounted under slight tension (0.5g) onto the surface of 1/2 in. x 1/4 in. x ~6 in. Lucite^R beams, parallel to the length of the beams, by applying several coats of Krylon^R Acrylic Spray. Fibers were tested after allowing the acrylic coating to dry to a hard film. It is emphasized that any shrinkage of the film during drying, which might put residual compressive stresses on the bonded fibers, is prevented by using only a thin acrylic coating on a relatively thick beam.

After a beam containing bonded fibers was clamped in the rig as shown in Figure 4.5, a circular wedge was inserted between the beam and the base plate of the rig to deflect the beam. Bonded, compressed fibers were examined in situ using a transmission light microscope. After insertion of a wedge of known diameter v to a distance L measured from the clamped end of the beam, the distance d from the clamped end of the beam to the point along the compressed fiber length where the last kink band was seen was recorded. The compressive strain in the fiber at any point x measured from the clamped end is assumed to be equal to the surface strain $\epsilon(x)$ of the bent beam at the same location. This strain is calculated from:

$$\epsilon(x) = \frac{3tv}{2L^2} \left(1 - \frac{x}{L}\right) \quad (4.5)$$

where t is the thickness of the beam.

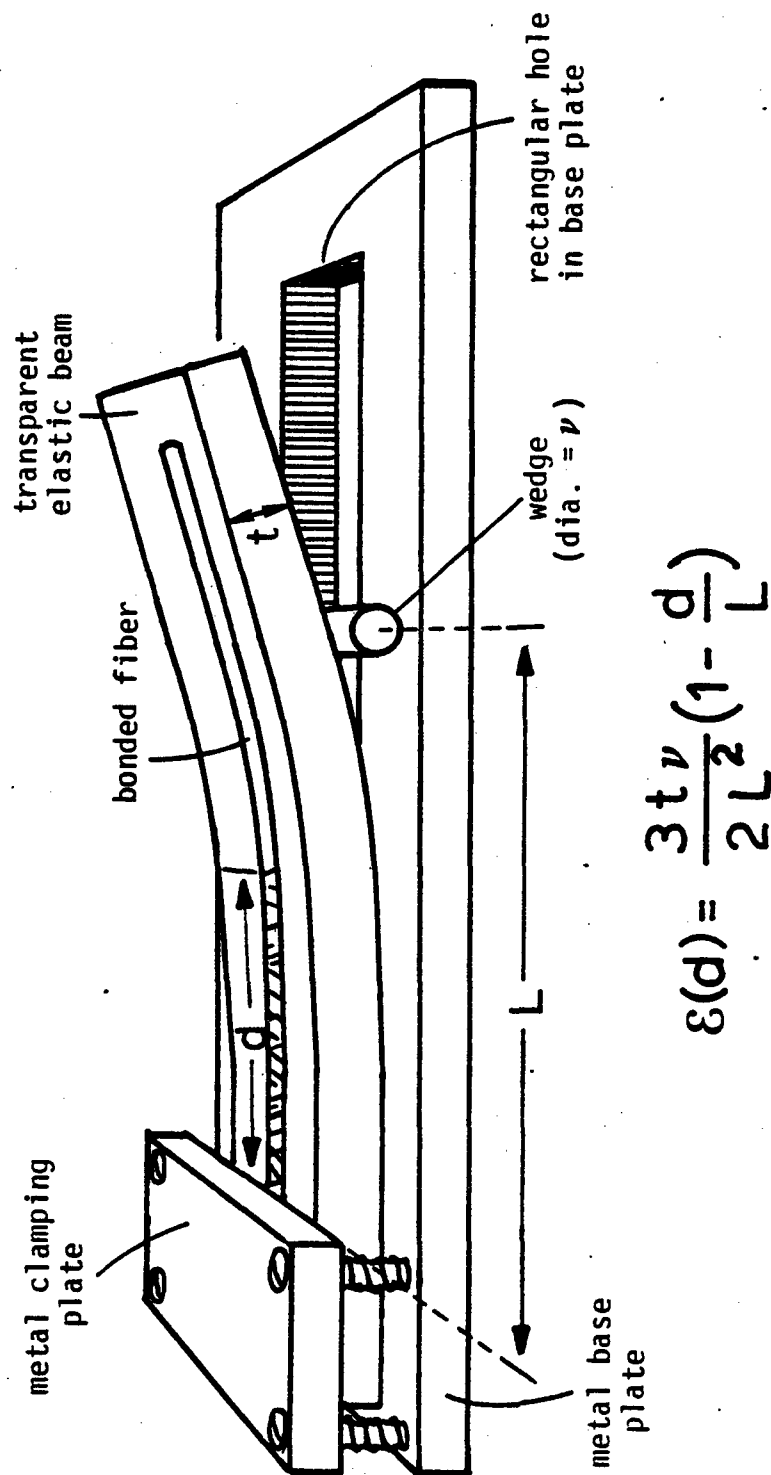


Figure 4.5. Schematic of apparatus for cantilever bending and simultaneous optical microscopic observations of a beam having fibers bonded to its surface.

The critical compressive strain ϵ_c for kink band formation is obtained by substituting $x=d$ into (4.5).

The compressive strain distribution in the fiber could be changed either by using a larger diameter wedge or by moving the wedge closer to the clamped end of the beam (i.e., reduce L). In this manner previously undamaged (unkinked) regions of the bonded fiber could be tested to determine ϵ_c . Thus, several determinations of ϵ_c were obtained from one length of fiber. Because the compressive strain to kink band formation was measured, fibers with irregular cross-section such as the gel-spun PE could be tested with the same accuracy as fibers having circular cross-sections.

Equation (4.5) is derived from linear beam theory, which is based on the assumption of small curvatures for bent beams. Therefore, in all tests performed here, relatively small diameter wedges (i.e., small beam deflections) were held at relatively large distances L so that use of (4.5) to calculate ϵ_c would be valid.

The morphology of compressively kinked fibers was examined using scanning electron microscopy (SEM) and optical microscopy. Kinked fibers were prepared for microscopic observations by using the solvent-cast nylon-6 matrix shrinkage technique for fiber compression described in Chapter 2. However, the relatively thick PE fibers required a thicker film for compression. For these fibers, an approximately 1mm thick layer of Duco^R cement was spread over fibers held aligned on a glass plate. The shrinkage that occurred as the cement dried at room temperature was sufficient to cause kink band formation in the embedded PE

fibers. The surfaces of kinked PE fibers were observed by SEM after dissolving the surrounding Duco cement film with acetone.

Optical microscopic observations of kink band formation at several levels of compressive strain in a single region along a fiber length were made using the cantilever beam bending technique. The strain in one location along a bonded fiber could be increased by simply moving the wedge closer to the clamped end of the beam.

Tensile tests were performed at strain rates of approximately $5 \times 10^{-4} \text{ sec}^{-1}$ using an Instron Universal Testing Machine. A polarizing Zeiss optical microscope was used to examine fibers bonded to bent beams. The surfaces of fibers before and after compression were examined using an ETEC Autoscan SEM.

4.3 Results

The range of diameters and the tensile properties measured for each fiber are listed in Table 4.1. Fibers which were produced in large quantities, namely, PPTA (Kevlar 49), PBT and graphite, exhibited relatively uniform diameters along sample lengths. The filament-to-filament variation in diameter for these three fibers was relatively small. The ABPBO and NTP fibers were produced by laboratory-scale spinning processes and were found to exhibit large variations in diameter, both along the length of one filament and between filaments.

Each type of fiber is one variant of a family which exhibits a wide range of properties that depend on spinning and post heat-treatment conditions. The fibers selected for testing in this study exhibited

Table 4.1
Tensile Properties of Fibers

Fiber	Diameter Range (μm)	Modulus (GPa)	Strength at Break (GPa)
PPTA	11.4-12.8	123 <u>+5.7</u>	3.2 <u>+0.16</u>
PBT	12.4-13.5	265 <u>+15</u>	2.6 <u>+0.20</u>
ABPBO	13.2-18.1	120 <u>+10</u>	3.0 <u>+0.55</u>
NTP	18.7-26.1	77 <u>+2.9</u>	3.2 <u>+0.64</u>
PE	(38)*	117*	2.6*
Graphite	9.7-10.0	500*	2.0*

*Manufacturer's data

+ values are standard deviations.

some of the best tensile properties attainable for each material. Although the moduli of these materials cover a range of values, the tensile strengths are all surprisingly similar. The coefficient of variation of tensile strengths ranged from 10% to 20%. All fibers, except PE, exhibited proportional tensile behavior to break. Therefore, a reasonable estimate of strain at break for these fibers is simply the ratio of tensile strength to tensile modulus.

A 2 cm length of PE fiber was tensile-tested to a load below break. This fiber exhibited tensile yield behavior. After testing, the intact fiber was embedded in resin and sectioned to determine the shape and area of the cross-section. The profiles of two transverse sections of this fiber sample taken approximately 1 cm apart are illustrated in Figure 4.6a. The cross-sectional area was determined to be $1.1 \times 10^3 \mu\text{m}^2$. Assuming the fiber "diameter" supplied by the manufacturer was calculated using linear density measurements, this hypothetical diameter corresponds to a cross-sectional area of $1.13 \times 10^3 \mu\text{m}^2$. Therefore, the areas calculated from micrographs of transverse fiber sections are in excellent agreement with manufacturer's data.

Using a machine compliance value obtained from tensile tests of other fibers under the same test conditions, a tensile modulus of 110 GPa was calculated for the single PE sample tested here. Within experimental error, this value is identical to the tensile modulus of 117 GPa quoted by the manufacturer. The limit of proportionality (onset of yielding) occurred at a tensile stress of 170 MPa.

Filament 1

Filament 2

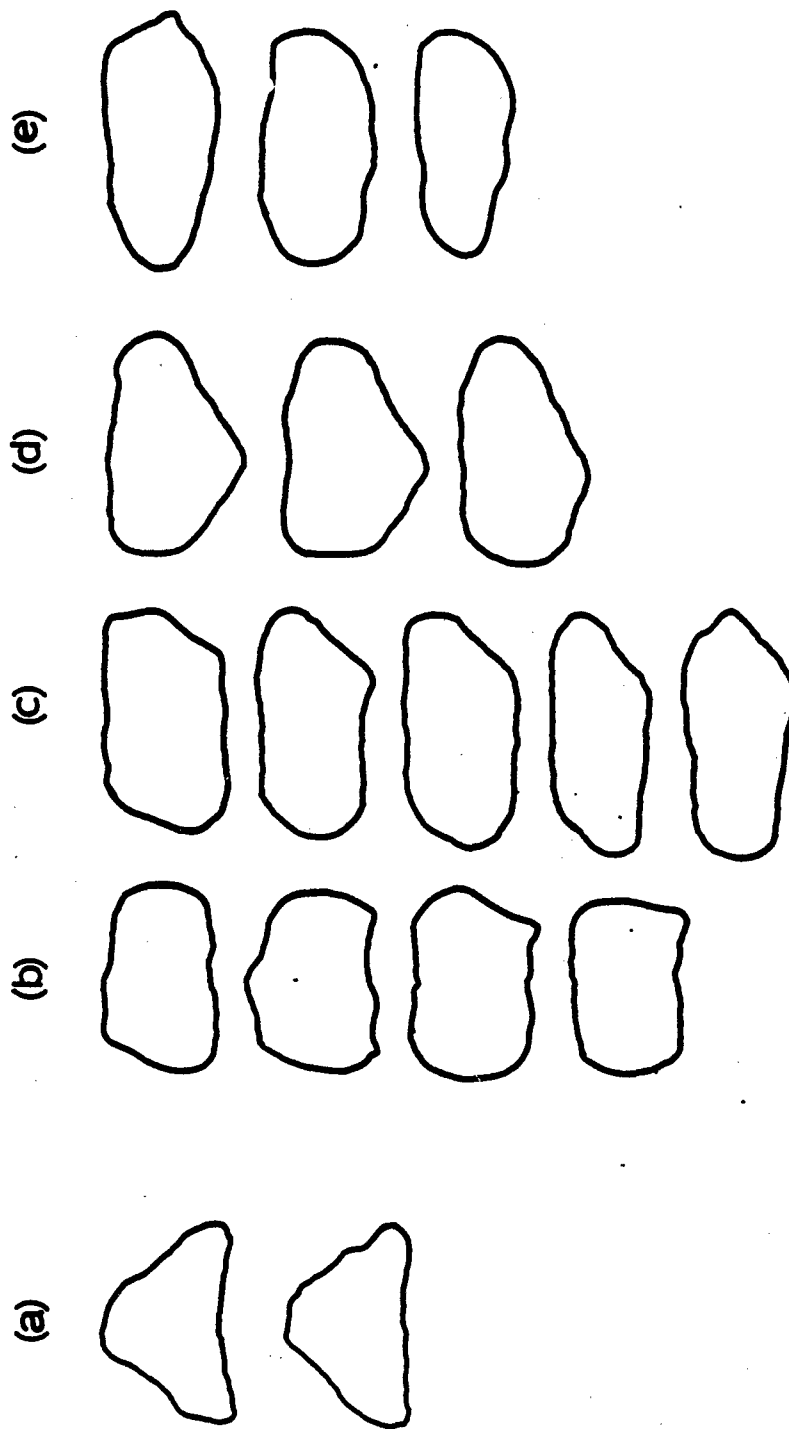


Figure 4.6. Tracings of optical micrographs of transverse sections of PE fibers.
(a) Filament 1: tensile test sample. (b-e) Filament 2: torsion test samples.

Values of torsion moduli G , critical compressive strains ϵ_c and calculated axial compressive strengths for each fiber are given in Table 4.2. Axial compressive strengths of PPTA (Kevlar 49) [17] and PBT [75] fibers were also obtained from calculations of the stress in each fiber at the reported yield or failure point measured for axial (0°) compression-testing of unidirectional composites of these fibers. These values are also listed in Table 4.2.

The graphite fiber is opaque and therefore could not be measured for compressive strength using transmission optical microscopy with the beam bending technique. However, the compressive strengths of similar pitch-based graphite fibers were calculated by other workers who used the elastica test to measure the compressive stress that initiated inelastic behavior [71] and an axial compression test to measure critical compressive strains [41]. The compressive strengths calculated in both studies corresponded to the axial compressive stress in the fiber at the onset of localized buckling that appeared on the fiber surface as a deformation band oriented at 90° to the fiber axis. The range of compressive strengths obtained for graphite fiber in these studies is given in Table 4.2.

It was discovered that axial tensile stresses resulted in an apparent increase in the torsion modulus that is given by the equation:

$$G^* = \alpha\sigma + G \quad (4.5)$$

where σ is the axial tensile stress, G^* is the apparent torsion modulus, G is the true torsion modulus and α is a constant approximately equal to 0.75. The reasons for and implications of this effect are examined and

Table 4.2
Torsion Moduli and Compressive Strengths of Fibers

Fiber	Torsion Modulus (GPa) ^a	Critical Compressive Strains (%) ^b	Calculated Compressive Strengths (GPa)	Composite Compressive Strength (GPa) ^c
PPTA	1.5 +0.20	0.50 +0.028	0.62 +0.063	0.45 ^e
PBT	1.2 +0.14	0.10 +0.022	0.27 +0.075	0.31 ^f
ABPBO	0.62 +0.07	0.18 +0.032	0.21 +0.055	
NTP	0.45 +0.04	0.15 +0.008	0.12 +0.011	
PE	0.7 +0.22	0.08 +0.017	0.09 +0.019	
Graphite	5.6	-	1.3-2.0 ^d	

^aCorrected for pendulum weight, except graphite.

^bCorrected for tensile prestrain applied during mounting to beams.

^cCalculated from σ_c/V_f , where σ_c = fiber composite 0° compressive strength, V_f = fiber volume fraction of composite.

^dFrom references [41,71].

^eFrom reference [17].

^fFrom reference [75].

+ values are standard deviations.

discussed in Chapter 5. For the present study it is only necessary to consider the increase in measured torsion modulus due to the weight of the disc pendulum. Therefore, the values of the true torsion modulus for each fiber are given in Table 4.2. For the thinner fibers, this correction for pendulum weight amounted to as much as 10%.

Only one successful test for the torsion modulus of the extremely brittle graphite fiber was performed. In addition, the effects of tension on the torsion modulus of this fiber could not be measured due to fiber breakage during handling. For these reasons, the torsion modulus of 5.6 GPa listed in Table 4.2 for the graphite fiber is an uncorrected (for pendulum weight) value obtained from a single test. It is encouraging that this value is reasonably close to the value of 4.1 GPa reported for the inter-basal plane shear modulus of a dislocation-free graphite crystal [76]. The similarity of these shear moduli is evidence for a radial structure in P-75 graphite fibers.

The largest uncertainty in torsion modulus is for PE fibers, due to their irregular and varying cross-sections. The profiles of cross-sections of 4 test specimens (all 2 cm long) are shown in Figure 4.6b-e. The torsional rigidities of these specimens were calculated assuming that the cross-sectional profiles could be approximated by an ellipse, rectangle or triangle, whichever most closely fit the particular cross-section. It should be noted that all 4 specimens were cut from a single filament approximately 12 cm long and examination of Figure 4.6b-e clearly shows the variation of the PE fiber cross-section along the length of this single filament.

Although the coefficient of variation of the PE fiber torsion modulus is large, the mean value of 0.7 GPa is in good agreement with the torsion modulus of 0.6 GPa measured for hot-drawn PE monofilaments [77]. The PE torsion modulus reported in Table 4.2 has not been corrected for the weight of the disc pendulum because the constant a in (4.5) that defines the relationship between apparent torsion modulus and axial stress could not be determined with sufficient accuracy due to the irregular fiber cross-section. There was a measurable linear increase in torsional rigidity of PE fiber with applied axial tensile stress, but the weight of even the large disc pendulum should result in only minimal fiber tensile stress and therefore a negligible apparent increase in the measured torsion modulus of the relatively thick PE fibers.

The calculated average cross-sectional area of the sections depicted in Figure 4.6b-e is $1.4 \times 10^3 \mu\text{m}^2$. The coefficient of variation of this value is 10%, which is equivalent to the variation in area along the lengths of the other fibers. However, this cross-sectional area is approximately 25% greater than the value calculated from manufacturer's data. This discrepancy is presumably due to a relatively large inter-filament variation in cross-sectional area.

The relatively large uncertainties in compressive strengths that were calculated from the product of tensile modulus and critical compressive strains arise from the combined errors in these latter two quantities. However, the range of coefficient of variation for compressive strengths is similar to the range of uncertainty for tensile

strengths. It is clear from Table 4.2 that the average compressive strength varies widely among the fibers.

The 0.50% critical compressive strain measured for PPTA using the cantilever beam technique is slightly lower than the 0.53% strain measured using the three-point beam technique described in Chapter 2. This discrepancy can be attributed to the fact that critical compressive strains are measured in situ (i.e., while under compression) using the cantilever beam bending technique, whereas with the three-point bending technique the fiber is viewed after compression. For this reason, the PPTA axial compressive strength of 0.62 GPa calculated from cantilever beam measurements is a better estimate of the true strength of the fiber. However, this value is still larger than that of 0.45 GPa calculated using composite data [17].

In Chapter 2 it was shown that PPTA (Kevlar 49) fibers form helical kink bands under axial compression. SEM and optical micrographs of kink bands in PBT, ABPBO, NTP and PE fibers are shown in Figures 4.7-4.10. Except for the PE fiber, no kink bands were observed in fibers prior to compression via beam bending or matrix shrinkage. Few kink bands were observed in as-received PE fibers, which, in light of the relative thickness of the fiber and its low critical strain to kink band formation, probably resulted from fiber bending due to handling.

Kink bands initiate in PBT fibers as thin bands oriented at approximately 70° to the fiber axis. The arrow in Figure 4.7c points to an incipient band. At higher levels of compressive strain, the bands propagate across the fiber diameter and eventually form the thick,

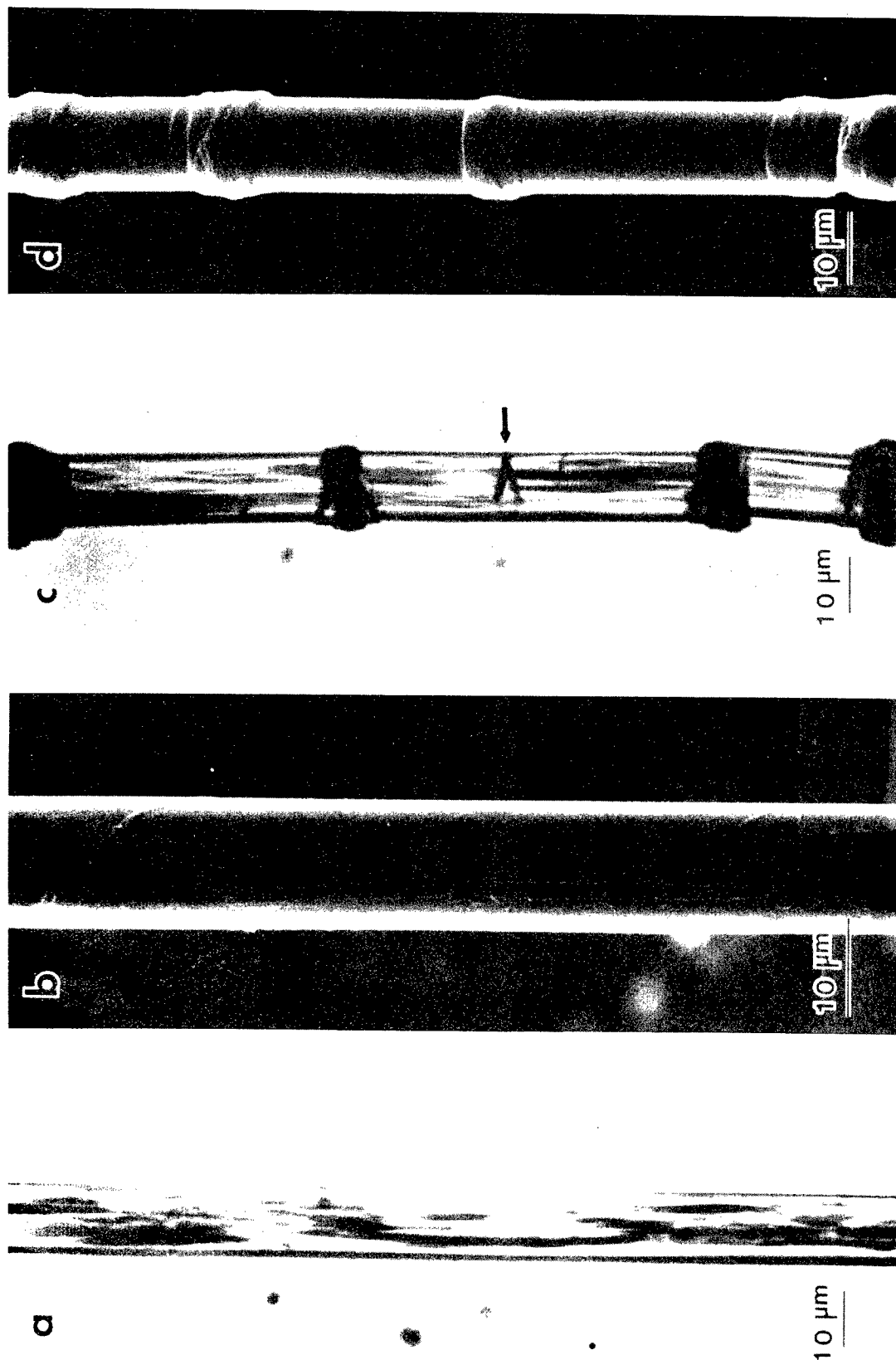


Figure 4.7

PBT fiber. Before compression: (a) optical micrograph; (b) SEM micrograph. After axial compression: (c) optical micrograph; (d) SEM micrograph.

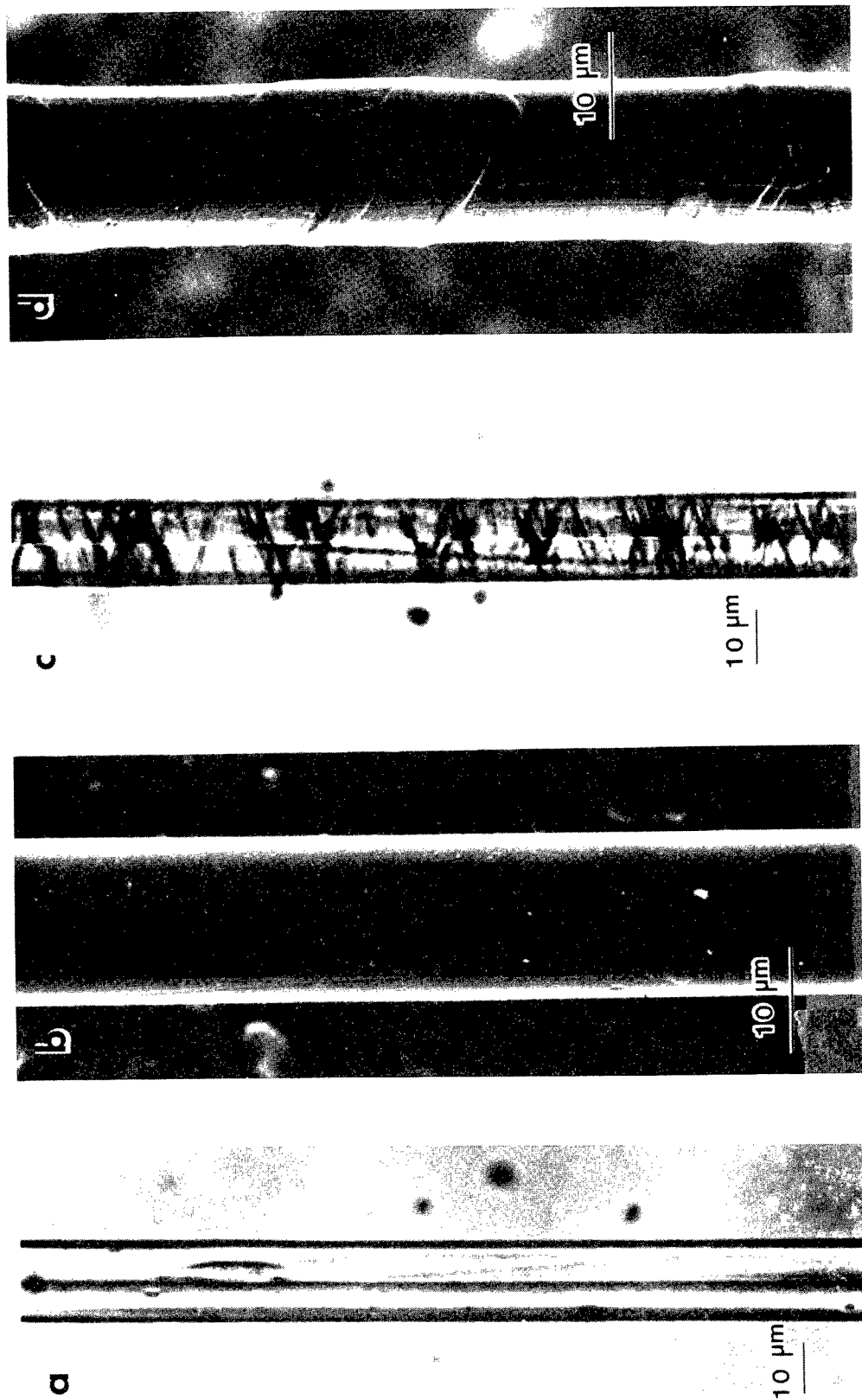


Figure 4.8

ABPB0 fiber. Before compression: (a) optical micrograph; (b) SEM micrograph. After axial compression: (c) optical micrograph; (d) SEM micrograph.

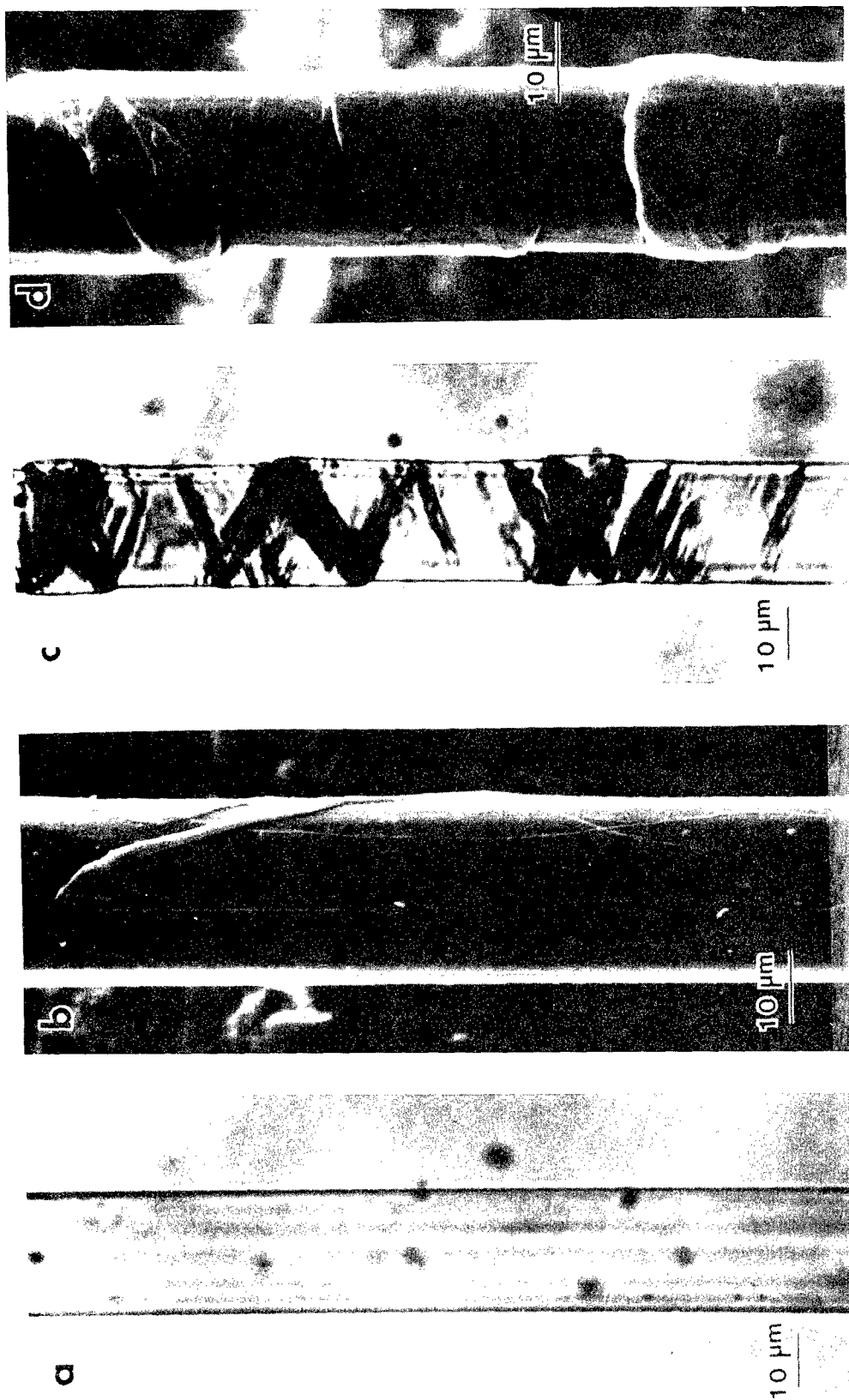


Figure 4.9
NTP fiber. Before compression: (a) optical micrograph; (b) SEM micrograph. After axial compression: (c) optical micrograph; (d) SEM micrograph.

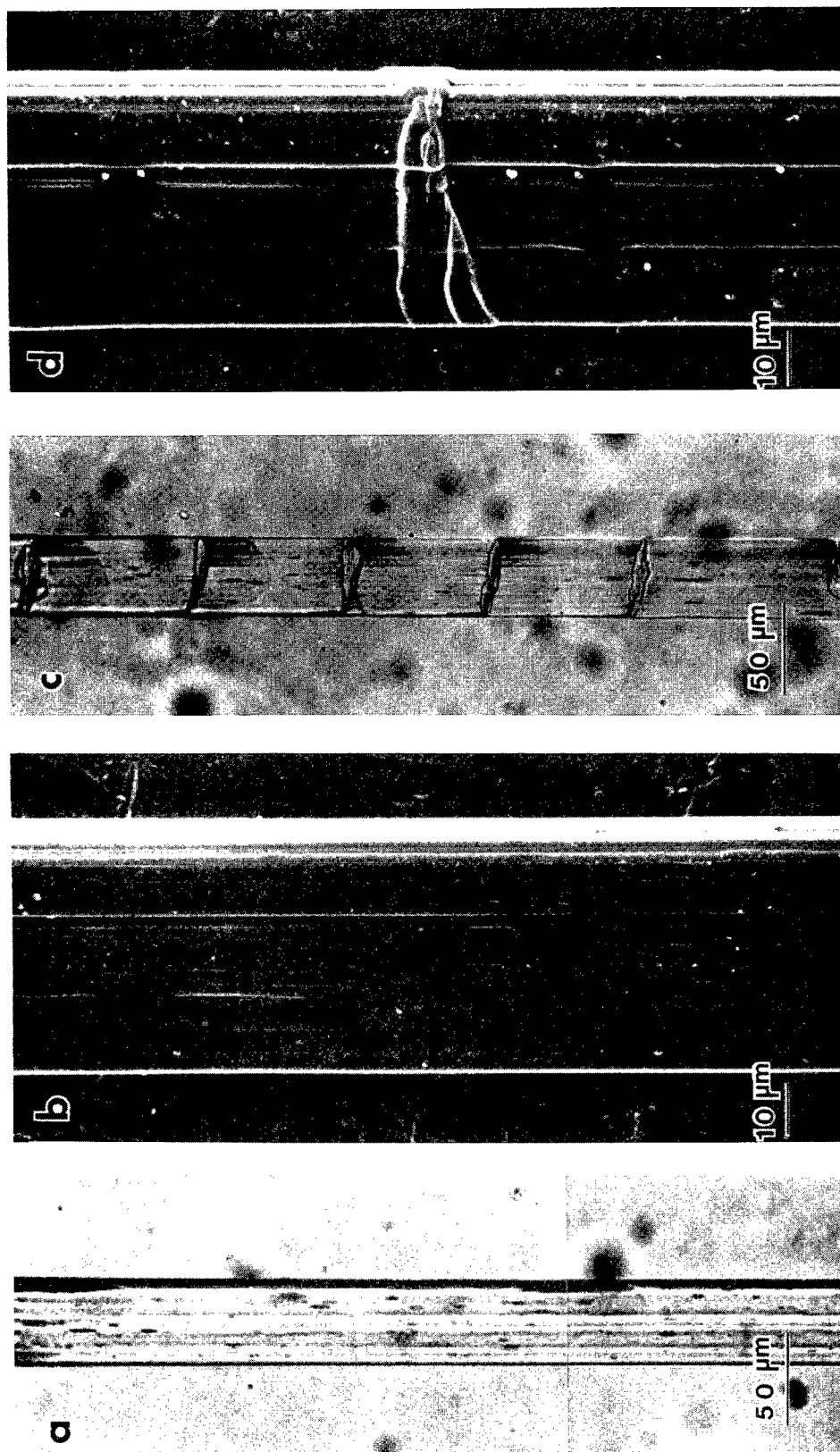


Figure 4.10

PE fiber. Before compression: (a) optical micrograph; (b) SEM micrograph. After compression: (c) optical micrograph; (d) SEM micrograph.

bulging perpendicular deformation bands seen in Figures 4.7c,d. These large bands form periodically along the fiber length.

The kink bands in compressed ABPBO fibers shown in Figure 8c,d bear some resemblance to the helical kink bands observed in PPTA fibers (see Figures 2.4 and 2.5). Like the PPTA kink bands, the kink bands in ABPBO are oriented at angles ranging from 50° - 60° to the fiber axis. Although the ABPBO compressive kink bands appear to be helical, there is no propagation of any one helical kink band for any appreciable distance along the fiber length.

In optical micrographs of compressed NTP fibers (Figure 4.9c), black deformation bands of various thicknesses are observed to be oriented at approximately 55° to the fiber axis. Where only one band crosses the fiber diameter, the deformation closely resembles that of an ideal kink band (Figure 3.1). Where two such bands criss-cross the fiber diameter, the fiber exhibits bulging that is similar to the dilatation in deformation bands in PBT fibers. The surface of compressed NTP fibers exhibits kink bands oriented at several angles to the fiber axis (Figure 4.9d). There is no obvious regularity to the spacing of these bands along the length of NTP fibers.

Compressed PE fibers exhibit both obliquely oriented kink bands and bands that are oriented at 90° to the fiber axis (Figures 4.10c,d). In many regions of compressed PE fibers, deformation bands formed at regular intervals along the fiber length.

A comparison of measured compressive strengths with predicted critical stresses for elastic instabilities (equations (4.1) and (4.2))

for all fibers is shown in Table 4.3. The shear mode buckling stress σ_{cr}^S is simply equal to a shear modulus, and it is assumed that the torsion modulus is equal to the longitudinal shear modulus of the "foundation" that supports the chains and/or microfibrils against buckling.

The calculation of the extension mode buckling stress σ_{cr}^e is made using values of transverse moduli E_t , bond bending and torsion force constants k , covalent bond lengths ℓ and cross-sectional areas of chains A . The values of E_t have been reported for Kevlar 49 [78] and oriented PE [77]. An estimate of 0.5 GPa for the transverse moduli of PBT, ABPBO and NTP fibers was made based on the similarity of these rigid rod polymers to PPTA. Covalent bond lengths were assumed to be 1\AA for every backbone bond in every chain. Bending force constants of valence angles are surprisingly similar for many types of bonds, with values near $0.5 \times 10^{-18} \text{ J-rad}^{-1}$ [67]. However, for PE it was assumed that bending of the chain will occur almost exclusively by torsion away from the trans conformation. A force constant for this torsion in n-paraffins was measured to be $0.024 \times 10^{-18} \text{ J-rad}^{-1}$ [79]. The cross-sectional areas of PPTA [25], PBT [80], and PE [81] chains were calculated from unit cell dimensions. An estimate of chain cross-sectional area equal to 20\AA^2 was made for ABPBO and NTP fibers after considering the values reported for the other fibers.

No cross-sectional area or bending rigidity $k\ell$ can be defined for the graphite ribbons based on the microbuckling model. Therefore, there is no calculation for the extension mode buckling strength of graphite fibers presented here. The value of shear mode buckling stress for

Table 4.3
Predicted and Measured Axial Compressive
Strengths of Fibers

Fiber	$A(\text{\AA}^2)$	$E_t(\text{GPa})$	$\sigma_{cr}^e(\text{GPa})$	$\sigma_{cr}^s(\text{GPa})$	$\sigma_c(\text{GPa})$
PPTA	20	0.77	3.9	1.5	0.62 [0.45]
PBT	22	(0.5)	2.9	1.2	0.27 [0.31]
ABPBO	(20)	(0.5)	(3)	0.62	0.21
NTP	(20)	(0.5)	(3)	0.45	0.12
PE	18	0.7	0.9	0.7	0.09
Graphite	-	-	-	4.1-5.6	1.3-2.0

$$\sigma_{cr}^e = 4\sqrt{E_t k\ell}/A$$

$$\sigma_{cr}^s = G$$

σ_c = measured compressive strength. Values in brackets calculated using composite data.

Values in parentheses are estimates.

graphite is assumed to fall between the basal plane shear modulus of 4.1 GPa for dislocation-free graphite single crystal [76] and the torsion modulus of 5.6 GPa measured for P-75 fiber.

Inspection of Table 4.3 reveals that the shear mode buckling stress is always lower than the extension mode buckling stress for every fiber; therefore, the former is a better estimate of the axial compressive strengths of these fibers. All shear mode predictions of compressive strength are larger than measured values, but the ratio of predicted to measured strengths is nearly identical for all fibers except PE.

The correlation between shear mode buckling stress estimates (i.e., torsion moduli) and measured compressive strengths is extremely good for all fibers except PE. A plot of measured strengths versus torsion moduli for all fibers, with the exception of PE, is shown in Figure 4.11. The points for PPTA, PBT, ABPBO and NTP fibers could be fitted to a straight line with a correlation coefficient $r=0.89$. If the compressive strengths of PPTA and PBT fibers calculated from composite data are used for linear correlation, the goodness of fit improves to a value $r=0.98$. The equation that describes this correlation is:

$$\sigma_c = 0.3G \quad (4.6)$$

It is also evident from Figure 4.11 that the relationship between shear modulus and axial compressive strengths of graphite fibers can be described by (4.6).

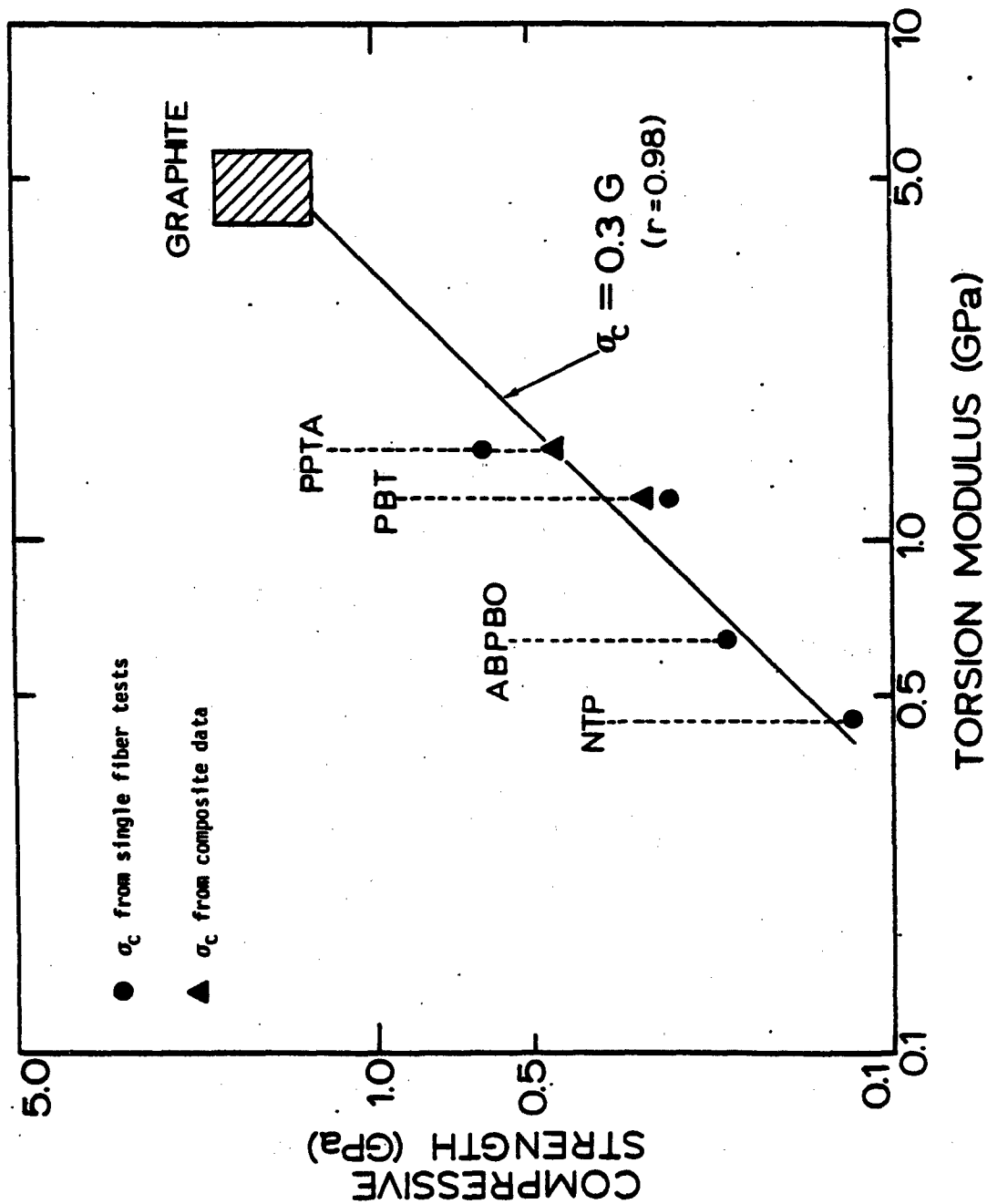


Figure 4.11

Correlation between measured axial compressive strengths and torsion moduli for high performance organic fibers.

The shear mode buckling estimate given by the torsion modulus of PE is much higher than the measured compressive strength. The ratio of measured to predicted strength is only 0.13 for this fiber.

4.4 Discussion

The correlation between axial compressive strengths and torsion moduli measured for the rigid-rod polymer and graphite fibers supports the concept of compressive failure due to elastic microbuckling instabilities for these materials.

In Chapter 2 it was shown that deformation due to shear mode (co-operative) buckling closely resembles the deformation observed in the nucleation region of a kink band [56,57,65]. Therefore, it is both reasonable and satisfying to find the shear mode buckling stress the most appropriate estimate of axial compressive strength. The compressive stress required to initiate shear mode buckling instability in unidirectional glass fiber-reinforced composites is also the best estimate of compressive strength for these materials [42,69,70].

A linear correlation analysis of compressive strength-torsion modulus data revealed a remarkably good fit for all fibers except PE. Indeed, considering the simplicity of the instability analysis, which does not account for fiber morphology, individual molecular chain architecture, structural defects and inhomogeneities, it is encouraging that predictions are within an order of magnitude of measured compressive strengths. Theoretical predictions of material strengths are typically two orders of magnitude larger than measured values [82].

The shear mode buckling stress was assumed to be equal to the longitudinal shear modulus measured from fiber torsion. For the rigid-rod polymer and graphite fibers this estimate was too large by approximately a factor of 3. Possible explanations for this disparity are considered below.

The single link-hinge chain model was constructed after assuming many simplifications in the specific architecture of the chain. Particular values of bending force constants, bond lengths and bond orientations were ignored. Fortunately, the analysis of a collection of interacting chains showed that the shear mode buckling stress is almost exclusively a function of the shear modulus of the foundation and that the resistance to buckling due to the bending rigidity of the chains can be neglected when the chains are long. As mentioned in Chapter 3, if another level of structural scale was considered--for instance, long microfibrils--the buckling stress for a collection of these fibrils would also be proportional to a shear modulus. In this particular case, if the fibrils were assumed to be rigid, then the shear mode buckling stress would be proportional to the shear modulus of the material between fibrils.

The lateral bonding between chains or microfibrils was modelled with a continuous foundation that has a shear modulus equal to the torsion modulus of a fiber. If there is anisotropy within the fiber cross-section, then there may be two longitudinal shear moduli. For such fibers, buckling will occur via shear deformation between planes of the

lowest longitudinal shear modulus. Therefore, the estimate of axial compressive strength is the minimum longitudinal shear modulus of a fiber.

Kevlar and radial graphite fibers are cylindrically orthotropic materials and hence exhibit two longitudinal shear moduli: G_{rz} and $G_{\theta z}$. Torsion tests of fibers measure $G_{\theta z}$, which is the modulus of shearing between hydrogen-bonded sheets in Kevlar fibers and between basal planes in radial graphite fibers and is therefore the lower longitudinal shear modulus for these fibers. The torsion modulus of "onionskin" graphite fibers is due to shear deformations within basal planes and is larger than G_{rz} . It is therefore not surprising that reported torsion moduli of some graphite fibers [83,84] are greater than the value of 4.1 GPa determined for shear between dislocation-free graphite basal planes [76]. It must be emphasized that for fibers which exhibit anisotropy such that $G_{\theta z} > G_{rz}$, the torsion modulus is the wrong estimate for the shear mode buckling stress of these materials.

It was shown in Chapter 3 that kink bands are formed under axial compression by nucleation in one local region followed by propagation at nearly constant compressive stress. Examination of the nucleation process by other workers revealed that S-shaped incipient buckling of planes of easy shear slip occurred prior to material collapse into an angular kink band [56,57,65]. The theoretical compressive strength was defined in Chapter 3 as the critical compressive stress required to initiate elastic instabilities that are believed to be the cause of this local buckling. Therefore, structural inhomogeneity may lead to

initiation of local instabilities at compressive loads less than the value predicted for shear mode buckling of a homogeneous material.

The presence of voids in fibers can be crudely incorporated into the instability analysis by eliminating the elastic foundation from one side of the chains or microfibrils that line the void surface. Additionally, the material at the fiber surface is supported on only one side. These chains and microfibrils should reach critical buckling loads at a compressive stress equal to half the minimum longitudinal shear modulus.

Residual stresses have been shown to exist in graphite [85] and PBT fibers [19]. Indeed, the stresses generated during drying of PBT fibers are believed to be the cause of compressive buckling observed in the dried fibers [19]. Regions of a fiber that are under residual compression will reach critical buckling stresses first. Therefore, premature nucleation of kink bands can occur in such regions.

Although it is reasonable to assume that residual stresses exist in all the fibers examined in this study, it is believed that these stresses have minimal effect on the reduction in axial compressive strength. Significant residual stress would be revealed by the linear correlation analysis of compressive strength versus torsion modulus as a relatively large intercept. The data plotted in Figure 4.8 were fitted to a straight line which passed close to the origin, and therefore indicate only a small effect of residual stress on compressive strength. The only other way that large residual stresses could exist and affect

the compressive strengths of fibers that obeyed the relationship $\sigma_c = 0.3G$ would be if the magnitude of residual stress in each fiber was directly proportional to the torsion modulus. This proportionality is highly unlikely for five different fibers. However, the presence of even small residual axial compressive stresses near the surface of these fibers could explain the initiation of kink bands at the fiber surface.

Small misalignment or curvature of chains and microfibrils should not affect the compressive stress that initiates elastic instabilities. However, under axial compression, these misaligned regions would be subjected to shear stresses that could possibly exceed the shear strength between chains or microfibrils. Argon has proposed that axial compressive strengths of composites are limited by local shear failure along such planes of misalignment [62]. He believes that shear failure initiates material collapse into kink band formation. The equation derived by Argon to predict fiber-reinforced composite compressive strength for failure by this mechanism is:

$$\sigma_c = \frac{\tau_m}{\phi} \quad (4.7)$$

where τ_m is the interlaminar shear strength and ϕ is the angle of misalignment measured with respect to the load axis.

Any high performance fiber will exhibit a distribution of molecular orientation, and shear failure should occur in the most poorly aligned regions. Although it is difficult to measure the largest misalignment angle for any fiber it is reasonable to assume, based on Argon's proposal of shear failure initiation of kink banding, that

fibers with higher average orientation should have higher compressive strengths. However, the compressive strength of PBT [19,75] and Kevlar [17] fibers is relatively insensitive to improvements in average axial orientation by tension heat-treatment. Therefore, it is unlikely that shear failure initiates compressive kink band formation in high performance fibers.

The gel-spun PE fiber does not obey the relationship between compressive strength and torsion modulus obtained for the rigid rod polymer fibers. The analysis of elastic instabilities in high performance fibers was made for fully extended linear polymers. Inasmuch as chain entanglements are necessary for the attainment of high degrees of PE chain extension using the gel-spinning process, the existence of such entanglements in PE fibers may severely limit their compressive strength.

As mentioned above for the rigid rod polymers, it is necessary to measure the minimum longitudinal shear modulus to predict compressive strength. If the PE fibers are anisotropic within their cross-section or if they contain amorphous regions that exhibit low shear moduli, then it is conceivable that the torsion modulus is not the best estimate of compressive strength.

Although it might be argued that a compressive buckling analysis should not apply to flexible polymer chains, it is emphasized that the analysis showed that the critical compressive stress for shear mode buckling is only a function of intermolecular (or interfibrillar) interactions when the chains (or fibrils) are long. Therefore, the buckling

stress for a collection of laterally interacting and infinitely flexible extended chains is also equal to the minimum longitudinal shear modulus of such a collection.

4.5 Conclusions

The axial compressive strength of high performance rigid-rod polymer fibers and certain graphite fibers is limited by the onset of elastic microbuckling instabilities and not by material failure. The best estimate of compressive strength is given by:

$$\sigma_c = G_{\min}$$

where G_{\min} is the minimum longitudinal shear modulus of a fiber.

A linear correlation analysis of measured compression strengths and torsion moduli for five different fibers yielded an excellent fit of data to a straight line given by $\sigma_c = 0.3G$. Several reasons for this theoretical overestimate of compressive strength were discussed in relation to anisotropy and local irregularities that might act as nucleation regions for kink band formation.

The stages of axial compressive failure due to kink band formation can be summarized as follows:

1. At a critical axial compressive stress equal to the minimum longitudinal shear modulus, there is initiation of local elastic instability.
2. Large elastic buckling deformations occur at this critical stress, which subsequently result in shear failure between the planes of easy shear slip (i.e., between chains or microfibrils).

3. Shear failure eliminates the elastic foundation from one side of neighboring chains or fibrils, causing them to undergo similar buckling instability at the same critical compressive stress. As a result the instability propagates through the fiber.
4. Buckled material collapses to the observed angular kink band due to severe bending at the kink band boundaries.

The apparent contradiction in this proposed failure mechanism is that the predicted compressive strength is obtained from elastic instability analysis, which is not a failure analysis. Thus the compressive strength is equal to a longitudinal shear modulus and not a shear strength. In the perfectly oriented fiber there is no shear deformation due to axial compression until the critical stress for elastic instability is reached. The large deformations that result from the instability subsequently lead to true material failure in shear.

CHAPTER V

COUPLING OF AXIAL NORMAL STRAINS WITH LONGITUDINAL SHEAR STRAINS IN HIGH PERFORMANCE POLYMER FIBERS

5.1 Background

5.1.1 Finite Strain Tensor for Simple Shear in Two Dimensions

In this chapter, the coupling of axial normal strains ϵ_{zz} with torsion shear strains $\gamma_{z\theta}$ in anisotropic high performance polymer fibers is investigated. Torsion of cylindrical fibers sets up a linear distribution of simple shear strains $\gamma_{z\theta}$ that range from zero at the fiber axis to a maximum on the fiber surface. Simple shear deformation in the $z\theta$ plane is illustrated in Figure 5.1 as the distortion of an initially rectangular material element $abcd$ into the parallelogram described by points $abc'd'$. The displacement field for this shear deformation is given by:

$$\begin{aligned} u_{\theta} &= kz \\ u_z &= 0 \end{aligned} \tag{5.1}$$

where u_i are the displacements along each of the cylindrical coordinate axes.

The Lagrangian finite strain tensor is defined as:

$$\epsilon_{ij} = \frac{1}{2} \left[\frac{\partial u_j}{\partial a_i} + \frac{\partial u_i}{\partial a_j} + \frac{\partial u_m}{\partial a_i} \frac{\partial u_m}{\partial a_j} \right] \tag{5.2}$$

where $i, j = \theta, z$.

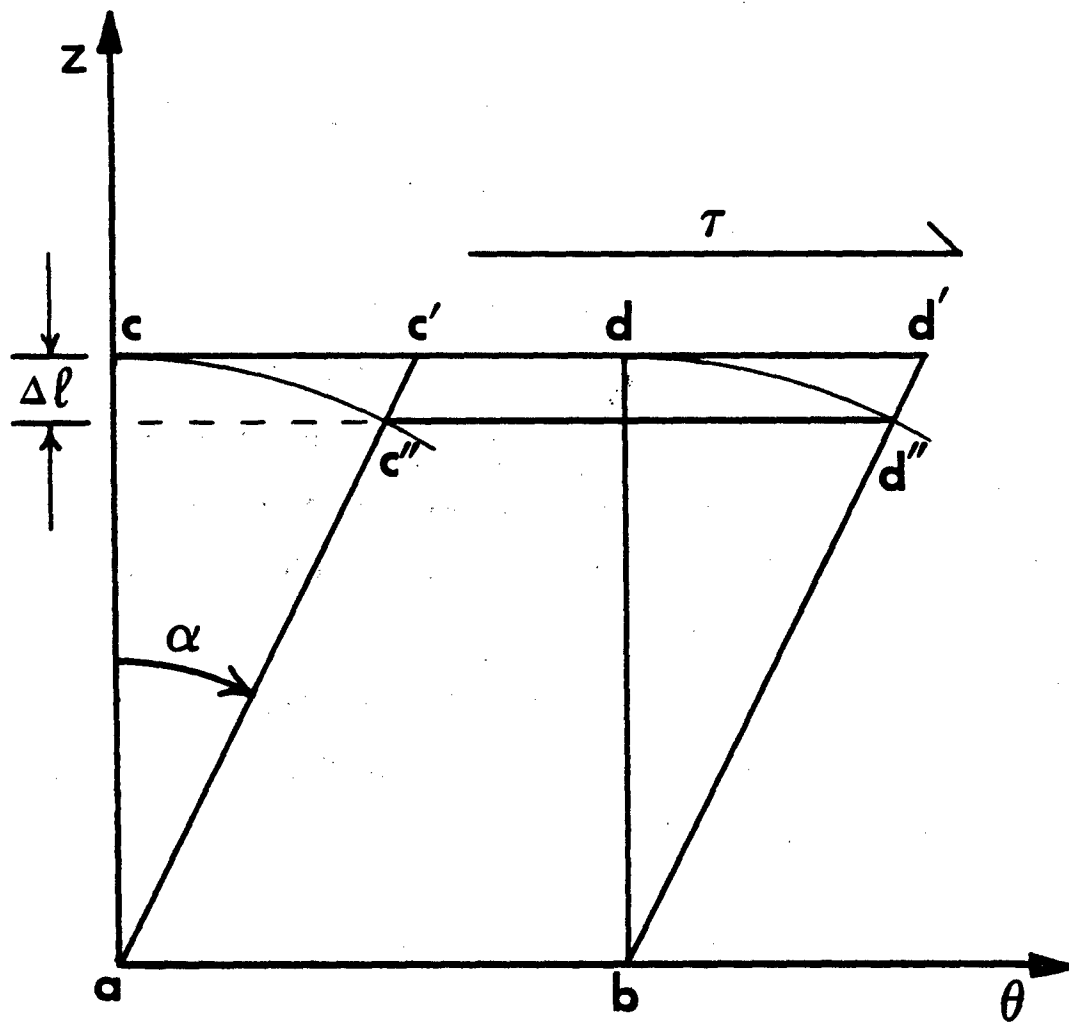


Figure 5.1. Simple shear deformation with and without volume loss.

The engineering shear strain $\gamma_{z\theta}$ is defined with respect to this strain tensor as:

$$\gamma_{z\theta} = 2\epsilon_{z\theta} \quad (5.3)$$

which, after substitution of the displacements (5.1) into (5.2), yields:

$$\gamma_{z\theta} = \frac{\partial u_{\theta}}{\partial z} = k \quad (5.4)$$

It is verified from inspection of Figure 5.1 that $k = \tan \alpha$, which for small displacements can be approximated by $k \approx \alpha$. Therefore, the shear strain due to small displacements (5.1) becomes:

$$\gamma_{z\theta} \approx \alpha \quad (5.5)$$

Substitution of displacements (5.1) into (5.2) also reveals that this deformation results in a normal tensile strain along the z-direction of magnitude:

$$\epsilon_{zz} = \frac{1}{2} k^2 \quad (5.6)$$

which for small α can be approximated by:

$$\epsilon_{zz} \approx \frac{1}{2} \alpha^2 \quad (5.7)$$

This axial strain represents the elongation of line ac to a length ac', which maintains constant height of the element during simple shear. It is verified from the areas of rectangle abcd and parallelogram abc'd' shown in Figure 5.1 that this axial elongation is necessary to keep volume constant during simple shear deformation.

The axial strain ϵ_{zz} is a second-order effect that is neglected when the shear strain (and therefore α) is small. For isotropic materials this approximation is reasonable because only a relatively small

axial stress (i.e., relative to shear stress $\tau_{z\theta}$) is required to produce this elongation.

However, if a material is anisotropic and possesses a relatively high axial modulus E_{zz} and low longitudinal shear modulus $G_{z\theta}$, the axial stress $\sigma_{zz} = E_{zz} \epsilon_{zz}$ required to maintain constant volume during simple shear deformation may be comparable to the shear stress $\tau_{z\theta}$. Therefore, when such materials are deformed in simple shear in the absence of axial stress σ_{zz} there should be axial contraction. In other words, there should be a reduction in the height of the material element.

In the extreme case of no elongation of the element ac during shear, the deformed material element will appear as the parallelogram $abc'd$ shown in Figure 5.1. This parallelogram is formed by simple rotation of parallel lines ac and bd through an angle α as shown; thus the lengths ac and bd are equal to ac' and bd' . However, this distortion of the rectangular element results in a volume loss, which is revealed as the reduction in area of rectangle $abcd$ after it is deformed into parallelogram $abc'd$. Therefore, there are two competing effects involved in simple shear deformation. The reduction in height of the material element in the absence of axial stress σ_{zz} during simple shear is resisted by the negative volume change that must accompany this reduction in height.

If the volume changes are not neglected, the reduction in height of the element $abcd$ after shearing is:

$$\Delta l_{\max} = -[ac - ac(\cos\alpha)] \quad (5.8)$$

which, for small angles α , can be approximated by:

$$\Delta \ell_{\max} \approx -ac\left(\frac{\alpha^2}{2}\right) \quad (5.9)$$

This is the maximum reduction in height of the rectangular element because it is assumed that elements ac and bd rotate without elongation during shear deformation.

If the material does indeed resist volume changes, it is reasonable to expect that the reduction in height of element $abcd$ with shear will be less than that given by (5.9). This effect may be accounted for by defining a constant α that can take on values $0 \leq \alpha \leq 1$ and represents the fraction of the maximum height reduction that occurs during shear. Therefore, the reduction may be given by:

$$\Delta \ell = (\alpha) \Delta \ell_{\max} \approx -(\alpha)ac\left(\frac{\alpha^2}{2}\right) \quad (5.10)$$

which, for small strains, is approximately:

$$\Delta \ell \approx -(\alpha)ac\left(\frac{\gamma_{z\theta}^2}{2}\right) \quad (5.11)$$

The value α is independent of α , and is unity when no elongation of elements ac and bd occurs during shear (i.e., when there is no resistance to volume changes) and is zero when there is no height reduction (i.e., when there is no volume change) during shear. Shear deformations that yield a value of $0 \leq \alpha \leq 1$ involve both volume reduction and axial strain ϵ_{zz} .

5.1.2 Torsion of a Solid Cylindrical Rod

Torsion of a solid circular cylinder about its axis imposes simple shear strain $\gamma_{z\theta}$ defined by:

$$\gamma_{z\theta} = \frac{\psi r}{\ell} \quad (5.12)$$

where ψ is the angle of twist, r is the radial distance from the cylinder axis and ℓ is the length of the cylinder. Therefore, there is a linear distribution of shear strain ranging from $\gamma=0$ at the cylinder axis to a maximum $\gamma_m = \psi R/\ell$ at the surface of a cylinder of radius R . (For the remainder of this chapter the symbol γ will refer to $z\theta$ shear strain unless otherwise noted.)

In the previous section, second-order effects that give rise to axial contraction during simple shear in two dimensions were discussed. The consequences of this axial contraction on torsion of a solid cylinder may be predicted by considering the cylinder to be composed of many thin concentric hollow cylinders of radii r . Torsion of these concentric cylinders through an angle ψ results in shear strains which vary among the cylinders as given by (5.12).

If each hypothetical concentric cylinder were not "bonded" to its neighbors, each would shorten, with torsion, by an amount given by (5.11). Therefore, there would be a parabolic distribution of length reduction for the solid cylinder, which may be calculated from:

$$\Delta \ell(r) = - \frac{a \ell_0}{2} \left(\frac{\psi r}{\ell_0} \right)^2 \quad (5.13)$$

where ℓ_0 is the initial length of the solid cylinder and therefore of every concentric cylinder before twisting. However, if transverse planes ($r\theta$ planes) are to remain plane and parallel during torsion, then the change in length of each concentric cylinder is forced to be

identical. This restriction is especially true for long cylinders and it requires that axial normal stresses develop in a twisted solid cylinder to maintain each hypothetical concentric cylinder at the same length.

If there is no external axial load acting on the cylinder during twisting, then the net axial stress must be zero on transverse planes. Using this boundary condition, Timoshenko determined the equation for the axial normal stress distribution in a twisted isotropic solid cylinder [86]. With the assumption that shear strain γ results in maximum axial length reduction (i.e., neglecting resistance to volume change so that $\alpha=1$ in (5.13)), he obtained, in the present notation, the equation:

$$\sigma_{zz}(r) = \frac{E\psi^2}{2\ell_0^2} \left(r^2 - \frac{R^2}{2} \right) \quad (5.14)$$

where E is Young's Modulus.

Examination of (5.14) shows that there are tensile stresses in the outer region of the cylinder where $r > R/\sqrt{2}$ and compressive stresses in the central region of the cylinder where $r < R/\sqrt{2}$. This stress distribution is a consequence of the larger amount of axial contraction that the outer cylinder region would undergo with shear deformation but is prevented from doing by the inner region.

Timoshenko also calculated the axial contraction with twist of a solid cylinder to be:

$$\Delta\ell = \frac{-\psi^2 R^2}{4\ell_0} \quad (5.15)$$

Comparison of (5.15) with (5.13), assuming $\alpha=1$, reveals that the

predicted axial contraction of a solid cylinder due to torsion is half that of a thin-walled hollow cylinder of the same radius R .

The analysis by Timoshenko may be improved upon by accounting for the resistance to volume change during simple shear deformation, which was discussed in the previous section. Assuming each hypothetical cylinder shortens by an amount given by (5.13), equations (5.14) and (5.15) that describe the axial normal stress distribution and axial contraction respectively due to torsion will be modified by simply multiplying each by the constant α .

Timoshenko considered the effect of torsion on length changes of isotropic cylinders and therefore predicted such materials should shorten with twist. Experimentally it has been shown that solid circular cylinders of metal [87,88] and rubber [89] actually elongate with twist. This phenomenon can be explained by rigorous nonlinear elasticity theory [90]. One reason for the failure of Timoshenko's two-dimensional analysis to predict the elongation of isotropic cylinders with twisting is that it does not consider volume changes.

In comparison, twisting anisotropic cylinders that have a relatively high axial modulus and low longitudinal shear modulus, such as textile fibers, results in axial contraction [91]. The application of nonlinear elasticity theory to such anisotropic materials requires determination of several material constants that are very difficult to measure [90]. Therefore, it is often impossible to predict not only the magnitude but also the direction (elongation or contraction) of axial

length changes of a solid cylinder with twist using nonlinear elasticity analysis.

In light of the relatively large axial stresses required to prevent axial contraction due to twisting of materials exhibiting the particular anisotropy common to textile fibers, it is reasonable to consider Timoshenko's analysis, as modified here, to explain the observed axial contraction. The empirical constant α was introduced in the previous section to account for axial contraction that is less than the maximum predicted by a two-dimensional analysis. The contraction of a solid cylinder with twisting may also be characterized by a constant α that is a multiplicative factor for equations (5.14) and (5.15). This constant is not defined in terms of material constants (stiffness coefficients) and must be determined experimentally. If values of $\alpha < 1$ are obtained from torsion-axial contraction measurements, they may be explained in terms of the resistance of the material to volume changes due to length and radius changes during twist. Therefore, the constant α determined from twisting a solid cylinder might be different from the value obtained from twisting a hollow cylinder of the same material.

5.1.3 Prediction of Coupling of Axial Normal Stress with Longitudinal Shear Modulus

An interesting consequence of the axial contraction that occurs with torsion of certain anisotropic cylinders as discussed in the previous sections is the effect of a constant axial tensile stress on the shear stiffness of these materials. The two-dimensional analysis of

this effect was first published by Foye [92] and will be reproduced here with some alteration.

Consider a rectangular material element that is subjected to a constant axial stress σ_0 as shown in Figure 5.2a. If this element is now deformed in simple shear by a stress $\tau_{z\theta}$, it will contract axially. Because the stress σ_0 is held constant during shear, it does not elongate the element in the axial direction as the element is distorted. Therefore, the element contracts axially by an amount calculated from (5.11) irrespective of the value of σ_0 . It is only necessary to consider that the initial height (length a in (5.11)) of the element increases with increasing σ_0 .

Because the element contracts with shear, there is work done by the material in displacing the stress σ_0 through a distance Δl as shown in Figure 5.2b. If the material element depicted in Figure 5.2a is a square of unit dimensions, then the total work per volume of deforming this element is:

$$W = \frac{\tau\gamma}{2} - \sigma_0 a(1 - \cos\alpha) \quad (5.16)$$

where the first term on the right-hand side of (5.16) is the work done on the element by the applied shear stress and the second term is the work done by the element due to the axial contraction against the line of action of the constant stress σ_0 . (The subscripts $z\theta$ for shear stresses and strains and zz for axial normal stresses are to be understood.) The initial work to deform the material when the stress σ_0 is applied is neglected because the initial state is taken as the deformed element after application of σ_0 .

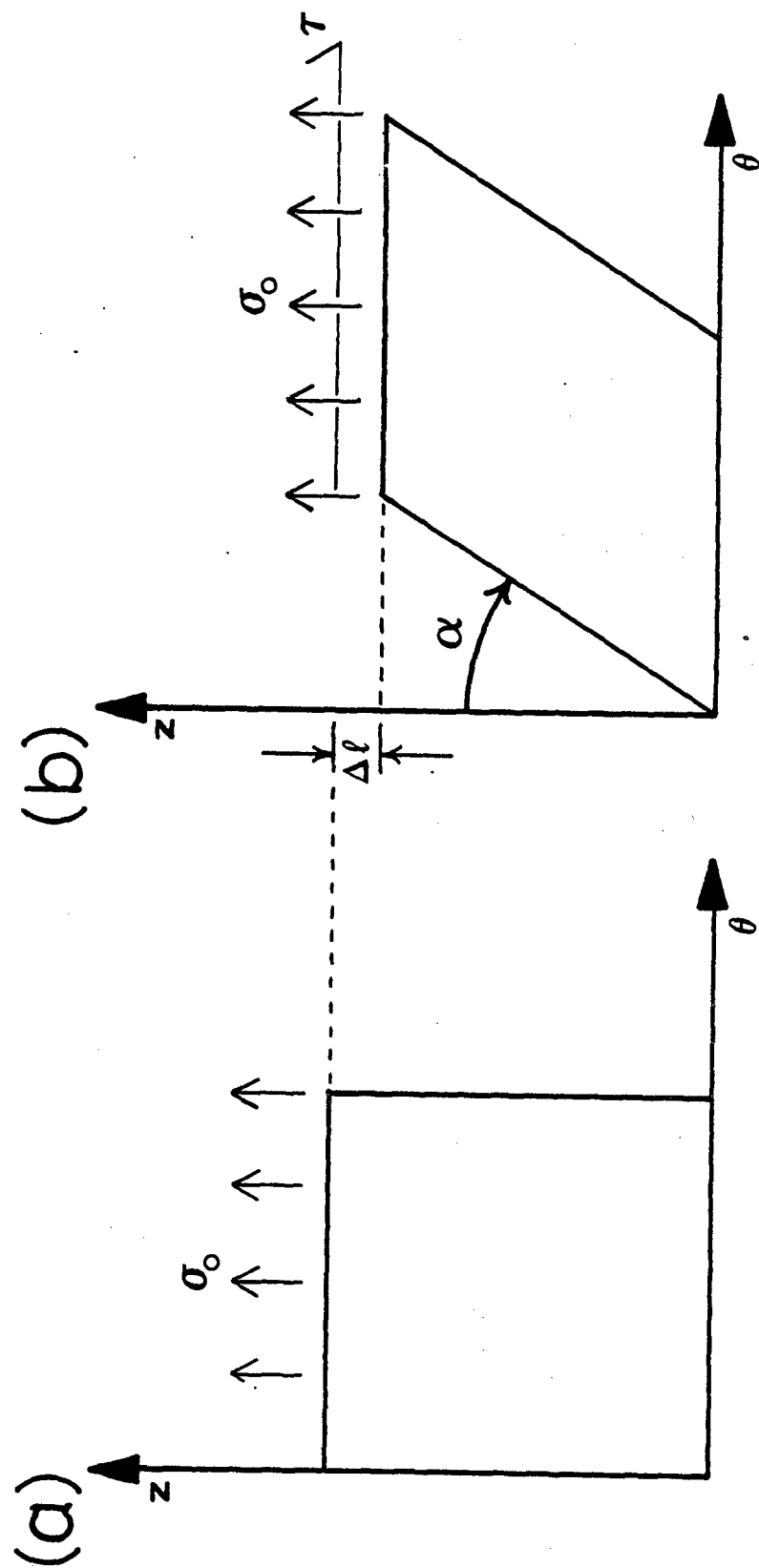


Figure 5.2. Simple shear of a material element subjected to a constant axial tensile stress.

For small shear strains, $\gamma \approx \alpha$ and $1 - \cos \alpha \approx \alpha^2/2$. Therefore (5.16) becomes:

$$W = \frac{\tau\gamma}{2} - \frac{\sigma_0 \alpha \gamma^2}{2} \quad (5.17)$$

This work due to external loads must be equal to the strain energy of the deformed element for conservative systems. The material is deformed from the initial state shown in Figure 5.2a by shear to the final state shown in Figure 5.2b. Therefore, the strain energy of this deformation is:

$$U = \frac{G\gamma^2}{2} \quad (5.18)$$

Equating (5.18) and (5.17) and rearranging yields:

$$\frac{\tau}{\gamma} = G + \alpha \sigma_0 \quad (5.19)$$

The ratio of shear stress to strain on the left side of this equation is defined as an apparent shear modulus G^* . This modulus is a measure of resistance of the element under stress σ_0 to shear deformation. Substitution of G^* into (5.19) yields:

$$G^* = G + \alpha \sigma_0 \quad (5.20)$$

which shows that the apparent shear modulus increases linearly with σ_0 . Foye neglected both the effects of volume changes which are necessary to give axial contraction with simple shear and the effects of the resistance of the material to such volume changes. Therefore, he obtained a similar relationship between apparent shear modulus and axial stress, except that $\alpha=1$ (maximum axial contraction with shear) in his result.

The effect predicted by (5.20) is not an increase in the true shear modulus of a material; rather, it is the apparent increase in resistance to the particular shear deformation shown in Figure 5.2 due to the additional work required to effect axial contraction against axial stress σ_0 during shear.

The extension of Foye's two-dimensional analysis to the problem of torsion of a solid cylinder under applied constant axial tensile stress can be made using a similar strain energy analysis. The initial state of the cylinder is defined as the cylinder under applied axial stress σ_0 . Therefore, the analysis for coupling between torsion modulus and σ_0 need only consider the work and energy changes that are due to twisting.

The energy balance for static equilibrium of a cylinder that is twisted while subjected to a constant axial tensile stress is:

$$W_1 + W_2 = U_1 + U_2 \quad (5.21)$$

where: W_1 = work due to torque required to twist cylinder through an angle ψ

W_2 = work done by cylinder as it contracts axially against the applied tensile stress

U_1 = shear strain energy due to torsion

U_2 = axial normal strain energy due to internal strain distribution

The work W_1 is the area under the torque-twist angle curve, which for linear-elastic deformation is:

$$W_1 = \frac{M_t \psi}{2} \quad (5.22)$$

where M_t is the applied torque. Equation (5.22) can be written in terms of an apparent shear modulus G^* that describes the resistance of the

cylinder to twisting. For a circular cylinder of length ℓ_0 and radius R (5.22) may be written as [93]:

$$W_1 = \frac{G\pi R^4 \psi^2}{4\ell_0}$$

The work W_2 is the product of the applied axial tensile force P_0 and the axial contraction due to twisting $\Delta\ell$:

$$W_2 = P_0 \Delta\ell \quad (5.24)$$

In terms of the applied axial stress $\sigma_0 = P_0 / \pi R^2$ and the axial contraction given by (5.15), (5.24) may be written as:

$$W_2 = - \frac{\sigma_0 a \pi R^4 \psi^2}{4\ell_0} \quad (5.25)$$

where the constant a has been inserted in (5.15) for reasons discussed earlier.

The shear strain energy associated with torsion of a cylinder of shear modulus G is [93]:

$$U_1 = \frac{G\pi R^4 \psi^2}{4\ell_0} \quad (5.26)$$

For anisotropic cylinders, it is assumed that $G = G_{z\theta}$.

There is additional strain energy U_2 due to the internal axial stresses which arise with twisting. This stress distribution for the case where $\alpha=1$ was obtained by Timoshenko and is given by (5.14). The strain energy of the stress distribution may be calculated from:

$$U_2 = \frac{\pi \ell_0}{E} \int_0^R \sigma^2 dr \quad (5.27)$$

Multiplication of (5.14) by the empirical constant a and substitution of the result in (5.27) yields, after integration:

$$U_2 = \frac{Ea^2\pi R^6\psi^4}{96\ell_0^3} \quad (5.28)$$

Collecting all the energy terms (5.23), (5.25), (5.26) and (5.28) and substituting them into (5.21) gives:

$$\frac{G^*\pi R^4\psi^2}{4\ell_0} - \frac{\sigma_0 a \pi R^4\psi^2}{4\ell_0} = \frac{G\pi R^4\psi^2}{4\ell_0} + \frac{Ea^2\pi R^6\psi^4}{96\ell_0^3} \quad (5.29)$$

Solving this equation for G^* yields:

$$G^* = G + a\sigma_0 + \frac{Ea^2R^2\psi^2}{24\ell_0^2} \quad (5.30)$$

Recalling that the maximum shear strain due to torsion of a circular cylinder is equal to $\gamma_m = \psi R / \ell$, (5.30) can be written as:

$$G^* = G + a\sigma_0 + \frac{Ea^2}{24} \gamma_m^2 \quad (5.31)$$

Although anisotropic polymer fibers exhibit tensile moduli E that may be two orders of magnitude greater than their longitudinal shear moduli G , the effect of axial tensile stress on apparent torsion modulus of these materials at small torsion strains can be approximated by:

$$G^* \approx G + a\sigma_0 \quad (5.32)$$

Comparison of (5.32) with (5.20) reveals that the effect of axial tensile stress on apparent shear modulus predicted by Foye using a two-dimensional analysis is identical to the effect of axial tensile stress

on the apparent torsion modulus of a solid cylinder obtained above. In both cases the dependence of G^* on σ_0 has been modified by the empirical constant α that was introduced to account for axial contraction that is less than the maximum predicted value.

Note that both (5.20) and (5.32) only apply to small, elastic shear strain behavior. Furthermore, it is emphasized that the true shear modulus G does not change to give the effect predicted by (5.20) and (5.32). The apparent change in shear modulus results from axial contraction with shear against an applied constant tensile stress. This effect is not expected for materials that do not contract axially with shear.

5.2 Experimental

The coupling of axial normal strains with torsional shear strains was investigated for five high performance polymer fibers and a glass fiber. The polymer fibers include poly(p-phenylene terephthalamide) (PPTA), poly(p-phenylene benzobisthiazole) (PBT), poly(2,5-benzoxazole) (ABPBO), a nematic thermotropic polyester (NTP) fiber and a gel-spun polyethylene (PE) fiber. A K-glass fiber was tested for comparison of this isotropic material with the highly anisotropic polymer fibers. The chemical structures, tensile and compressive properties and torsion moduli of the polymer fibers are found in Chapter 4 of this dissertation.

In the foregoing discussion of the relationship between torsion shear strain γ and axial normal strain ϵ , an empirical constant α was

defined as the fraction of maximum predicted axial contraction that occurs with twisting to small shear strains. The equation relating axial contraction Δl to angle of twist ψ for a solid cylinder is obtained by multiplying (5.15) by α to give:

$$\Delta l = \frac{-\alpha \psi^2 R^2}{4l_0} \quad (5.33)$$

One method of determining the constant α would be to directly measure the axial contraction of a fiber with twist. However, because the contraction is a second-order effect, the magnitude of Δl is extremely small for small twist angles ψ and is difficult to measure with precision.

Instead, it was decided to take advantage of the relatively large axial moduli of the fibers to calculate the constant α from measurements of the change in axial tension with twist of a fiber held at constant length. Because the fiber is held at constant length in this experiment, the axial contraction due to twisting is prevented by the generation of an axial stress which stretches the fiber to maintain the constant length. Small stretching or axial strains generate relatively large axial stresses in the stiff high performance fibers, which can be measured with relatively good precision using a sensitive tensile load cell.

The relationship between axial contraction Δl , twist angle ψ and tensile force P can be written as the total differential:

$$\left(\frac{\partial l}{\partial \psi}\right)_P = -\left(\frac{\partial l}{\partial P}\right)_\psi \left(\frac{\partial P}{\partial \psi}\right)_l \quad (5.34)$$

Noting that $\Delta\ell = \ell - \ell_0$, where ℓ is the fiber length after twisting through an angle ψ , then the change in length with twist at constant load can be obtained directly from differentiation of (5.33) to yield:

$$\left(\frac{\partial \ell}{\partial \psi}\right)_P = \frac{-\alpha \psi R^2}{2\ell_0} \quad (5.35)$$

The first term on the right-hand side of (5.34) can be related to the axial tensile modulus of a fiber at any twist angle ψ . For axial deformation:

$$\sigma = E\epsilon \quad (5.36)$$

where $\sigma = P/\pi R^2$, E = axial tensile modulus and $\epsilon = (\ell - \ell_0)/\ell_0$ for small strains. Substitution of these identities into (5.36) and rearrangement to solve for ℓ yields:

$$\ell = \ell_0 \left(\frac{P}{\pi R^2 E} + 1 \right) \quad (5.37)$$

Differentiating with respect to the tensile force P gives:

$$\left(\frac{\partial \ell}{\partial P}\right)_\psi = \frac{\ell_0}{\pi R^2 E} \quad (5.38)$$

where it is noted that E is the axial modulus at a twist angle ψ .

The last term in (5.34) is obtained from measurements of axial tensile force generated by twisting a fiber at constant length. For small angles of twist (i.e., small shear strains γ) the tensile force-twist angle relationship is of the form:

$$P = m\psi^2 + P_0 \quad (5.39)$$

where m is a constant and P_0 is the initial tensile load in the fiber at ψ_0 . This parabolic relationship between tensile load and twist angle

is a direct consequence of the dependence of axial contraction on the square of twist angle given by (5.33).

Differentiation of (5.39) with respect to ψ yields:

$$\left(\frac{\partial P}{\partial \psi}\right)_L = 2m\psi \quad (5.40)$$

Substitution of (5.35), (5.38) and (5.40) into the total differential (5.34) yields, after rearranging to solve for α :

$$\alpha = \frac{4\ell_0^2 m}{\pi R^4 E} \quad (5.41)$$

The relationship (5.39) and values of E at various angles of twist ψ are easily obtained by twisting a fiber that is held clamped in a tensile test machine at constant length. Approximately 20 cm long lengths of fiber were clamped in an Instron Universal Testing Machine equipped with a load cell capable of measuring 10g force full-scale. A paper tab was glued to the center of the fiber with epoxy. The fiber was then stretched by displacement of the Instron crosshead to put a small initial tension P_0 in the fiber.

A clamped fiber thus mounted was twisted at constant length by rotating the centrally bonded tab. This test configuration consists of twisting two fibers of equal length connected in series. Because the fibers are in series, the tensile force in each is identical. The measurements of force versus twist angle must be made at constant length. Therefore, it is crucial that the tab be glued to the exact center of the length of fiber that is clamped in the Instron. Long fiber lengths were used to minimize errors due to machine compliance.

The change in tensile force with twisting and untwisting at constant length was measured for each fiber. The maximum twist angle was kept within the range of elastic torsion deformation that was determined from separate experiments to be described subsequently. Linear regression analysis of P versus ψ^2 was performed to determine the constant m defined by (5.39).

The measurement of tensile modulus of fibers held twisted at several angles ψ throughout the range of elastic torsion deformation demonstrated that there was no significant change in the tensile modulus due to twisting for any of the fibers. Therefore, the value of E used to calculate the constant a from (5.41) is a constant for each fiber, independent of the twists ψ applied in these tests.

The range of elastic torsion deformation for each polymer fiber was determined from the onset of irreversible deformation with twisting. For these tests a 2 cm length of fiber was clamped at one end and bonded to a paper tab at the other. The end bonded to the tab was allowed to hang freely and attain a rest position. This free end was twisted a known amount, then allowed to untwist while the amount of this recoverable twist was measured. After a single test, a sample was discarded and a new one used for each subsequent test. The amount of applied twist was increased until the measured recoverable twist was noticeably less than the applied.

Plots of recoverable versus applied twist were made in terms of recoverable versus applied fiber surface shear strain. The applied surface shear strain corresponding to the onset of irrecoverable

deformation was determined from these plots. Because the maximum strain in a twisted fiber occurs at the surface, the surface shear strain at the onset of irrecoverable twist was defined as the critical shear strain γ_c .

This technique has been used to measure a critical shear strain of 10% for Kevlar 49 (PPTA) fibers [19]. In this previous study, the critical shear strain was shown to correspond to the initiation of longitudinal splitting of the fiber surface. In the present study, optical microscopic observations of highly twisted polymer fibers revealed internal fiber damage that closely resembled compressive kink band formation (see Chapter 4). This phenomenon was investigated by twisting fiber samples to various levels to determine the onset of this internal deformation. The surface shear strain corresponding to the initiation of these bands is defined as the critical shear strain to kink band formation γ_k .

The deformation of fiber surfaces was examined using an ETEC Auto-scan scanning electron microscope (SEM). The internal deformation of twisted fibers was observed using a Zeiss polarizing optical microscope.

The effect of axial tensile stress on the torsion shear modulus of fibers was measured using a modification of the torsion pendulum technique described in Chapter 4. The modification involves bonding one length of fiber at its top end to a rigid clamp, threading the fiber through a disc pendulum to which it is subsequently bonded, and bonding the bottom end to a weight. A schematic of this test configuration is shown in Figure 5.3. The small arrows in this figure indicate where the

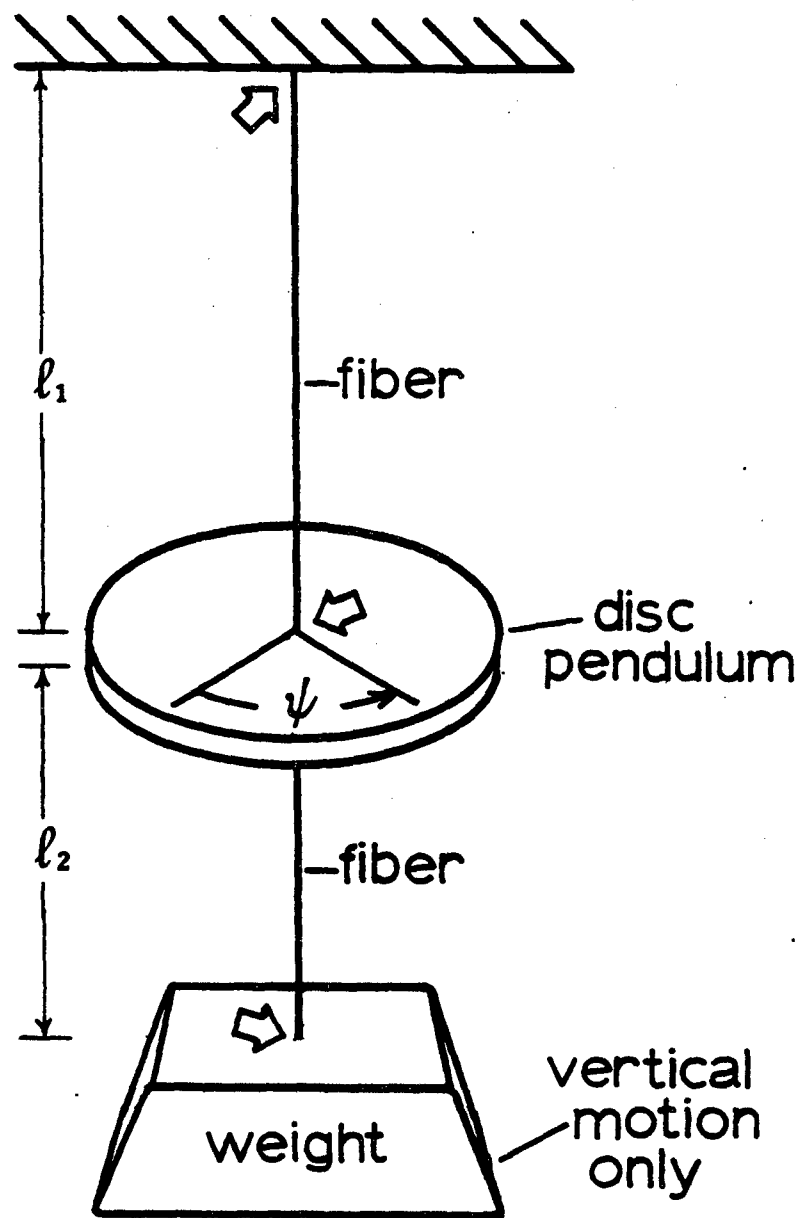


Figure 5.3. Schematic of apparatus used for torsion modulus-axial tensile stress measurements.

fiber is bonded. The weight that hangs from the bottom of the fiber is free to move vertically, but is fixed against rotation.

The torsion shear modulus is calculated from measurements of the period of oscillation of the centrally bonded disc pendulum. This test configuration is the torsion of two fibers in series, from which the shear modulus is calculated using:

$$G = \frac{8\pi I_d}{\tau^2 r^4} \left(\frac{l_1 l_2}{l_1 + l_2} \right) \quad (5.42)$$

where I_d = polar moment of inertia of the disc pendulum

τ = period of oscillation

r = fiber radius

l_1, l_2 = lengths of fiber above and below pendulum

The advantage of this particular test is that the only variable is the weight hung from the fiber--that is, the axial tensile stress in the fiber. The disadvantage of this technique is that the length of fiber below the disc pendulum is always under less tensile stress than the length above the disc due to the pendulum weight. However, the test is performed to determine the change in torsion modulus with applied tensile stress, and this variation is identical for both lengths of fiber.

The diameters of all fibers except PE were measured using a laser diffraction technique [72]. The PE fibers have irregular cross-sections and a value of $1.13 \times 10^3 \mu\text{m}^2$ for cross-sectional area was calculated from the linear density.

5.3 Results

The tensile force-twist behavior at constant fiber length could be adequately fitted to (5.39) for PPTA, PBT, ABPBO and NTP fibers. A graph of tensile force P versus twist angle ψ for PPTA is shown in Figure 5.4. The force data were also plotted against ψ^2 to demonstrate the parabolic relationship between P and ψ .

The characteristics of PPTA fiber shown in Figure 5.4 were found to be similar to those of PBT, ABPBO and NTP fibers. All fibers exhibited the small hysteresis seen in this figure for PPTA upon untwisting. Moreover, every fiber sample retained some permanent, irrecoverable twist, which was detected by allowing the centrally bonded tab to unwind freely.

A linear regression analysis of P versus ψ^2 yielded the slopes m and correlation coefficients r listed in Table 5.1. These slopes represent the average for the two values obtained from twisting and untwisting. A value of the constant α was calculated for each fiber using (5.41) and the data given in Table 5.1.

Twisting a glass fiber held at constant length resulted in a small decrease in tensile force, indicating that this fiber elongates with twist. The change in tensile force with twist was too small to enable a slope m and therefore a constant α to be calculated with any accuracy for glass.

The constant α ranged from 0.70-0.85 for the four polymer fibers. These values are all less than unity, indicating that there is less contraction than the maximum predicted by Timoshenko (5.15).

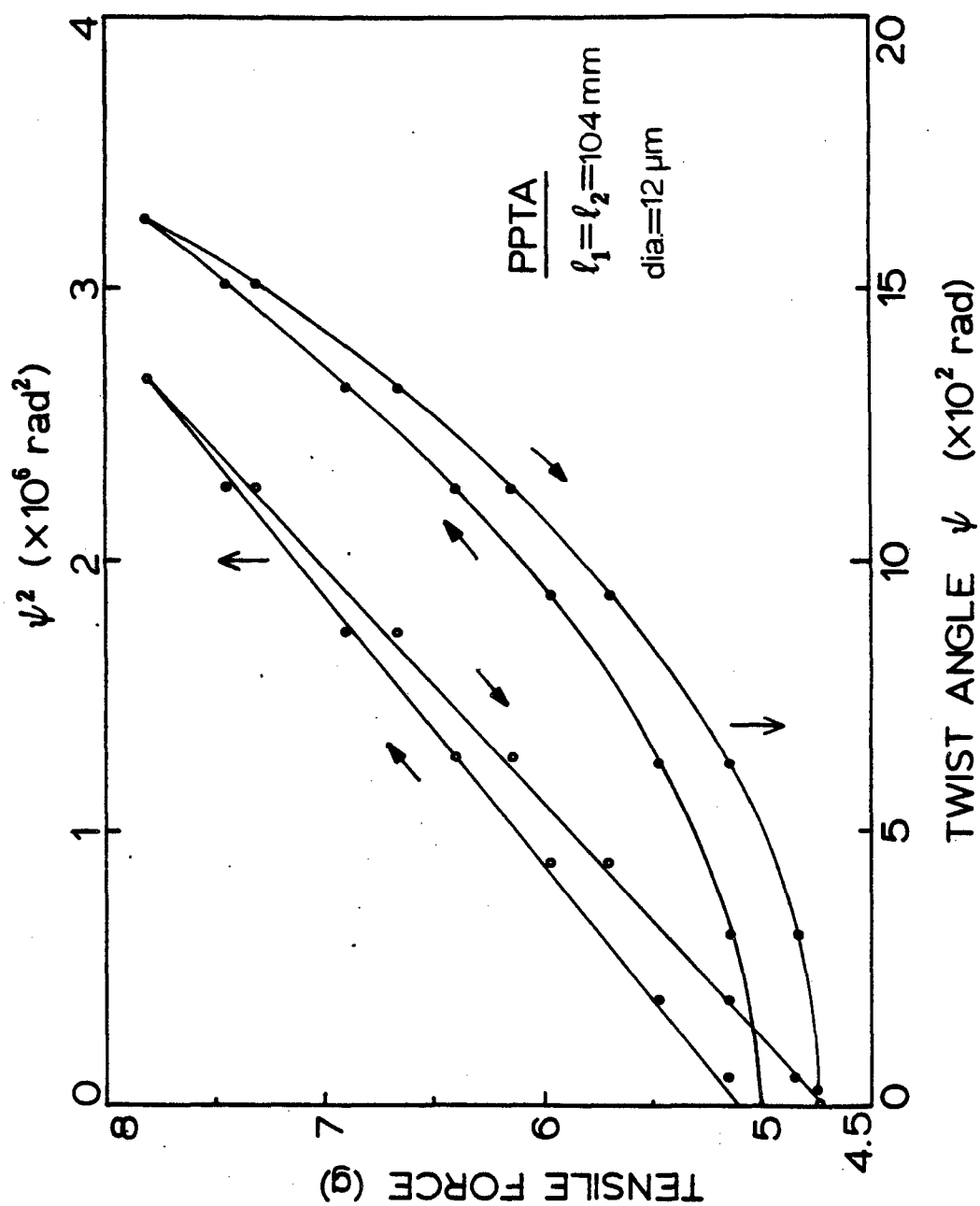


Figure 5.4

Tensile force-twist behavior at constant length for PPTA fiber.

Table 5.1

Linear Regression Data for Tensile Force
Versus Twist Angle Measurements and
Calculation of Constant a

Fiber	$m(\text{g/rad}^2 \times 10^6)$	r	Fiber Length ^a (mm)	Fiber Radius (μm)	Tensile Modulus (GPa)	a^b
PPTA	1.08	0.9994	103.5	6.1	123	0.85
PBT	3.53	0.9995	96.5	6.5	265	0.85
ABPBO	3.20	0.9993	93.5	8.3	117	0.70
NTP	11.4	0.9986	94.0	12.0	77	0.80
K-Glass	(-)	-	94.0	6.4	70	<0

$P = m\psi^2 + P_0$; r = correlation coefficient

^aLength above and below centrally bonded paper tab.

^bCalculated using equation (5.41).

Inspection of (5.41) confirms that the error in α is at least four times the error in the radius. Measurements of fiber radii along lengths comparable to those used for force-twist measurements were accurate to approximately 5%. Therefore, the values of α listed in Table 5.1 are precise to no less than 20%.

The elastic torsion deformation range as defined by the critical shear strain γ_c was determined from plots of normalized recoverable strain versus applied strain as shown in Figure 5.5 for ABPBO. Similar behavior was observed for PPTA, PBT and NTP fibers. After twisting to surface shear strains equal to or greater than γ_c , the recovery (untwisting) of NTP fibers became noticeably time-dependent. Therefore, NTP fibers were allowed to untwist for a few minutes before taking a measurement of recoverable shear strain. The values of γ_c for the polymer fibers are given in Table 5.2.

Values of critical surface shear strain to internal kink band formation γ_k are also listed in Table 5.2. The range of values for γ_k represents the variation in shear strain required to initiate visible kink bands in several samples of one type of fiber. Optical micrographs of internal kink bands in PPTA, PBT, ABPBO and NTP fibers held twisted to strains greater than γ_k are shown in Figure 5.6. The obliquely oriented bands occur at angles to the fiber axis which are identical to the orientation angles of kink bands formed by axial compression of the same fibers (see Chapter 4). In twisted fibers these bands are predominantly confined to the center of the fiber, which suggests that internal axial compressive failure occurs due to torsion.

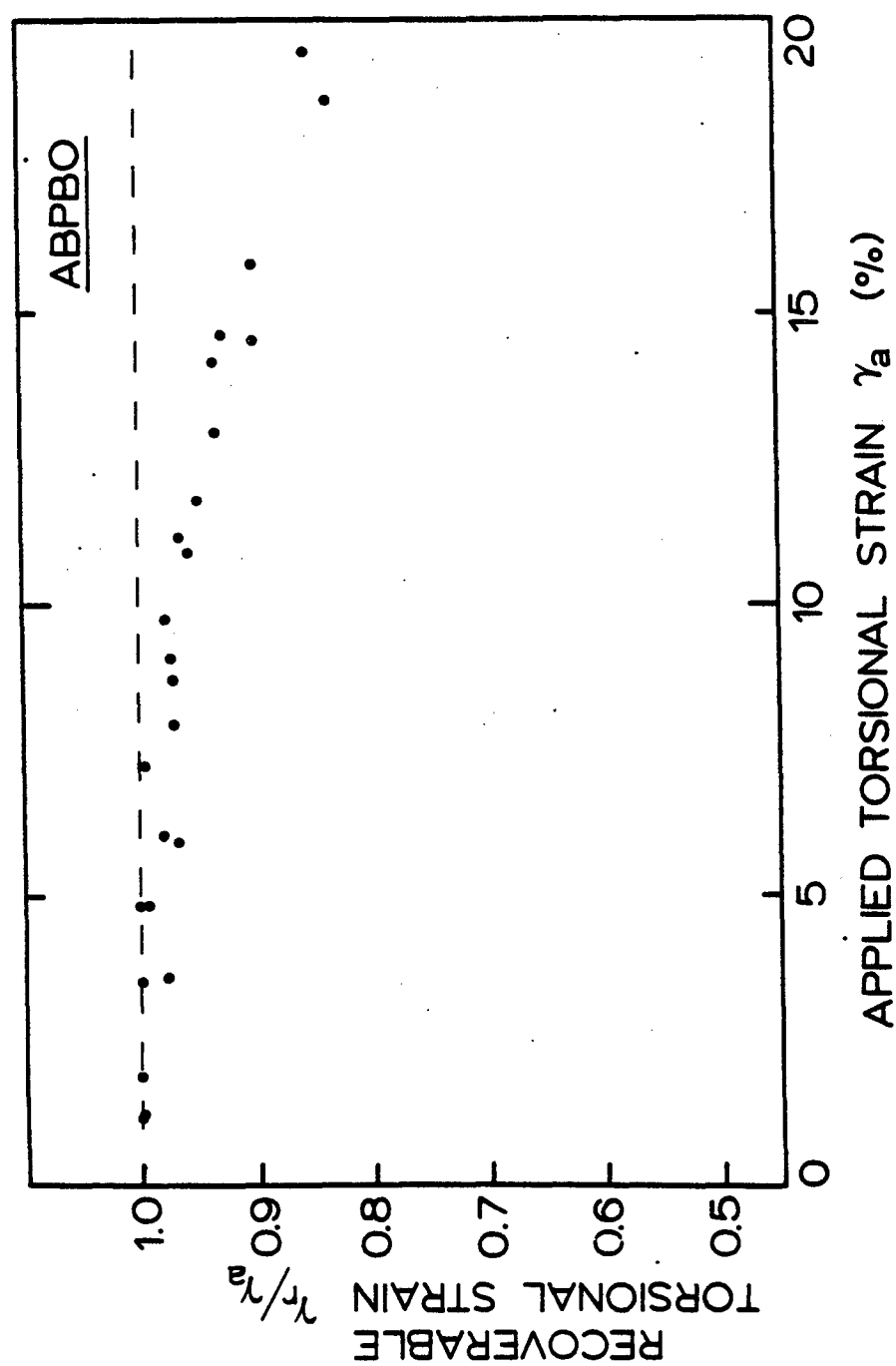


Figure 5.5. Plot used to determine elastic torsion deformation range for ABPBO fiber.

Table 5.2

Critical Shear Strains to Inelastic Torsion Deformation
and Internal Kink Band Formation

Fiber	γ_c (%)	γ_k (%)	ϵ_m^a (%)	ϵ_c^b (%)
PPTA	10	14-15	0.42-0.48	0.50
PBT	3-4	6-7	0.08-0.10	0.10
ABPBO	10	10-12	0.18-0.25	0.18
NTP	10	8-9	0.13-0.16	0.15

^aMaximum axial compressive strain due to twist = $-\alpha\gamma_k^2/4$.

^bCritical axial compressive strains to kink band formation (Chapter 4).

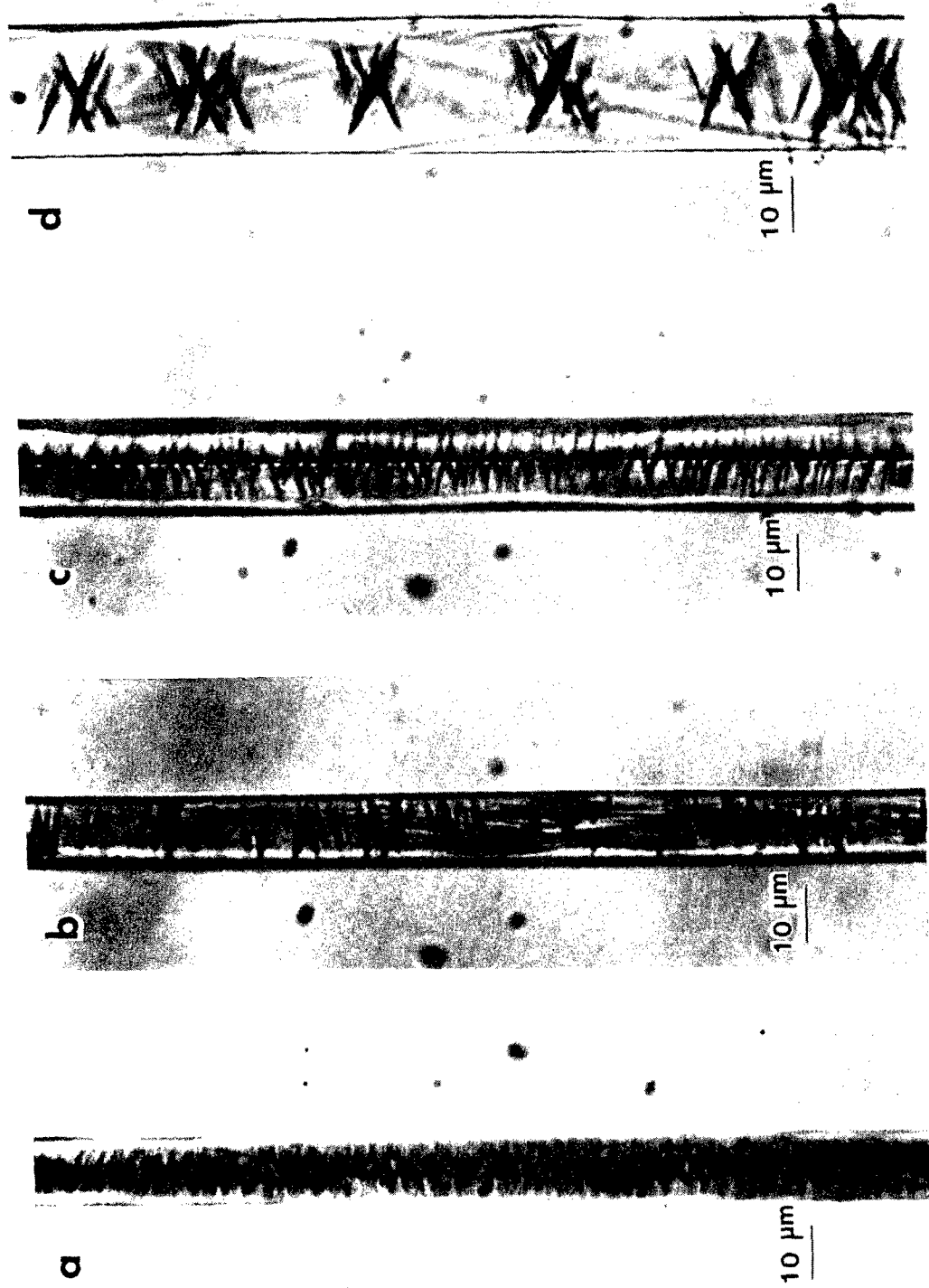


Figure 5.6

Optical micrographs of fibers held twisted at large torsion strains. (a) PPTA, $\gamma_m = 40\%$. (b) PBT, $\gamma_m = 20\%$. (c) ABPBO, $\gamma_m = 20\%$. (d) NTP, $\gamma_m = 20\%$.

Further proof that axial compressive failure occurs due to torsion is obtained from the comparison of ϵ_m , the maximum internal compressive strains occurring with torsion to surface strains γ_k , with ϵ_c , the critical compressive strains to kink band formation. The internal compressive strains may be calculated using equation (5.14) for the internal axial normal stress distribution after multiplication by the constant a to give:

$$\epsilon = \frac{a\sigma}{E} = \frac{a\psi^2}{2\ell_0^2} \left(r^2 - \frac{R^2}{2} \right) \quad (5.43)$$

The maximum compressive strain occurs at the fiber axis ($r=0$). Noting that $\gamma_m = \psi R/\ell_0$, the maximum compressive strain of the distribution given by (5.43) may be written in terms of γ_k as:

$$\epsilon_m = - \frac{a\gamma_k^2}{4} \quad (5.44)$$

Values of compressive strain calculated using (5.44) and critical axial compressive strains to kink band formation determined for each fiber in Chapter 4 are given in the last two columns of Table 5.2. Clearly, the internal compressive strains due to shearing to strains γ_k are sufficient to initiate kink band formation in these fibers.

SEM observations of twisted fibers revealed longitudinal surface scratches and splits as shown in Figure 5.7 for NTP fiber twisted to a shear strain greater than γ_c . However, similar surface markings were observed on the surfaces of PBT, ABPBO and NTP fibers prior to twisting, making assessment of damage to the fiber surface due to twisting difficult. PPTA fibers exhibit a relatively smooth surface, and therefore it

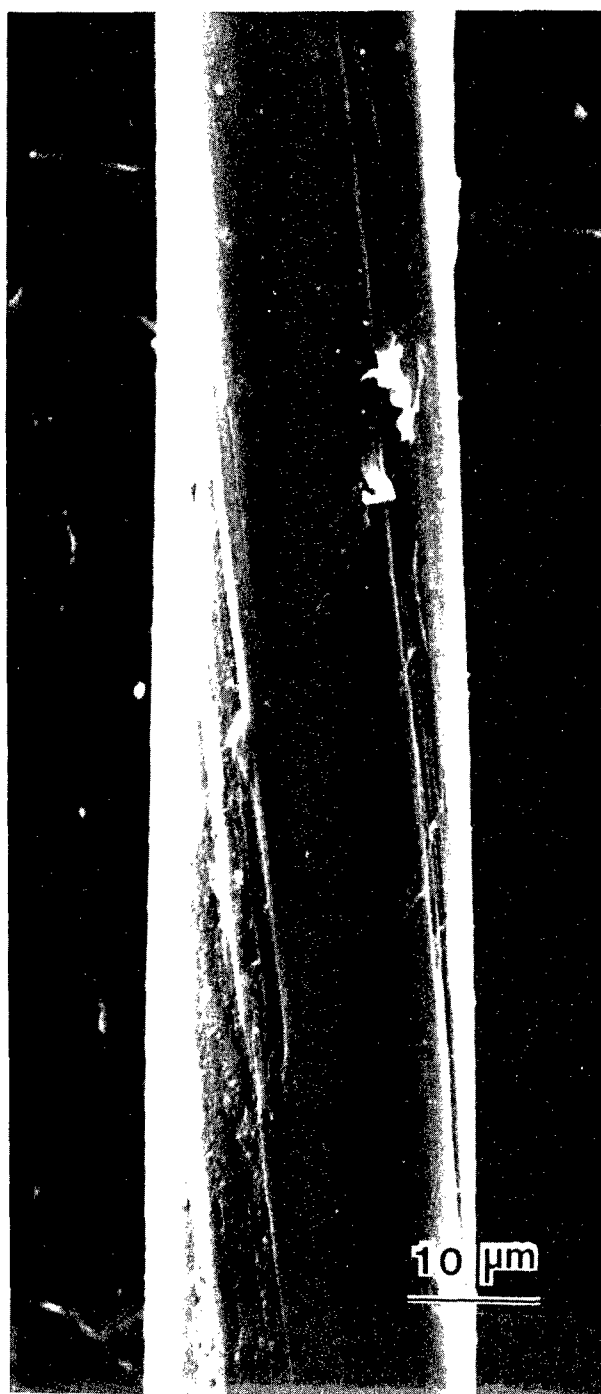


Figure 5.7

SEM micrograph of NTP fiber held twisted
at a surface torsion strain $\gamma_m = 20\%$.

was easy to determine that surface splitting coincided with the onset of irrecoverable torsion deformation [19]. However, in light of the similarity of γ_c and γ_k , especially for ABPBO and NTP fibers, it appears that torsion failure, as defined by the onset of irrecoverable deformation, is due to either shear failure of the fiber surface or axial compressive failure of the fiber core.

Although the exact torsion strains for irrecoverable torsion deformation and torsion-induced kink band formation could not be determined for the PE fibers due to their irregular cross-sections, kink bands were observed in highly twisted PE fibers. These kink bands can be observed in optical and scanning electron micrographs of twisted PE fibers, as shown in Figure 5.8a,b. The kink bands are nearly perpendicular to the fiber axis and occur with regular periodicity along this axis.

The samples of PE fiber shown in Figure 5.8a,b have a nearly rectangular cross-section. Timoshenko has calculated the torsion-induced axial normal stress (and strain) distribution for isotropic rectangular prismatic bars, predicting that the maximum axial compressive stress occurs in the center of the surface of the wide face of the bar [86]. Inspection of Figure 5.8b shows that the transverse kink bands are confined to the central region of the surface of the wider face of the fiber, thereby indicating that axial compressive failure occurred with torsion.

All fibers exhibited excellent linear correlation between apparent torsion modulus G^* and applied axial tensile stress σ_0 as predicted by

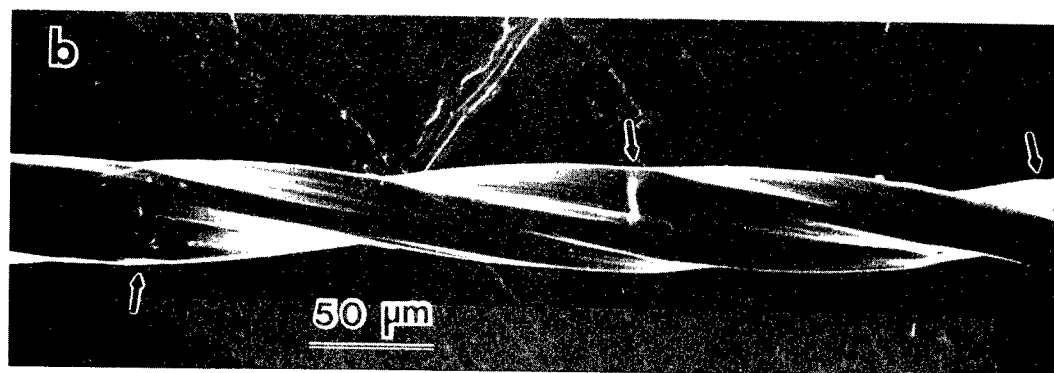
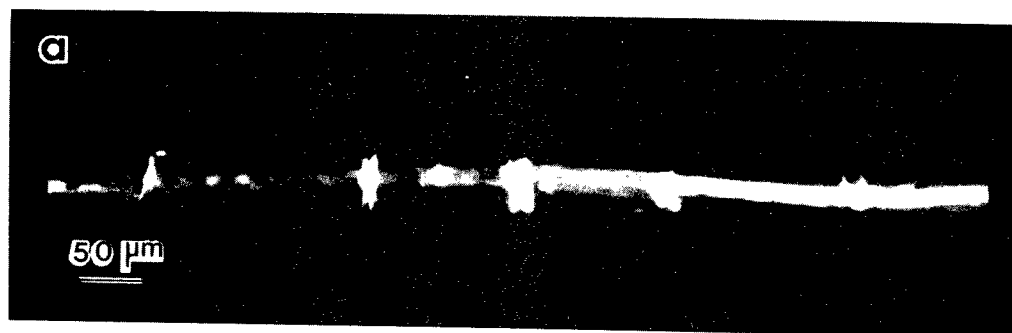


Figure 5.8

(a) Optical and (b) SEM micrographs of highly twisted PE fiber. Fiber between cross polars, parallel to analyzer, in (a).

(5.32). A plot of G^* versus σ_0 for PBT fiber is shown in Figure 5.9. The values of G^* measured for increasing and decreasing σ_0 were identical within experimental error.

Linear regression analysis yielded slopes α and correlation coefficients r given in Table 5.3. The true shear moduli, i.e., the intercepts, were obtained from independent measurements performed in Chapter 4. Comparison of the constants α determined from the slope of G^* versus σ_0 with those obtained from tensile force-twist measurements and given in Table 5.1 shows that there is relatively good agreement of these values for all fibers tested. Therefore, it appears that the increase in torsion modulus with axial tensile stress is due solely to the axial contraction that occurs with twist.

There was no measureable effect of tensile stress on the torsion modulus of glass fiber. This result is in agreement with the relatively small axial elongation observed during twisting of glass fibers. A linear decrease in torsion modulus with increasing axial stress would be expected based on the observed elongation with twisting of glass fibers. However, the small elongation with twist and the relatively large shear modulus of glass presumably render the effect of tensile stress on apparent torsion too small to be detected.

The last column in Table 5.3 shows the maximum axial tensile stress, as a percentage of the stress at break, that was applied to each fiber for torsion modulus measurements. The linear increase in apparent torsion modulus persisted up to tensile stresses that were approximately 50% of the break stress for all fibers.

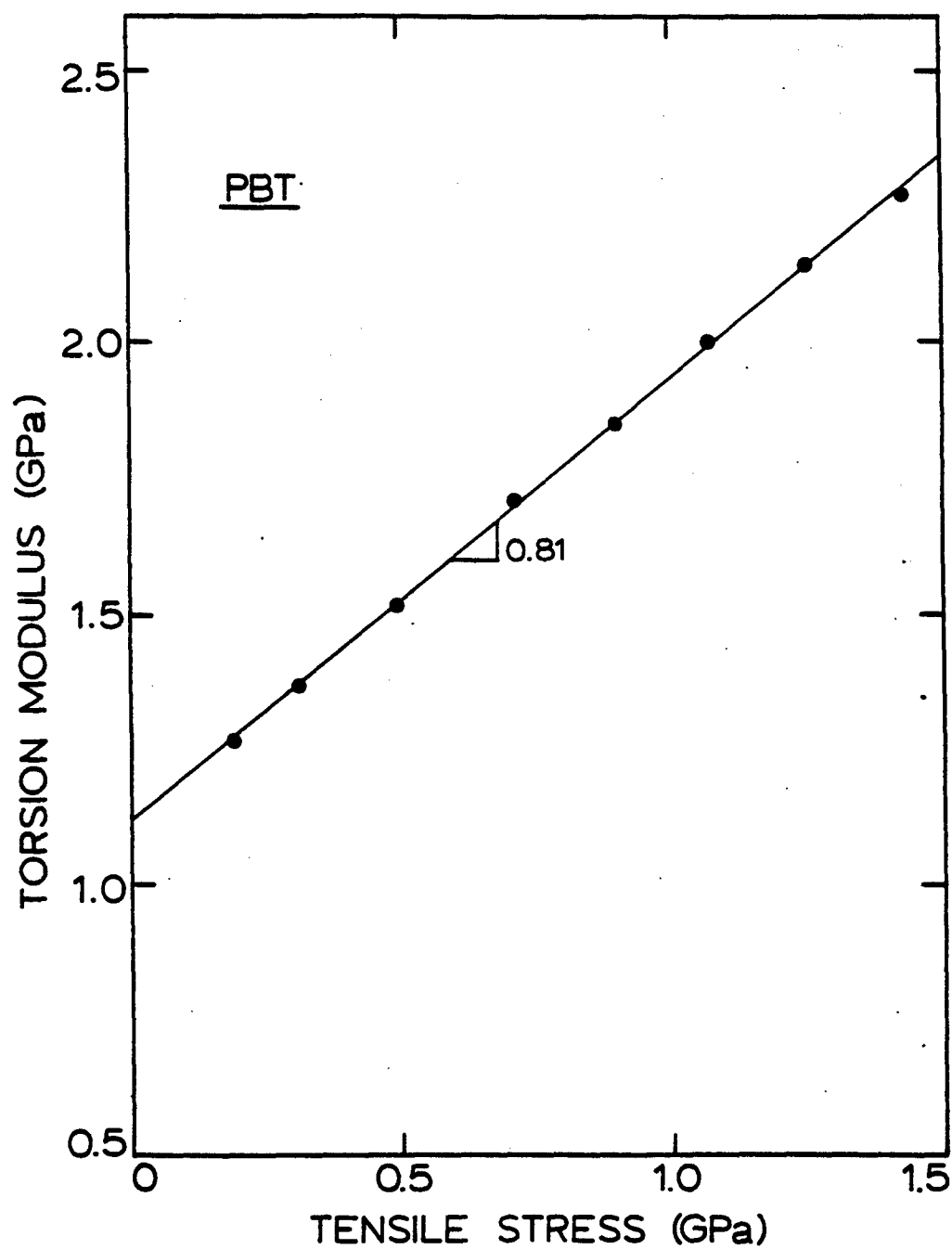


Figure 5.9. Torsion modulus-axial tensile stress behavior of PBT fiber.

Table 5.3
Linear Regression Data for Apparent Torsion Modulus
Versus Axial Tensile Stress Measurement

Fiber	G^a (GPa)	a	r	$\% \sigma_u^b$ (%)
PPTA	1.5	0.8	0.9996	54
PBT	1.2	0.8	0.9997	55
ABPBO	0.62	0.7	0.9999	63
NTP	0.45	0.7	0.9999	43
PE	0.7	-	0.9993	32 ^c
K-Glass	20	0.0	-	69

$$G^* = a\sigma_0 + G$$

^aTrue torsion moduli, measurements discussed in Chapter 4.

^bMaximum applied tensile stress, as percentage of ultimate tensile strength σ_u .

^cYield stress is approximately 15% of ultimate strength.

The linear increase in torsion rigidity with axial tensile stress was also observed for PE fibers. Unfortunately, the irregular cross-section of these fibers made determination of torsion modulus and therefore determination of constant α difficult. Note that the linear dependence of torsion rigidity on tensile stress was observed up to stresses significantly higher than the yield stress of PE fiber.

5.4 Discussion and Conclusions

Indirect measurements of axial contraction with twist of high performance polymer fibers showed that 70% to 80% of the maximum predicted contraction occurred for all fibers examined. Measurement of less-than-maximum axial contraction may be due to resistance of the fibers to the volume reduction concomitant with shear-induced contraction.

A glass fiber was observed to elongate with twist, although the relative magnitude of this elongation was much less than polymer fiber length contraction with twist. The behavior of the glass fiber is similar to other isotropic materials such as metal and rubber. Elongation of glass fibers with torsion could possibly be analyzed using nonlinear elasticity theory for isotropic materials.

Although the torsion-induced axial contraction of the anisotropic polymer fibers is a second-order effect, it results in unique behavior for these materials.

Relatively large torsional strains result in relatively small axial compressive strains in the core of polymer fibers. However, the

high axial moduli of these fibers translate the small axial compressive strains into significant axial compressive stresses. Therefore, there is a large amount of axial strain energy in these fibers at large torsional strains. This axial strain energy is expected to cause a non-linear increase in torsion modulus according to (5.31), which should be noticeable at large torsion strains.

Moreover, the low compressive strength of the high performance polymer fibers limits the range of elastic deformation in torsion. The significant axial compressive stresses that are generated within these fibers with torsion are sufficient to cause internal compressive failure. Therefore, torsion may result in failure of these anisotropic fibers due to an effect which is only of second order. The observation of axial splitting on the surface of some fibers after twisting to shear strains similar to those which initiate internal compressive failure suggests that either shear or compressive failure or both lead to the onset of inelastic torsion deformation.

A predicted linear increase in torsion modulus at small shear strains with applied constant axial tensile stress was observed for all polymer fibers examined. This apparent increase in modulus could be completely explained by the work required of the fiber to contract against the tensile stress with torsion. Therefore, there appears to be no change in the true shear modulus of the material due to axial stresses.

In his two-dimensional analysis of the relationship between apparent shear modulus and axial stress, Foye considered the effect of

compressive stress on shear modulus [92]. Compressive stresses do work on a material that contracts with simple shear and should therefore reduce the apparent shear modulus. This effect has been observed for fiber-reinforced composite tubes [94]. Foye predicted failure of fiber composites under compression due to onset of the instability that occurs when sufficient compressive stress is applied to cause the apparent shear modulus to vanish. This instability may be perceived as a total loss of resistance to shear deformation, which subsequently leads to collapse of the material in shear due to infinitesimal shear strains.

Consideration of the effect of axial compressive stress on the apparent torsion modulus of high performance polymer fibers leads to the conclusion that an instability (i.e., $G^*=0$) occurs when $\sigma_0 = -G/\alpha$. This prediction of compressive instability in these fibers is identical, except for the constant α , to the theoretical estimate of axial compressive strength obtained from the elastic microbuckling analysis presented in Chapter 3. The constant α was approximately equal to 0.75 for all polymer fibers tested. Therefore, the estimate of compressive strength obtained by applying Foye's analysis is about 33% higher than predicted by analysis of microbuckling instabilities.

However, the empirical constant α is very possibly a measure of the resistance of fibers to the volume reduction that occurs during twisting. In Chapter 3 it was shown that negative volume changes are avoided with compressive failure due to kink band formation if the band forms at oblique angles to the fiber axis. Therefore, because kink

bands form by simple shear without a volume decrease, the constant a may be assumed to equal unity and therefore the predicted compressive stress required to initiate elastic shear instability, i.e., $G^*=0$, is equal to the longitudinal shear modulus.

C H A P T E R V I
HELICAL COMPRESSIVE KINK BANDS IN CYLINDRICALLY
ORTHOTROPIC MATERIALS: WOOD AND PPTA FIBERS

6.1 Introduction

In studies of the axial compressive behavior of a high performance oriented polymer, Kevlar^R 49 fiber, it was observed that under uniform compression these fibers form helical kink bands with a pitch angle of approximately $60\frac{1}{2}$ on the fiber surface (Chapter 2). This formation of surprisingly regular helical kink bands in compressed Kevlar 49 fiber invited attempts at explanation based upon what is currently known about the fiber morphology.

Structural studies of Kevlar 49 fiber show that it is a crystalline material of cylindrically orthotropic symmetry [28-30]. (A cylindrically orthotropic material has three mutually perpendicular planes of structural symmetry which are parallel to a system of orthogonal cylindrical coordinates.) A more common example of a cylindrically orthotropic material is wood. In this chapter, results of a study of the axial compression of wood are presented with the intent of relating its compressive failure morphology to that of Kevlar 49 fiber. Additional results of observations of compressive kink band formation in Kevlar 49 fiber are also presented.

6.2 Background

The structures of both Kevlar 49 fiber and wood in its natural form are best described by a cylindrical coordinate system. The three orthogonal axes of this system are shown in Figure 6.1. For both materials the z-axis is the direction of highest strength and modulus. In wood science this axial direction is referred to as "parallel to grain" because it describes the orientation of the wood fibers and tracheids [95]. The axial direction of Kevlar 49 is the orientation axis of the extended polymer chains [23,24].

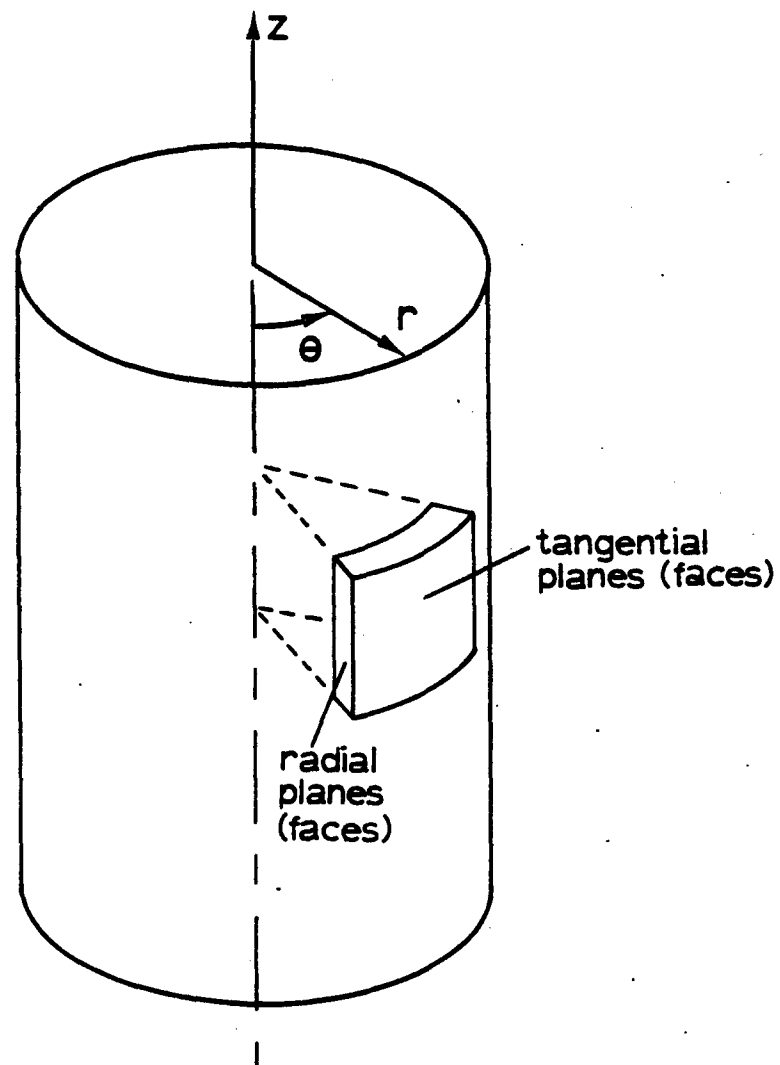
Cylindrically orthotropic materials exhibit symmetry in the cross section ($r\theta$ plane) such that the properties differ in the radial (r) and tangential (θ) directions. The transverse symmetry in wood results from the yearly accumulation of rings. Additionally, radially oriented tubular cells (wood rays) enhance the strength and stiffness of wood in the radial direction relative to the tangential direction [95]. This morphology gives most woods a measured mechanical anisotropy that can be ranked as:

$$E_z \gg E_r > E_\theta$$

$$\sigma_z \gg \sigma_r > \sigma_\theta$$

where E_i = tensile or compressive moduli and σ_i = tensile or compressive strengths. Moreover, the axial compressive strength of wood is usually less than half of the corresponding tensile strength.

Structural studies of Kevlar 49 fiber show that it also has transverse symmetry [28-30]. This symmetry is due to the average alignment



z : axial direction
 r : radial direction
 θ : tangential direction

Figure 6.1. Directions and planes of a cylindrical coordinate system.

of two lateral crystallographic axes along radial and tangential directions. In particular, one axis of the monoclinic unit cell is parallel to the direction of strong hydrogen bonding between polymer chains; this axis is oriented predominantly along the radial direction of the fiber. The other lateral axis of the unit cell is a direction of weaker secondary bonds between chains and is oriented along the tangential direction of the fiber. This arrangement of polymer chains in the fiber cross-section probably gives Kevlar 49 fiber a mechanical anisotropy that is qualitatively identical to the properties of wood. Kevlar 49 fiber further resembles wood in that its axial compressive strength is much lower than its axial tensile strength (Chapter 2).

To understand the mechanical behavior of both wood and Kevlar 49 fiber, it is helpful to model both materials as cylinders formed by a collection of hypothetical radial sheets. A "sheet" is the plane formed by the two mechanically strongest directions, i.e., the z- and r-axes. The relatively poor adhesion between these sheets corresponds to the strength and stiffness of each material in the tangential direction. The radial sheet model for Kevlar 49 fiber was originally proposed by Dobb et al. [28], and is adopted here to explain the compressive failure of both Kevlar 49 fibers and wood.

Observations of axially compressed Kevlar 49 fibers made in Chapter 2 have shown that such fibers exhibit V-shaped black lines when examined by light microscopy, and observations using scanning electron microscopy show these lines to be helical kink bands on the fiber

surface. SEM micrographs of this unusual compressive failure mode were shown in Figure 2.5.

Takahashi and coworkers used electron microscopy techniques to examine thin sections of compressively kinked Kevlar 29 fibers [37]. This variant of the Kevlar fibers also exhibits cylindrically orthotropic structural symmetry [30]. Furthermore, the compressive kink bands in Kevlar 29 fiber observed by Takahashi are similar to those observed in Kevlar 49. Takahashi showed that kink bands formed by shear slippage between radial hydrogen-bonded sheets and were oriented at 55° to the fiber axis in tangential sections (planes). Deformation within radial sections (i.e., hydrogen-bonded sheets) appeared as thin bands of buckled material oriented perpendicular to the fiber axis.

Reports on the compression testing of cylindrically orthotropic wood specimens appear to be limited to the compression of poles and pilings [96]. One study presented evidence of kink banding on the surface of compressed pilings [96], but these materials were defect-ridden and efforts to correlate structure with compressive failure modes were not made.

For practical reasons most wood compression tests are performed on lengths cut from the cross-section of the tree. These test specimens are not cylindrically orthotropic, but their structure is of course related to this orthotropy. The axial compression of wood sections can result in several failure modes [95]. Specimens which are free of defects (clear) and have a well-oriented grain usually fail due to the formation of kink bands, which are referred to as shear bands in wood

technology [53,95]. Microscopic examination of the material within the kink band reveals the kinking and buckling of the wood fibers and microfibrils [54].

It has been reported that for rectangular wood blocks having lateral faces parallel to radial and tangential planes, axial compression results in deformation bands that are usually oriented perpendicular to the axial direction (grain) on the radial faces and oriented at 60° to the axial direction on the tangential faces [53]. However, no pictures of this failure mode were provided. These orientations of compressive deformation bands on radial and tangential planes are identical to the orientations of bands in corresponding planes of compressed Kevlar 29 fibers observed by Takahashi [37].

Two questions are to be addressed in this study. First, why does Kevlar 49 fiber form helical kink bands under compression? Second, given the structural similarities between wood and Kevlar 49 fiber, does wood also form helical kink bands under axial compression?

6.3 Experimental

The formation of kink bands in Kevlar 49 fiber was observed at several levels of axial compressive strain above the critical strain for initiation of these bands. The technique employed for these observations is described in Chapter 4. Briefly, the method involves bonding single fibers to one surface of a transparent elastic beam which is subsequently bent in a manner that places the bonded fibers in axial

compression. The formation of kink bands in these compressed fibers can then be examined using optical microscopy.

The internal deformation in kinked Kevlar 49 fibers is revealed by the compression of the fiber tensile fracture surface. Single fibers were embedded in a nylon-6 matrix by solvent-casting a nylon film around the fibers. These fiber-containing films were stretched parallel to the fiber axis in order to break the embedded fiber in tension. Because the fiber fails in tension at low strains and the nylon matrix plastically deforms to relatively large tensile strains before it fails, stretching fiber-containing nylon films caused the fiber to break at several locations along its length prior to ultimate failure of the surrounding nylon matrix. Kink bands were observed in fibers fractured in this manner, thereby demonstrating that compressive stresses were generated in the fiber after tensile failure. This preparation resulted in compressive failure of the tensile-fractured end of the fiber, as well as compressive deformation of the internal regions of the fiber which had been exposed by tensile failure. It is believed that compression of the fiber subsequent to tensile failure occurs by snap-back of the fractured end [43] as well as by the elastic recovery of the nylon matrix which occurs upon removal of the tensile load. Fibers which were fractured in tension and then compressed as described above were recovered from the nylon matrix by dissolving the matrix with formic acid. These isolated fiber fragments were examined using scanning electron microscopy (SEM). A Zeiss polarizing microscope and an ETEC Autoscan SEM were used to examine Kevlar fibers.

Two geometries of wood samples were tested in axial compression. First, rectangular wood blocks with lateral faces cut parallel to radial and tangential planes were compression-tested to determine the orientations of deformation bands within these planes. A 1 in. x 1 in. sample of white pine post having the necessary symmetry was selected from a local lumberyard. Blocks 2 in. long were cut with parallel ends using a band saw. These blocks were axially compressed using an Instron Testing Machine at a crosshead speed of 0.1 cm/min. Second, cylindrically orthotropic samples of wood were prepared by turning down knot-free logs of eastern white pine on a lathe to remove bark and form right circular cylinders. Two cylinders, roughly 8 in. long and 3 in. in diameter, were axially compressed in the green state using a Riehle Testing Machine at a crosshead speed of 0.05 in./min.

6.4 Results

The formation of kink bands in Kevlar 49 fiber at increasing levels of axial compressive strain is shown in the optical micrographs in Figure 6.2. These micrographs show the appearance of the V-shaped black lines, which correspond to a helical kink band, as the level of compressive strain in one region of the fiber is increased. It is clear from these micrographs that the helical kink band propagates in both directions along the fiber axis with increasing compressive deformation.

An SEM micrograph of a Kevlar 49 fiber tensile fracture surface which was subsequently compressed is shown in Figure 6.3. A montage of micrographs was made in order to show the surface of the long axial

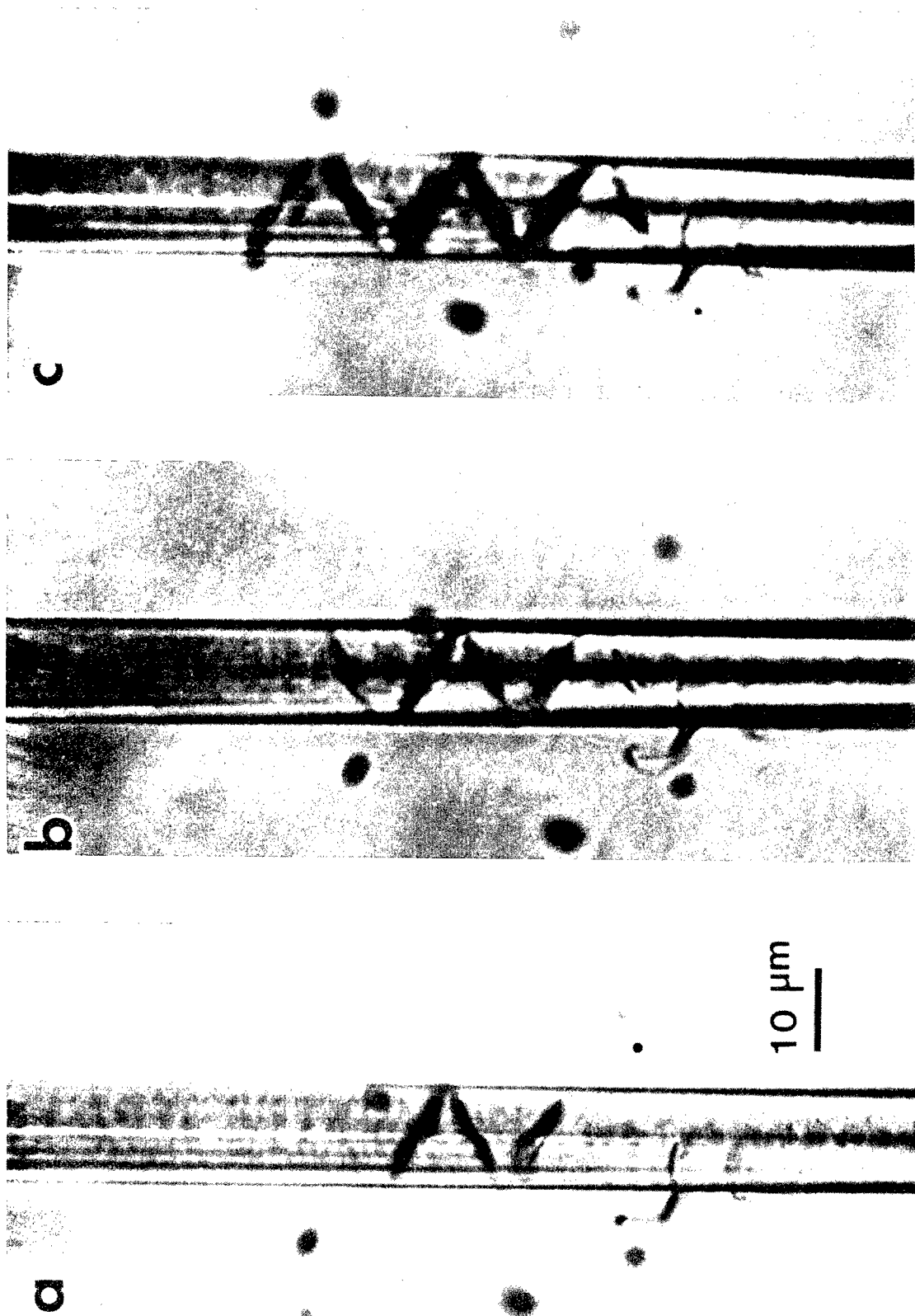


Figure 6.2

(a-c) Optical micrographs of one region of a Kevlar 49 fiber at increasing levels of axial compressive strain.

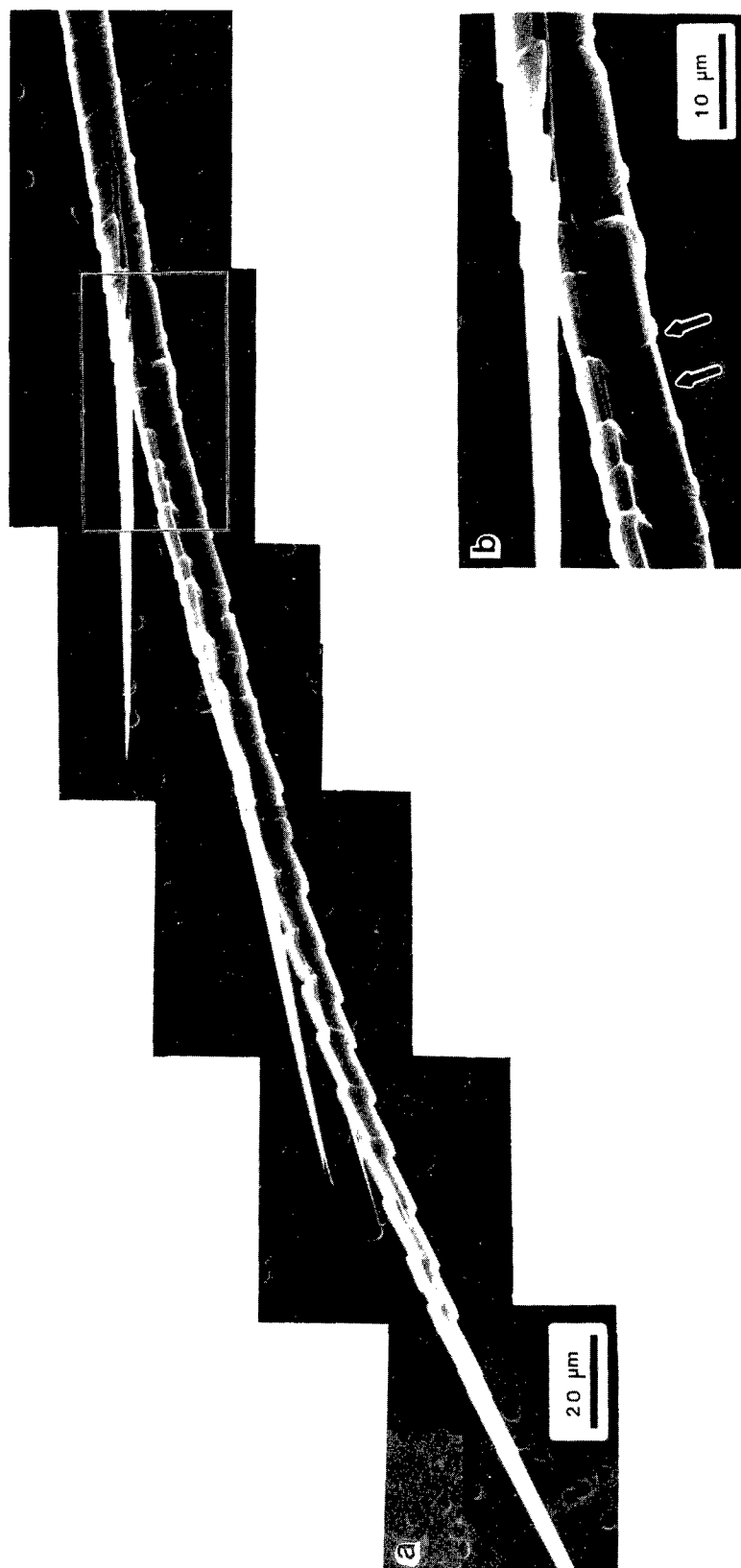


Figure 6.3

(a) SEM micrograph of tensile fracture surface of Kevlar 49 fiber after subsequent compression.
 (b) Enlargement of area outlined in (a). Arrows point to perpendicular bands on what appear to be radial planes.

splits which usually occur during tensile failure [33,43]. The compressive deformation which is superimposed on the split fiber is a striking combination of kinked and buckled regions. An enlargement of a section of the fiber near the area where the splitting initiated shows the internal deformation of the compressed fiber (Figure 6.3b). The inside of the fiber contains bands oriented perpendicular to the fiber axis on what appear to be radial planes. The splitting between radial planes during axial tensile failure is an expected consequence of the radial sheet morphology of Kevlar 49 fiber. Assuming that the compressive deformation of the intact fiber and the split fiber that has exposed internal surfaces are related, then the observations of perpendicular bands of buckled material on radial planes and of obliquely-oriented kink bands on tangential planes (i.e., the fiber surface) support the results obtained by Takahashi [37].

A photograph of an orthotropic wood block after compression is shown in Figure 6.4. The arrows in this figure point to a kink band oriented at approximately 45° to the grain (axial direction) on the tangential face and to a band of buckled material oriented perpendicular to the grain on the radial face. These particular orientations of deformation bands on the two material faces were observed for almost every specimen, except that kink bands formed at angles ranging from 40° to 60° with respect to the grain.

The first of two cylindrically orthotropic wood cylinders tested did indeed develop a helical kink band on its lateral surface during axial compression. Photographs of this specimen are shown in Figure

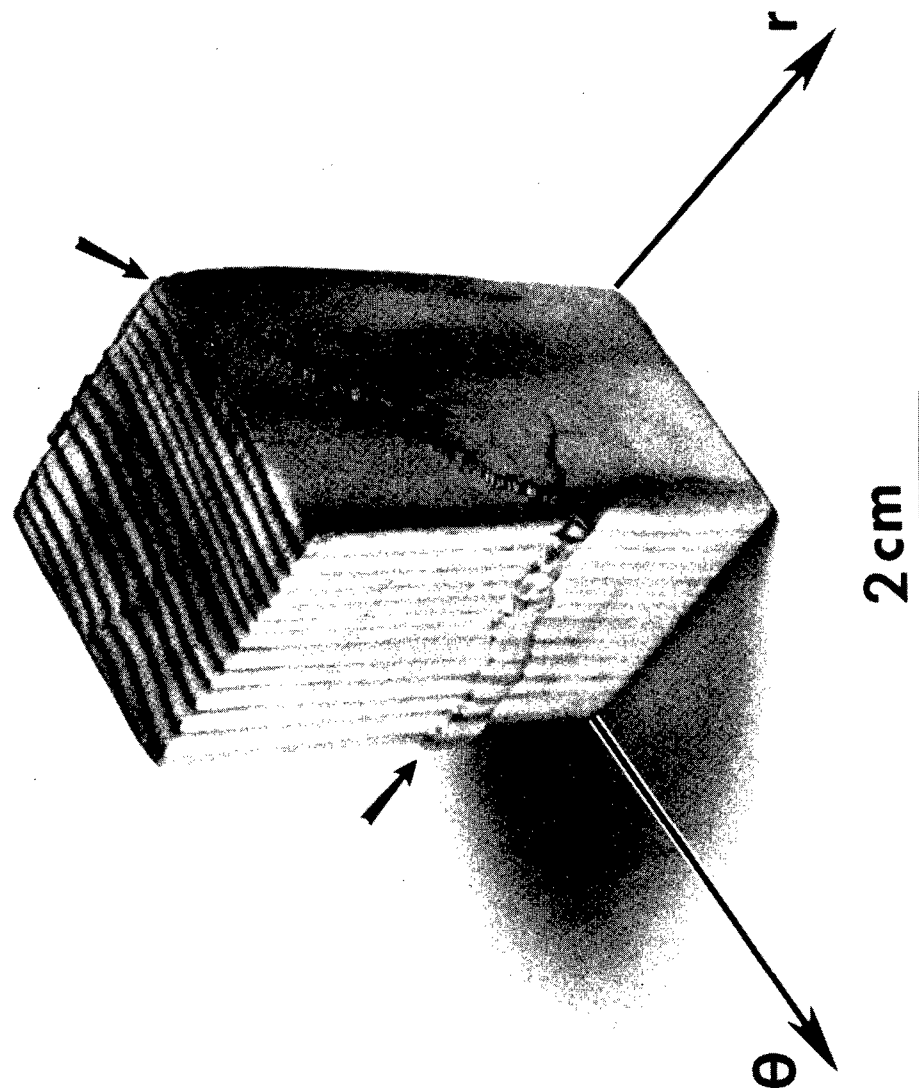


Figure 6.4

Orthotropic wood block after axial compression.

6.5. The left-handed helical band winds around the cylinder at an average angle of 60° to the grain. Note that the geometrical and structural centers of this wood cylinder coincide (Figure 6.5h). The axial splitting of this cylinder seen in some of the photographs of Figure 6.5 occurred long after the cylinder had been tested. These splits were presumably caused by shrinkage stresses which developed during drying of the specimen at ambient conditions after testing.

Results of simultaneous observations of helical band formation and force-displacement behavior for this first wood cylinder are summarized in Figure 6.6. In this specimen, the helical band initiated at one end of the cylinder and then propagated around the lateral surface. Both initiation and propagation of the band occurred within the strain-softening region of the force-displacement curve, after the maximum compressive force had been reached.

The second wood cylinder tested did not form complete helical kink bands under axial compression, but did form isolated kink bands oriented at approximately 60° to the grain on its lateral surface. A transverse section cut from this second cylinder through surface kink bands is shown in Figure 6.7. The sectioning reveals that surface kink bands are connected by internal radial deformation bands to the structural, and not the geometrical, center of the wood cylinder. This last observation is made clear by the distinct separation of the structural and geometrical centers of this particular cylinder.

It is also evident from Figure 6.7 that the internal radial deformation bands taper as they approach the core of the cylinder. Two such

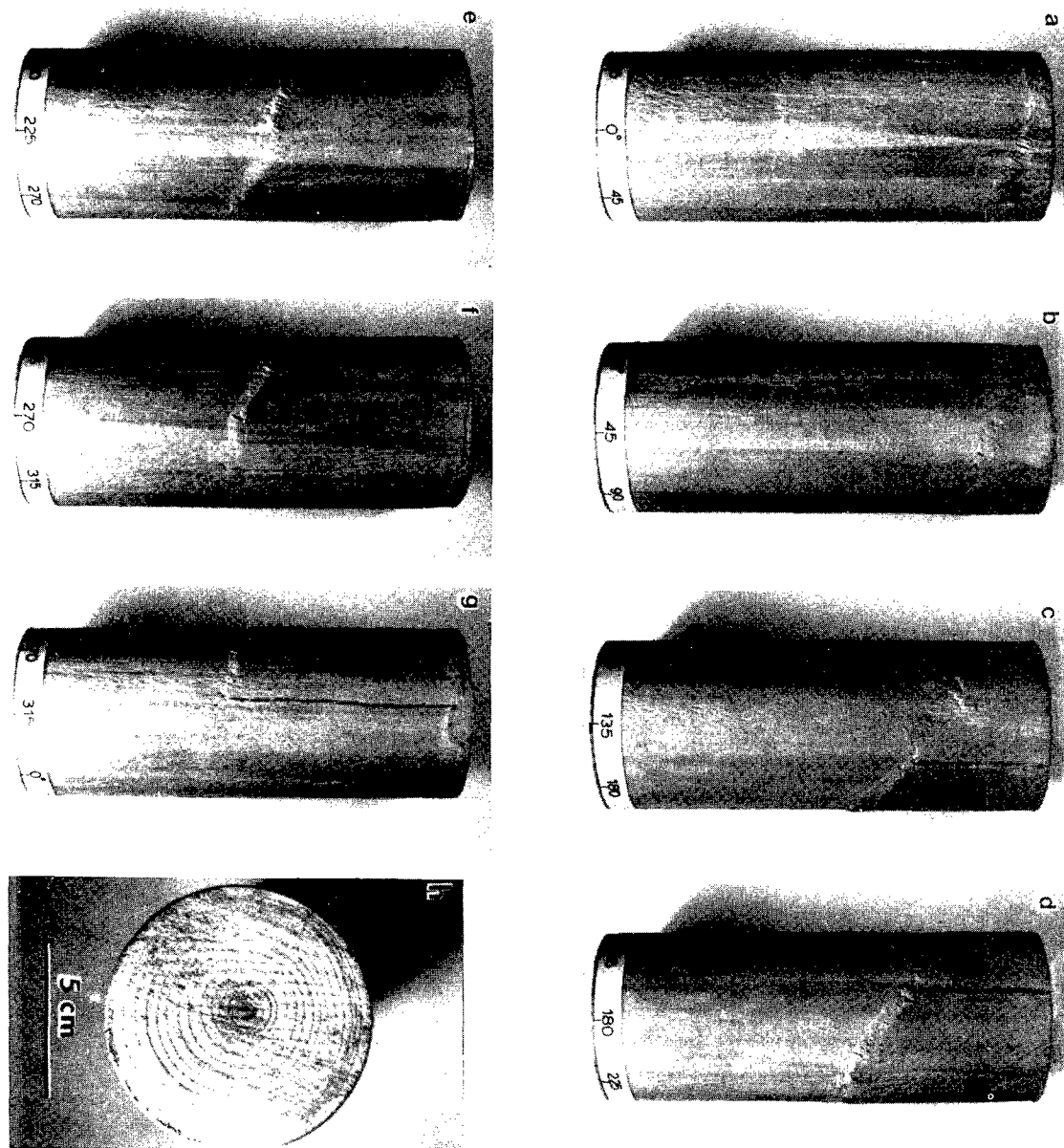
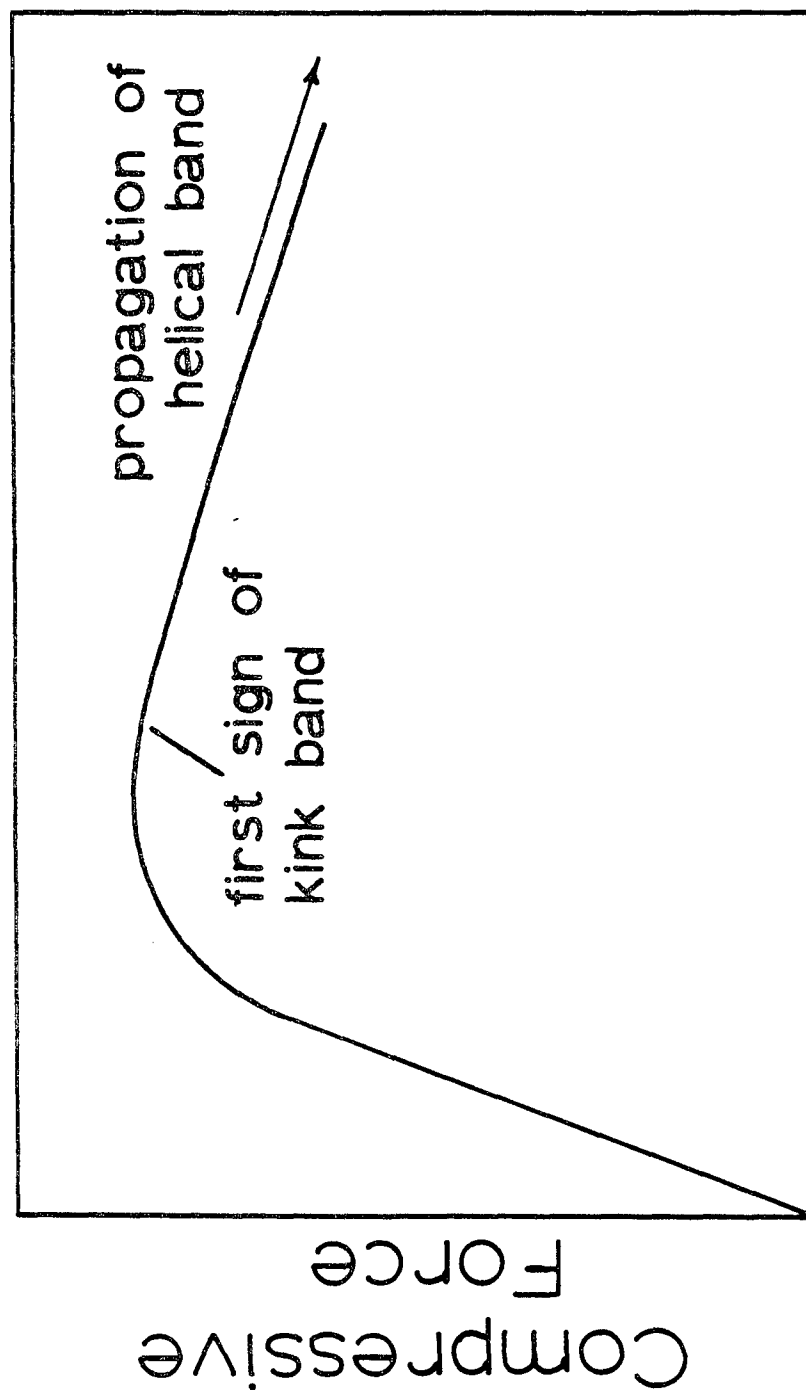


Figure 6.5

(a-g) Helical kink band in axially compressed wood cylinder. Each figure is a photograph taken after rotating the cylinder approximately 45°. (h) End view of cylinder shown in (a-g).



Displacement

Figure 6.6. Schematic of force displacement profile and corresponding stages of helical band formation for wood cylinder compression.

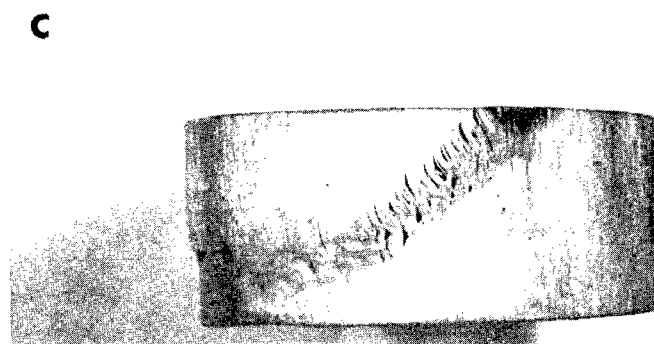
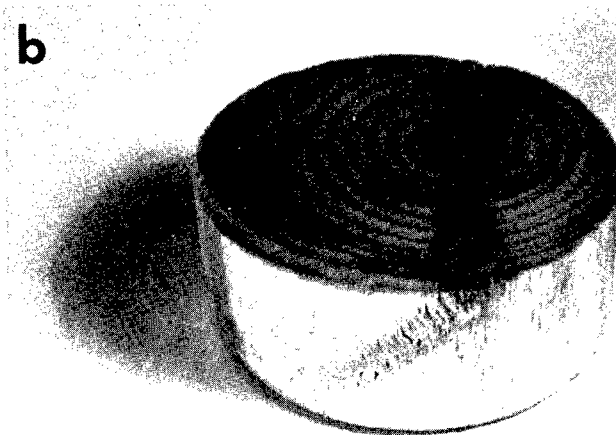
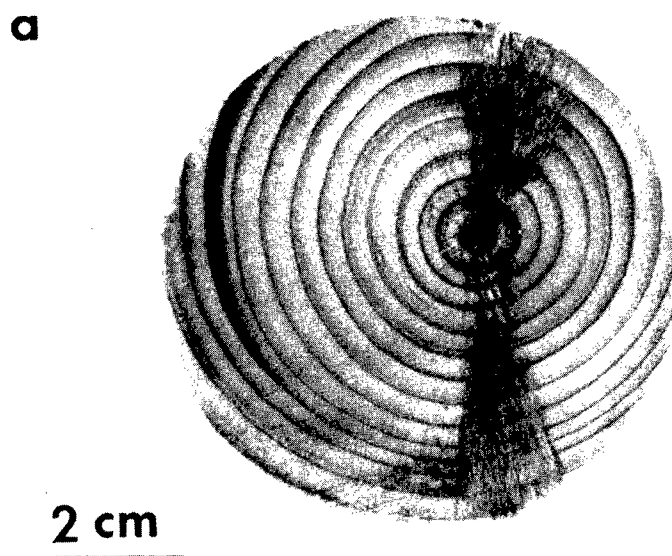


Figure 6.7

(a-c) Top and side views of a transverse section cut from a compressed wood cylinder that had two separate kink bands on its surface.

bands are seen in the section shown in this figure because the transverse cut was made through two isolated surface kink bands.

Other transverse sections through the second cylinder showed that the internal deformation band always connects the surface kink band to the structural core along radial directions, thereby forming a "spiral staircase" pattern of deformed material in the cylinder. The absence of complete helical kink bands on the surface of this cylinder may be related to the fact that its geometrical and structural centers do not coincide.

Comparison of the axial compressive deformation bands formed in the orthotropic wood blocks and the cylindrically orthotropic wood cylinders shows that radial planes buckle under compression, forming perpendicular bands, and that obliquely oriented kink bands form on tangential planes in both types of specimens. Therefore, it is apparent that the presence of free surfaces in wood blocks does not affect the orientations of compressive deformation bands relative to the orientations of corresponding bands in the wood cylinders.

6.5 Discussion

The evidence presented in this study shows that under axial compression, helical kink bands form by initiation and propagation on the surface of Kevlar 49 fibers and cylindrically orthotropic wood cylinders, and that radial bands of buckled material form within both materials. This similarity in compressive failure modes of two materials

which differ so greatly in both size and composition can be explained with the aid of the radial sheet model previously described.

When sheets of paper or rubber are stacked together and then compressed parallel to the plane of the sheets, kink bands oriented at oblique angles to the load axis form by initiation and propagation along the lateral face comprised of the edges of the sheets, and perpendicular bands (buckled sheets) form on the other lateral face [56,57]. This cooperative buckling of stacked sheets is illustrated in Figure 6.8.

Further examination of Figure 6.8 reveals that most of the deformation in the kink band is shearing between sheets. The deformation on the other lateral face consists of bending or buckling of the sheets at the boundaries of the perpendicular band. Therefore, kink bands form by shear slippage between buckled planes of easy shear slip.

Moreover, the angle between the kink band boundary and the axis of loading (β) is always less than 90° . This formation of obliquely-oriented kink bands has been explained in terms of volume changes [61]. Kink bands with perpendicular boundaries, i.e., $\beta=90^\circ$, can only be formed by imposing negative volume changes within the band and therefore the formation of such bands is considered highly unlikely.

When planes or sheets of easy shear slip are radially stacked to form an orthotropic cylinder and then compressed, the compressive failure should be internal buckling of the sheets in a cooperative manner to yield a helical kink band on the lateral surface of the cylinder. Therefore the failure pattern formed by kinked and buckled material will resemble a "spiral staircase." A schematic of this pattern is given in

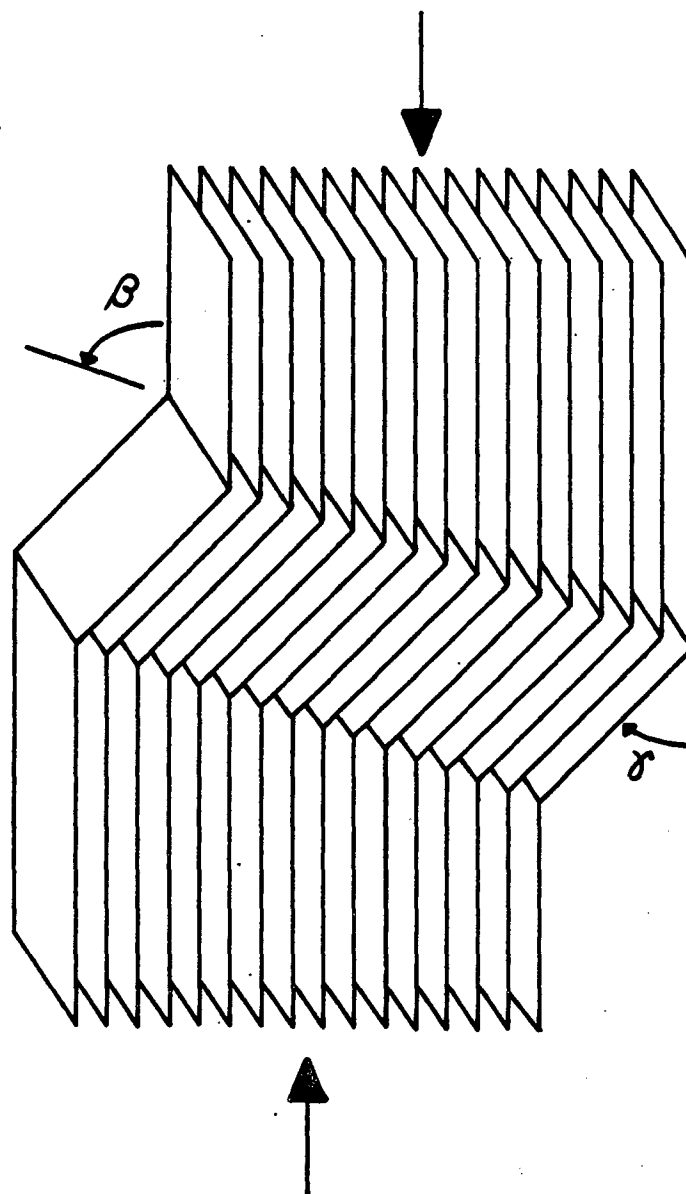


Figure 6.8. Illustration of a compressive kink band in stacked sheets.

Figure 6.9. Near the center of a cylinder composed of radial sheets, there is less room for lateral displacement than at the surface. This might explain the tapering of the internal deformation band in the compressed wood cylinder near its core (Figure 6.7).

There is little evidence for the internal buckling of the radial sheets of Kevlar 49 fiber in the optical micrograph in Figure 2.4. However, there is proof of the presence of perpendicular bands on free radial surfaces exposed by tensile fracture (Figure 6.3). Furthermore, Takahashi showed that perpendicular bands form within radial sections of compressively kinked Kevlar 29 fibers [37]. These observations may also be explained by the constraint imposed on lateral displacements near the center of the intact fiber. The extent of internal deformation due to buckling of radial planes close to the fiber core may be too small to be detected by transmitted visible light.

6.6 Conclusions

The results of this study can be summarized as follows:

1. The formation of compressive kink bands within particular planes of orthotropic materials results from shearing between the buckled planes (not necessarily crystallographic planes) of easy shear slip. This mechanism of compressive failure may be universal for orthotropic materials which are compressed parallel to planes of easy shear slip.
2. Helical kink bands in axially compressed Kevlar 49 fibers and wood cylinders result from the particular cylindrically orthotropic

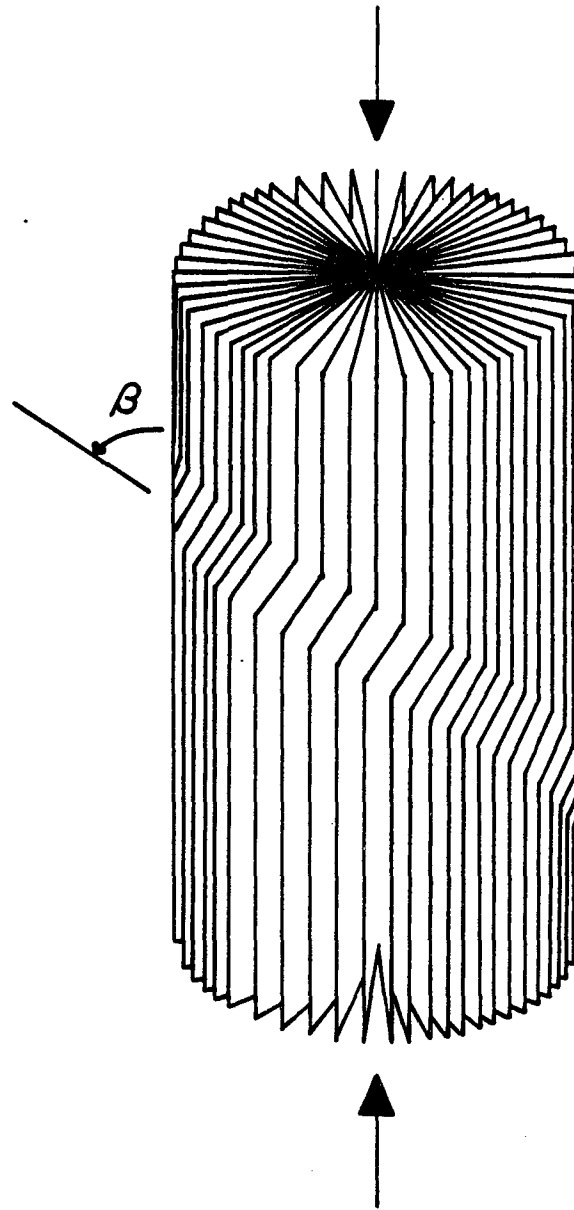


Figure 6.9. Illustration of a helical compressive kink band in a cylinder composed of radially oriented stacked sheets.

symmetry exhibited by these materials. Such band formation can be explained by the cooperative buckling of radial material planes.

3. Other cylindrically orthotropic materials which have the same mechanical anisotropy exhibited by wood and Kevlar fibers should also form helical bands under axial compression. Axial compression of cylindrically orthotropic materials composed of tangential material planes or sheets, such as "onionskin" graphite fibers, should provide interesting comparison to the results presented herein.

CHAPTER VII

FUTURE WORK

In this dissertation, it has been established that the axial compressive failure of high performance organic fibers is due to the onset of microbuckling instability. The compressive strength of these fibers is predicted to be equal to the minimum fiber longitudinal shear modulus. This prediction was obtained from both a linear elastic microbuckling analysis (Chapter III) and from an analysis of an observed second-order effect of axial tensile stress on the torsion modulus of high performance polymer fibers (Chapter V). Experimentally determined fiber compressive strength was found to be equal to approximately one-third of the torsion modulus.

Future studies should include measurements of axial compressive strengths and longitudinal shear moduli of other high performance organic fibers, especially fibers based on extended-chain polymers. These measurements are needed to establish the applicability of the linear relationship between compressive strength and longitudinal shear modulus and, therefore, the proposal that compressive strengths are limited by elastic instability. The current research efforts in the field of thermotropic polymer liquid crystals should make a variety of high performance materials available in the near future.

The only chain-extended flexible polymer fiber examined in this thesis, i.e., the gel-spun PE fiber, did not exhibit the same correlation between axial compressive and torsion modulus that was observed for

the rigid-rod polymer fibers. If PE fiber is an orthotropic material, the torsion modulus may not be the minimum longitudinal shear modulus of this fiber. It would be interesting to measure the torsion modulus of PE fibers having both a uniform cross-section and a structural symmetry that yields a torsion modulus equal to the minimum longitudinal shear modulus of PE. Such fibers could also be used to determine the dependence of torsion modulus on axial tensile stress, which was not determined in this thesis because of the limitations imposed on the experimental accuracy by the irregular and non-uniform cross-section of those PE fibers examined here.

If the axial compressive strength of rigid-rod polymers is truly limited by the onset of elastic microbuckling instability, then changes in compressive strength due, for example, to temperature changes, introduction of a plasticizer or heat-treatment should parallel changes in longitudinal shear modulus due to these same factors. Furthermore, because no buckling deformation occurs in perfectly oriented fibers compressed to stresses below the critical value, compressive fatigue of fibers or their composites below the critical compressive stress should not result in material failure no matter how many loading cycles are applied. Compressive fatigue tests of single fibers (via the beam bending technique described in Chapter II) or fiber composites should be performed to test this hypothesis.

Compressive failure with concomitant kink band formation due to compression along planes of easy shear slip occurs in several anisotropic materials. The stress required to initiate kink bands (i.e., the

compressive strength) in rigid-rod polymer fibers and some types of fiber-reinforced composites [97] appears to be limited by elastic microbuckling instability. It would be interesting to examine the compressive strength-shear modulus relationship for materials such as wood and metal single crystals and thereby determine if the elastic microbuckling mechanism for compressive failure is universal for anisotropic materials that form compressive kink bands.

The ratio of measured compressive strength to torsion modulus for rigid-rod polymer fibers is approximately one-third, indicating that the estimate of compressive strength given by the torsion modulus is consistently too high. One explanation discussed in Chapter IV for this disparity is that there may be regions within the fiber, such as interfibrillar regions, which exhibit a shear modulus that is lower than the torsion modulus. It was proposed that microbuckling should be initiated at a compressive stress equal to this lower local shear modulus.

However, if high performance fibers are actually composites of fibrils, microfibrils and "binder," then the stress required to initiate microbuckling in these fibers should be equal to the "composite" longitudinal shear modulus. Both Rosen [20] and Foye [92] considered the onset of elastic shear instabilities in fiber-reinforced composites where both the matrix and fiber undergo shear deformations. Although the approach taken by each worker to predict the critical compressive stress differed, both concluded that elastic instability is initiated at a stress equal to:

$$\sigma_c = \frac{G_m}{(1-V_f) + V_f(G_m/G_f)} \quad (7.1)$$

where: m = matrix

f = fiber

G_i = longitudinal shear moduli

V_f = volume fraction of fiber

This equation is the Reuss estimate of the longitudinal shear modulus G_R of a composite material. It is obtained by assuming the stresses in each phase (fiber and matrix) are equivalent. This estimate represents a lower bound for the actual longitudinal shear modulus of a composite.

An upper bound estimate for composite shear modulus is given by the Voigt modulus G_V , which is obtained by assuming the strains in each phase are identical. This shear modulus is given by:

$$G_V = V_f G_f + (1-V_f) G_m \quad (7.2)$$

The actual shear modulus of any composite should fall within the range bounded by G_R and G_V . Two different shear moduli $G_{xy} \neq G_{yx}$ may be obtained from complimentary measurements of shear deformation of a composite laminate as shown in Figure 7.1. The deformation shown in Figure 7.1a corresponds to equivalent shear strains γ_{yx} in each phase of the composite and is therefore characterized by a Voigt modulus G_V . This modulus is obtained when a strain γ_{yx} is applied and a stress τ_{yx} , an average of the shear stresses in each phase, is measured.

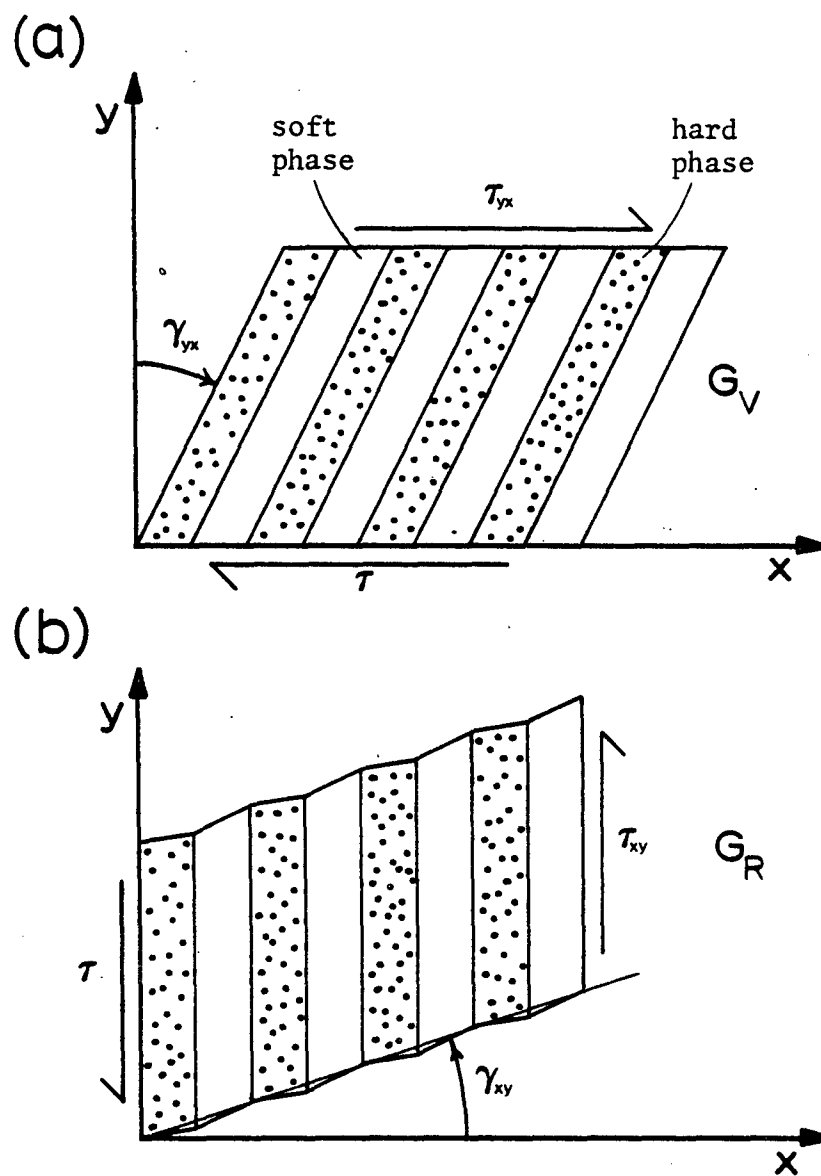


Figure 7.1. Simple shear deformation of a laminate.
 (a) Shear strain in each phase equal.
 (b) Shear stress in each phase equal.

The deformation shown in Figure 7.1b corresponds to equivalent shear stresses τ_{xy} in each phase and is therefore governed by a Reuss modulus G_R . This modulus is determined by applying a shear stress τ_{xy} and measuring a shear strain γ_{xy} that is an average of the shear strains in each phase.

The condition $G_{xy} \neq G_{yx}$ violates linear elasticity theory, but may apply to anisotropic materials composed of two or more distinct phases. If the anisotropy and heterogeneity of the high performance organic fibers are severe, then the torsion modulus of these fibers would correspond to the modulus $G_{yx} = G_V$ obtained from the deformation depicted in Figure 7.1a. This shear modulus is always greater than $G_{xy} = G_R$, and therefore the Reuss modulus should be used as the estimate of the compressive strength. Experiments should be performed on single fibers or fiber composites to determine if the deformations shown in Figure 7.1 do indeed yield different values of longitudinal shear moduli. If a disparity exists, it could explain the overestimate of compressive strength which is given by the torsion modulus.

The prediction that compressive strength is equal to the longitudinal shear modulus was obtained by a linear elastic microbuckling analysis (Chapter III) and by an analysis of the effect that axial stresses have on fiber torsion modulus (Chapter V). The axial stress-torsion modulus relationship is a result of nonlinear-elastic behavior. The magnitude of this nonlinear effect suggests that a refinement of the microbuckling analysis, which would incorporate nonlinear-elastic behavior, might yield better estimates of compressive strength. For example,

calculations of shear mode buckling stresses could be made assuming the foundation shear modulus is a function of shear strain or compressive stress. Reductions in the true shear modulus of fiber-reinforced composites due to compressive stresses have been measured [94]:

Several experiments could be performed on hollow fibers, which would further our knowledge of compressive characteristics of high performance organic fibers. First, the compressive strength of hollow fibers can be measured directly [98], thereby eliminating the need to resort to an indirect measurement of strength from critical strains to kink band formation. Second, measurements of torsion modulus versus axial tensile stress for hollow fibers and comparison to the results obtained for solid fibers of the same material should provide an assessment of the resistance of the fibers to length and radius changes with torsion. Third, hollow fibers can be measured for compressive strength as a function of twist without the complicating effects of axial normal stresses that develop with twist in solid fibers. This experiment would determine conclusively whether compressive failure occurs by elastic instability as demonstrated here, or by shear failure as proposed by Argon [62].

Further insight into kink band formation and the stresses required to initiate kink banding could be obtained from tests on model anisotropic materials. This work would be an extension of the studies of compressive behavior of card decks [56] and rubber laminates [57]. For future experiments, sheets of paper could be glued together with matrices having different shear moduli. These laminates could be

measured for composite shear modulus to determine if $G_{xy} \neq G_{yx}$ as discussed above. The compressive stress required to initiate kink banding in these models could be compared to measured and calculated composite shear moduli. The effect of defects on the nucleation of kink bands could be studied by deliberately incorporating voids, regions of misalignment or short lengths of paper (i.e., line defects) into the model laminate.

The goals outlined at the onset of this dissertation included the possibility of suggesting ways to improve the compressive strength of high performance organic fibers. It is clear from the work performed in this dissertation that improvements in compressive strength will follow from increases in longitudinal shear modulus. Again it is emphasized that the shear modulus and not the shear strength of the fiber determines its compressive strength. It is, perhaps, fortunate that a modulus is an average property of a material, less affected by local irregularities and defects than a material strength. Therefore, it is probably easier to improve a material stiffness than a strength.

Conceivably, the lateral interaction between polymer chains (i.e., the shear modulus) could be enhanced via stronger bonding between chains. These bonds might be strong secondary bonds such as hydrogen bonds or chemical crosslinks formed by covalent or ionic bonds. These strong lateral bonds must act in at least two directions within the cross-section of the fiber. Strong lateral bonds in only one direction, as in the case of radially oriented hydrogen bonds in PPTA fibers, still leave planes of easy shear slip that enable microbuckling to occur at

relatively low compressive stresses. An example of an extended polymer chain that forms a crystalline unit cell with hydrogen bonds oriented in at least two lateral directions is cellulose [95]. It would be interesting to measure the axial compressive strengths of highly oriented cellulose fibers.

Enhancement of crystalline perfection may be a route to higher shear modulus material. However, it is also possible that a perfect crystal might have a lower shear modulus than an imperfect crystal. This would be true for crystals containing pinned dislocations that offer more resistance to shear deformation. Theoretical calculations of shear modulus may provide an estimate of the upper limit on compressive strength that may be attained via crystalline perfection.

If a polymer fiber is an inhomogeneous material composed of microfibrils, fibrils and binder, then the shear modulus (and hence the compressive strength) is a function of the shear moduli of all these phases. It is readily verified from (7.1) that the estimate of composite shear modulus is dominated by the modulus of the soft matrix phase. Therefore, improvements in the shear modulus of the binding phase between microfibrils would yield significant improvements in composite shear modulus and possibly compressive strength.

REFERENCES

1. W.B. Black, "High Modulus/High Strength Organic Fibers," *Ann. Rev. Mater. Sci.*, 10, 311 (1980).
2. W.B. Black, "Stiff-Chain Aromatic Polymer Solutions, Melts and Fibers," in Flow-Induced Crystallization, R.L. Miller, ed., Gordon and Breach, New York (1979).
3. R.J. Diefendorf and E. Tokarsky, "High Performance Carbon Fibers," *Polym. Eng. Sci.*, 15(3), 150 (1975).
4. W.N. Reynolds, "Structure and Physical Properties of Carbon Fibers," in Chemistry and Physics of Carbon, P.L. Walker, Jr. and P.A. Thrower, eds., vol. 11, p. 2, Marcel Dekker, New York (1973).
5. H. Blades, U.S. Patent 3,869,430, "High Modulus, High Tenacity Poly (p-Phenylene Terephthalamide) Fiber," assigned to E.I. DuPont de Nemours & Co. (1975).
6. G.C. Alfonso, E. Bianchi, A. Ciferri, S. Russo, F. Salaris, and B. Valenti, "Ultrahigh-Modulus Fibers From Rigid and Semirigid Aromatic Polyamides," *J. Polym. Sci.: Polym. Symp.* 65, 213 (1978).
7. W.B. Black, J. Preston, H.S. Morgan, G. Raumann, and M.R. Lilyquist, "Some Physical and Mechanical Properties of Some High-Modulus Fibers Prepared From All-Para Aromatic Polyamide-Hydrazides," *J. Macromol. Sci.-Chem.*, A7(1), 137 (1973).
8. T.E. Helminiak, "The Air Force Ordered Polymers Research Program: An Overview," *ACS Org. Coat. and Plast. Preprints*, 4, 475 (1979).
9. H.F. Kuhfuss and W.J. Jackson, U.S. Patent 3,804,805, assigned to Eastman Kodak Co. (1974).
10. P.W. Morgan, U.S. Patent 4,048,148, assigned to E.I. DuPont de Nemours & Co. (1977).
11. G.W. Calundann, U.S. Patents 4,067,852 (1978), 4,185,996 (1980), 4,161,470 (1979), and 4,256,624 (1981), assigned to Celanese Co.
12. I.M. Ward, "Developments in Oriented Polymers--I," I.M. Ward, ed., Chapt. 5, *Appl. Sci. Pub., Ltd., London* (1982).
13. P. Smith and P. Lemstra, "Ultra-High-Strength Polyethylene Filaments By Solution Spinning/Drawing," *J. Mater. Sci.*, 15(2), 505 (1980).

14. W.T. Mead, C.R. Desper and R.S. Porter, "Physical and Mechanical Properties of Ultra-Oriented High-Density Polyethylene Fibers," J. Polym. Sci.: Polym. Phys. Ed., 17(5), 859 (1979).
15. G. Capaccio, A.G. Gibson and I.M. Ward, Ultra-High Modulus Polymers, A. Ciferri and I.M. Ward, eds., Chapt. 7, Appl. Sci. Pub., Ltd., London (1979).
16. Chemical and Engineering News, p. 37, February 20 (1984).
17. R.E. Wilfong and J. Zimmerman, "Strength and Durability Characteristics of Kevlar Aramid Fiber," J. Appl. Polym. Sci., Appl. Polym. Symp. 31, 1 (1977).
18. N.L. Hancox, ed., Fibre Composite Hybrid Materials, MacMillan, New York (1981).
19. S.R. Allen, Mechanical and Morphological Correlations in Poly (p-Phenylene Benzobisthiazole) Fibers, Ph.D. Thesis, University of Massachusetts, Amherst, 1983.
20. S.V. Kulkarni, J.S. Rice and B.W. Rosen, "An Investigation of the Compressive Strength of Kevlar 49/Epoxy Composites," Composites, 6(5), 217 (1975).
21. M.G. Dobb, D.J. Johnson, and B.P. Saville, "Compressional Behavior of Kevlar Fibres," Polymer, 22(7), 960 (1981).
22. J.M. Greenwood and P.G. Rose, "Compressive Behavior of Kevlar 49 Fibres and Composites," J. Mater. Sci., 9(11), 1809 (1974).
23. M.G. Northolt and J.J. Van Aartsen, "Chain Orientation Distribution and Elastic Properties of Poly (p-Phenylene Terephthalamide), A 'Rigid-Rod' Polymer," J. Polym. Sci.: Polym. Symp. 58, 283 (1977).
24. F. Druschke, H.W. Siesler, G. Spilgies, and H. Tengler, "Molecular Order and Orientation in Aromatic Polyamide Fibers by Internal Reflection Spectroscopy and Wide Angle X-ray Diffraction," Polym. Eng. Sci., 17(2), 93 (1977).
25. K. Tashiro, M. Kobayashi, and H. Tadokoro, "Elastic Moduli and Molecular Structures of Several Crystalline Polymers, Including Aromatic Polyamides," Macromol., 10(2), 413 (1977).
26. M.G. Northolt, "Tensile Deformation of Poly (p-Phenylene Terephthamide) Fibres, An Experimental and Theoretical Analysis," Polymer, 21(10), 1199 (1980).

27. M. Panar, P. Avakian, R.C. Blume, K.H. Gardner, T.D. Gierke and H.H. Yang, "Morphology of Poly (p-Phenylene Terephthalamide) Fibers," J. Polym. Sci.: Polym. Phys. Ed., 21(10), 1955 (1983).
28. M.G. Dobb, D.J. Johnson and B.P. Saville, "Supramolecular Structure of a High-Modulus Polyaromatic Fiber (Kevlar 49)," J. Polym. Sci.: Polym. Phys. Ed., 15(12), 2201 (1977).
29. R. Hagege, M. Jarrin and M.J. Sotton, "Direct Evidence of Radial and Tangential Morphology of High-Modulus Aromatic Polyamide Fibers," J. Microsc. O., 115, 65 (1979).
30. S.B. Warner, "On the Radial Structure of Kevlar," Macromol., 16(9), 1546 (1983).
31. M.G. Dobb, D.J. Johnson and B.P. Saville, "Direct Observation of Structure in High-Modulus Aromatic Fibers," J. Polym. Sci.: Polym. Symp. 58, 237 (1977).
32. S.C. Simmens and J.W.S. Hearle, "Observation of Bands in High-Modulus Aramid Fibers by Polarization Microscopy," J. Polym. Sci.: Polym. Phys. Ed., 18(4), 871 (1980).
33. R.J. Morgan, C.O. Pruneda and W.J. Steele, "The Relationship Between the Physical Structure and the Microscopic Deformation and Failure Processes of Poly (p-Phenylene Terephthalamide) Fibers," J. Polym. Sci.: Polym. Phys. Ed., 21(9), 1757 (1983).
34. L.-S. Li., L.F. Allard and W.C. Bigelow, "On the Morphology of Aromatic Polyamide Fibers (Kevlar, Kevlar 49 and PRD-49)," J. Macromol. Sci.-Phys., B22(2), 269 (1983).
35. M.G. Dobb, D.J. Johnson, A. Majeed and B.P. Saville, "Microvoids in Aramid-Type Fibrous Polymers," Polymer 20(10), 1284 (1979).
36. M.M. Schoppee and J. Skelton, "Bending Limits of Some High-Modulus Fibers," Tex. Res. J., 44(12), 968 (1974).
37. T. Takahashi, M. Miura and K. Sakurai, "Deformation Band Studies of Axially Compressed Poly (p-Phenylene Terephthalamide) Fiber," J. Appl. Polym. Sci., 28(2), 579 (1983).
38. W.C. Dale and E. Baer, "Fibre-Buckling in Composite Systems: A Model for the Ultrastructure of Uncalcified Collagen Tissues," J. Mater. Sci., 9(3), 369 (1974).
39. F.J. McGarry, Trans. Inst. Chem. Eng., 182, CE 236 (1964).
40. J.K. Gillham, P.N. Reitz and M.J. Doyle, "Spiral and Helical Fractures," Polym. Eng. Sci., 8(3), 227 (1968).

41. H.M. Hawthorne and E. Teghtsoonian, "Axial Compression Fracture in Carbon Fibers," J. Mater. Sci., 10(1), 41 (1975).
42. B.W. Rosen, "Mechanics of Composite Strengthening," A.S.M. Seminar, Philadelphia (October 1964).
43. L. Konopasek and J.W.S. Hearle, "The Tensile Fatigue Behavior of Para-Oriented Aramid Fibers and Their Fracture Morphology," J. Appl. Polym. Sci., 21(10), 2791 (1977).
44. J. Frenkel, Z. Phys., 37, 572 (1926).
45. E. Orowan, Rep. Prog. Phys., 12, 185 (1949).
46. C.A. Coulomb, Mém. Math. et Phys., 7, 343 (1773).
47. E. Orowan, "Type of Plastic Deformation New in Metals," Nature, 149, 643 (1942).
48. D.A. Zaukelias, "Observation of Slip in Nylon 66 and 610 and Its Interpretation in Terms of a New Model," J. Appl. Phys., 33(9), 2797 (1962).
49. M. Takayanagi and T. Kajiyama, "Structural Factors in Deformation of Crystalline Polymers," J. Macromol. Sci.-Phys., B8(1-2), 1 (1973).
50. K. Shigematsu, K. Imada and M. Takayanagi, "Formation of Kink Bands by Compression of the Extrudate of Solid Linear Polyethylene," J. Polym. Sci.: Polym. Phys. Ed., 13(1), 73 (1975).
51. P.B. Bowden and R.J. Young, "Review: Deformation Mechanisms in Crystalline Polymers," J. Mater. Sci., 9(12), 2034 (1974).
52. G.E. Attenburrow and D.C. Bassett, "Compliances and Failure Modes of Oriented Chain-Extended Polyethylene," J. Mater. Sci., 14(11), 2679 (1979).
53. M.E. Desch and J.M. Dinwoodie, Timber: Its Structure, Properties and Utilization, Timber Press, Forest Grove, Oregon (1981).
54. C.T. Keith, "The Anatomy of Compression Failure in Relation to Creep-Inducing Stresses," Wood Sci., 4(2), 71 (1971).
55. M.S. Paterson and L.E. Weiss, "Experimental Deformation and Folding in Phyllite," Geol. Soc. Am. Bull., 77, 343 (1966).
56. N.C. Gay and L.E. Weiss, "The Relationship Between Principal Stress Directions and the Geometry of Kinks in Foliated Rocks," Tectonophysics, 21(3), 287 (1974).

57. E. Honea and A.M. Johnson, "A Theory of Concentric, Kink and Sinusoidal Folding and of Monoclinical Flexuring of Compressible, Elastic Multilayers," *Tectonophysics*, 30 (3-4), 197 (1976).
58. C.A. Berg and M. Salama, "Fatigue of Graphite Fibre-Reinforced Epoxy in Compression," *Fibre Sci. Tech.*, 6(2), 79 (1973).
59. C.W. Weaver and J.G. Williams, "Deformation of a Carbon-Epoxy Composite Under Hydrostatic Pressure," *J. Mater. Sci.*, 10(8), 1323 (1975).
60. N.L. Hancox, "The Compression Strength of Unidirectional Carbon Fibre Reinforced Plastic," *J. Mater. Sci.*, 10(2), 234 (1975).
61. C.R. Chaplin, "Compressive Fracture in Unidirectional Glass-Reinforced Plastics," *J. Mater. Sci.*, 12(2), 347 (1977).
62. A.S. Argon, *Treatise on Materials Science and Technology*, H. Herman, ed., Vol. 1, p. 79, Academic Press, New York (1972).
63. A.G. Evans and W.F. Adler, "Kinking As a Mode of Structural Degradation in Carbon Fiber Composites," *Acta Metallurgica*, 26(5), 725 (1978).
64. L.E. Weiss, "Nucleation and Growth of Kink Bands," *Tectonophysics*, 65(1-2), 1 (1980).
65. R.E. Robertson, "Formation of Kink Bands in Oriented Polymers," *J. Polym. Sci.: Part A-2*, 7(8), 1315 (1969).
66. H. Mark, *Trans. Faraday Soc.*, 32, 144 (1936).
67. J.P. Hummel and P.J. Flory, "Structural Geometry and Torsional Potentials in p-Phenylene Polyamides and Polyesters," *Macromol.*, 13(3), 479 (1980).
68. S.P. Timoshenko and J.M. Gere, *Theory of Elastic Stability*, McGraw-Hill, New York (1961).
69. H. Schuerch, "Prediction of Compressive Strength in Uniaxial Boron Fiber-Metal Matrix Composite Materials," *AIAA J.*, 4(1), 102 (1966).
70. L.B. Greszczuk, "Microbuckling Failure of Circular Fiber-Reinforced Composites," *AIAA J.*, 13(10), 1311 (1975).
71. W.R. Jones and J.W. Johnson, "Intrinsic Strength and Non-Hookean Behavior of Carbon Fibers," *Carbon*, 9(5), 645 (1971).

72. A.J. Perry, B. Ineichen and B. Eliasson, "Fibre Diameter Measurement by Laser Diffraction," J. Mater. Sci., Letters, 9(8), 1376 (1974).
73. ASTM D3379-75e, "Standard Test Method for Tensile Strength and Young's Modulus of High-Modulus Single-Filament Materials," ASTM, Philadelphia (1975).
74. W.H. Gloor, "Torsional Testing of Fine Filaments, Part I: Apparatus and Procedures," Air Force Technical Report, AFML-TR-72-65 Part I (1972).
75. J.F. Mammone and W.C. Uy, "Exploratory Development of High Strength, High Modulus Polybenzothiazole Fibers. Part II: Fiberization Scale-Up and Optimization," Air Force Technical Report, AFML-TR-82-4154 (1984).
76. E.J. Seldin and C.W. Nezbeda, "Elastic Constants and Electron-Microscope Observations of Neutron-Irradiated Compression-Annealed Pyrolytic and Single-Crystal Graphite," J. Appl. Phys., 41(8), 3389 (1970).
77. D.W. Hadley, P.R. Pinnock and I.M. Ward, "Anisotropy in Oriented Fibres from Synthetic Polymers," J. Mater. Sci., 4, 152 (1969).
78. S.L. Phoenix and J. Skelton, "Transverse Compressive Moduli and Yield Behavior of Some Orthotropic, High-Modulus Filaments," Tex. Res. J., 44(12), 934 (1974).
79. R.G. Snyder and G. Zerbi, "Vibrational Analysis of Ten Simple Aliphatic Ethers: Spectra, Assignments, Valence Force Field and Molecular Conformations," Spectrochimica Acta, 23A(2), 391 (1967).
80. E.J. Roche, T. Takahashi and E.L. Thomas, "Structure of High Modulus Fibers of Poly (p-Phenylene Benzobisthiazole), Am. Chem. Soc. Symp., Fiber Diffraction Methods, 141, 303 (1980).
81. C.W. Bunn, "The Crystal Structure of Long-Chain Normal Paraffin Hydrocarbons," Trans. Faraday Soc., 35, 482 (1939).
82. A. Kelly, Strong Solids, Oxford University, London (1966).
83. R. Bacon, "Carbon Fibers From Rayon Precursors," in Chemistry and Physics of Carbon, P.L. Walker, Jr. and P.A. Thrower, eds., Vol. 9, p. 80, Marcel Dekker, New York (1973).
84. J.-B. Donnet and R.C. Bansal, Carbon Fibers, p. 171, Marcel Dekker, New York (1984).

85. K. Chen, C.W. LeMaistre, J.H. Wang and R.J. Diefendorf, "The Consequences of Residual Stress in High Modulus Carbon Fibers on Composite Performance," 182nd Nat. Conf., ACS, New York, Poly 137, August 1981.
86. S. Timoshenko, Strength of Materials: Part II, p. 286, D. Van Nostrand, Princeton, New Jersey (1956).
87. J.H. Poynting, "On the Changes in the Dimensions of a Steel Wire When Twisted and on the Pressure of Distortional Waves in Steel," Proc. Roy. Soc., A86 (590), 534 (1912).
88. A. Foux, "An Experimental Investigation of the Poynting Effect," in Second-Order Effects in Elasticity, Plasticity and Fluid Dynamics, M. Reiner and D. Abir, eds., p. 228, Pergamon, Oxford (1964).
89. R.S. Rivlin, "Torsion of a Rubber Cylinder," J. Appl. Phys., 18(5), 444 (1947).
90. F.D. Murnaghan, Finite Deformation of an Elastic Solid, John Wiley and Sons, New York (1951).
91. R.W. Dent and J.W.S. Hearle, "The Tensile Properties of Twisted Single Fibers," Tex. Res. J., 30(11), 805 (1960).
92. R.L. Foye, "Compression Strength of Unidirectional Composites," AIAA Paper No. 66-143, 3rd Aerospace Sciences Meeting, New York, January (1966).
93. S. Timoshenko, Strength of Materials: Part I, p. 281, Robert E. Krieger, Huntington, New York (1976).
94. J.G. Davis, Jr., Compressive Strength of Lamina-Reinforced and Fiber-Reinforced Composite Materials, Ph.D. Thesis, Virginia Polytechnic Institute and State University, Blacksburg (1973).
95. J. Bodig and B.A. Jayne, Mechanics of Wood and Wood Composites, Van Nostrand Reinhold, New York (1982).
96. T.L. Wilkinson, "Strength Evaluation of Round Timber Piles," U.S.D.A. Forest Service Research Paper FP1 101, Forests Products Laboratory, Madison, Wisc., December (1968).
97. J.R. Lager and R.R. June, "Compressive Strength of Boron-Epoxy Composites," J. Comp. Mater., 3, 48 (1969).
98. R.J. Farris, Polymer Science & Engineering Dept., University of Massachusetts, Amherst, private communication.

APPENDIX I
CRITICAL BUCKLING LOAD FOR A LINK-HINGE CHAIN
WITH THREE HINGES (p=4)

Examination of Figure A1.1 shows that the strain energies for hinges 1, 2 and 3 are:

$$\begin{aligned} U_1 &= \frac{k}{2} (\alpha_1 - \alpha_2)^2 \\ U_2 &= \frac{k}{2} (2\alpha_2)^2 \\ U_3 &= \frac{k}{2} (\alpha_1 - \alpha_2)^2 \end{aligned} \tag{A1.1}$$

and the total strain energy is therefore:

$$U = \sum_{i=1}^3 U_i = k(\alpha_1 - \alpha_2)^2 + \frac{k}{2} (2\alpha_2)^2 \tag{A1.2}$$

The total axial displacement is given by:

$$\Delta l = 2l(1 - \cos\alpha_1) + 2l(1 - \cos\alpha_2) \tag{A1.3}$$

which, for small α_i , can be approximated by:

$$\Delta l \approx 2l\left(\frac{\alpha_1^2}{2}\right) + 2l\left(\frac{\alpha_2^2}{2}\right) \tag{A1.4}$$

The work due to load P is then:

$$W = P\Delta l = Pl(\alpha_1^2 + \alpha_2^2) \tag{A1.5}$$

The total potential is defined by (3.4), which for this problem is:

$$V = (k - Pl)\alpha_1^2 + (3k - Pl)\alpha_2^2 - 2k\alpha_1\alpha_2 \tag{A1.6}$$

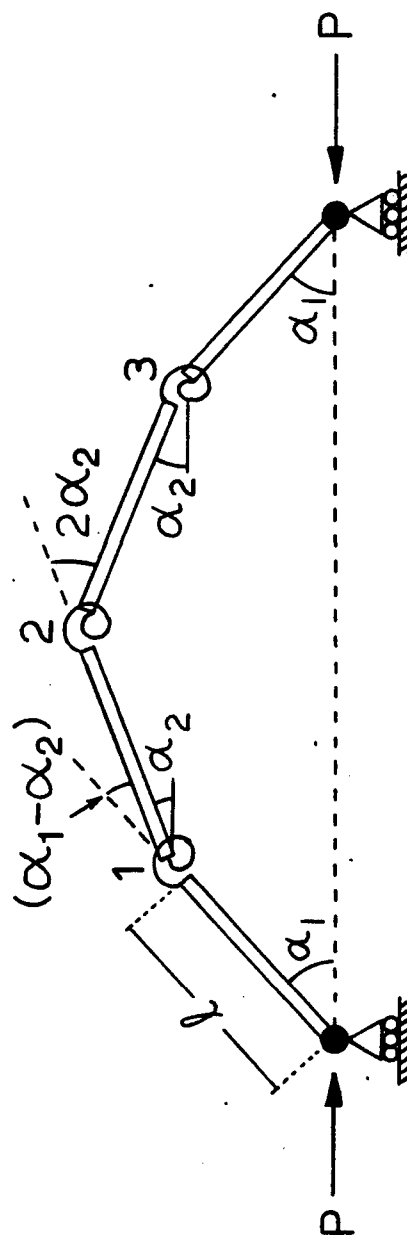


Figure A1.1. Postbuckled shape of link-hinge chain with 4 links.

The chain must be in equilibrium with respect to all rotations. Therefore, equilibrium for the chain shown in Figure A1.1 occurs when:

$$\frac{\partial V}{\partial \alpha_1} = 2(k - P\ell)\alpha_1 - 2k\alpha_2 = 0 \quad (A1.7)$$

$$\frac{\partial V}{\partial \alpha_2} = -2k\alpha_1 + 2(3k - P\ell)\alpha_2 = 0$$

The buckling loads P are obtained from the nontrivial solution of (A1.7). This solution is given by:

$$\begin{vmatrix} (k - P\ell) & (-k) \\ (-k) & (3k - P\ell) \end{vmatrix} = 0$$

$$\text{or} \quad P^2 - 4\left(\frac{k}{\ell}\right)P + 2\left(\frac{k}{\ell}\right)^2 = 0 \quad (A1.8)$$

The roots (eigenvalues) of this polynomial are:

$$P = (2 \pm \sqrt{2})\left(\frac{k}{\ell}\right) \quad (A1.9)$$

The critical buckling load is therefore:

$$P_{cr} = (2 - \sqrt{2})\left(\frac{k}{\ell}\right) \quad (A1.10)$$

It can be verified from (A1.7) that this value of P_{cr} gives:

$$\frac{\partial^2 V}{\partial \alpha_1^2} > 0, \quad \frac{\partial^2 V}{\partial \alpha_2^2} > 0 \quad (A1.11)$$

and therefore causes an unstable equilibrium.

It should be noted that a symmetrical buckling pattern was assumed in this analysis. The symmetry of the buckling configuration can be proven by assuming a general shape for the buckled chain and determining the eigenvectors, i.e., the values of α_i , for each eigenvalue or buckling load.

APPENDIX II

APPROXIMATE SHAPE OF LONG LINK-HINGE CHAIN

Referring to Figure 3.7b, it is seen that the slope at hinge i of the curve $v_i = v(x_i)$ that defines the shape of the buckled link-hinge column is:

$$\frac{\Delta v_i}{\Delta x_i} = \tan \alpha_i \quad (\text{A2.1})$$

For small α_i , $\tan \alpha_i \approx \alpha_i$, therefore (A2.1) becomes:

$$\frac{\Delta v_i}{\Delta x_i} \approx \alpha_i \quad (\text{A2.3})$$

Also, it can be seen from Figure 3.7b that

$$\ell \cos \alpha_i = \Delta x_i \quad (\text{A2.4})$$

which, for small α_i , reduces to:

$$\ell \approx \Delta x_i \quad (\text{A2.5})$$

When the number of links p and therefore the chain length is allowed to increase without bound at a fixed link size, the buckled chain configuration will conform exactly to the curve traced by the analytical function $v(x)$. The limit of increasing overall chain length L at fixed link length ℓ is mathematically equivalent to the limit of vanishing link length at fixed overall chain length. Both cases represent the limit of an infinite number of links.

Therefore, in this limit, equation (A2.3) becomes:

$$\lim_{\Delta x_i \rightarrow 0} \alpha_i = \lim_{\ell \rightarrow 0} \alpha_i = \left. \frac{dv}{dx} \right|_{x_i} \quad (\text{A2.6})$$

The derivative of any continuous function $f(x)$ is defined by:

$$\frac{d}{dx} (f(x)) = \lim_{\Delta x \rightarrow 0} \frac{\Delta f(x)}{\Delta x} = \lim_{\Delta x \rightarrow 0} \frac{f(x_i) - f(x_i - \Delta x)}{\Delta x} \quad (\text{A2.7})$$

If $f(x_i)$ is:

$$f(x_i) = \left. \frac{dv}{dx} \right|_{x_i} \quad (\text{A2.8})$$

Then substitution of (A2.8) into (A2.7) yields:

$$\lim_{\Delta x \rightarrow 0} \frac{\left. \frac{dv}{dx} \right|_{x_i} - \left. \frac{dv}{dx} \right|_{x_i - \Delta x}}{\Delta x} = \frac{d}{dx} \left(\left. \frac{dv}{dx} \right|_{x_i} \right) = \left. \frac{d^2 v}{dx^2} \right|_{x_i} \quad (\text{A2.9})$$

Recognizing that:

$$\lim_{\ell \rightarrow 0} \alpha_{i-1} = \left. \frac{dv}{dx} \right|_{x_i - \Delta x_i}$$

and recalling (A2.5) and (A2.6), their substitution of these results into (A2.9) yields:

$$\lim_{\ell \rightarrow 0} \frac{\alpha_i - \alpha_{i-1}}{\ell} = \left. \frac{d^2 v}{dx^2} \right|_{x_i} \quad (\text{A2.10})$$

APPENDIX III
CRITICAL BUCKLING LOADS FOR A COLLECTION OF
LATERALLY INTERACTING LINK-HINGE CHAINS

The chains are assumed to pack in the cross-section of the fiber on a cubic lattice as shown in Figure 3.8. The lattice dimension b is chosen so that the cross-sectional area per chain b^2 is equal to the value determined experimentally from the actual unit cell of each polymer. The elastic foundation is treated as a continuum matrix which surrounds the chains and is not shown in Figure 3.8.

Buckling is assumed to be restricted to one of two planes, either xy or xz , which are geometrically equivalent. The foundation is assumed to be equally stiff in the y and z directions. This assumption imposes a restriction of transverse isotropy on the polymer. If the total effect of lateral bonding is summarized as a continuum, then the foundation stiffness in the extension buckling mode is a function of a single transverse modulus, $E_t = E_y = E_z$; and the stiffness in the shear buckling mode a function of a single longitudinal shear modulus, $G = G_{xy} = G_{xz}$. In reality each polymer chain will buckle in a manner that simultaneously minimizes the chain bending strain energy and foundation strain energy changes.

Rosen postulated that any combination of extension and shear buckling modes will require more energy and therefore higher loads than either of these extremes. Therefore the critical load for the

collection of chains is the lower of the two values predicted for extension and shear mode buckling.

Following reference [68], any buckled configuration of a chain can be described by a single series of sine waves. The lateral deflection of a chain is then:

$$v(x) = \sum_n a_n \sin \frac{n\pi x}{L} \quad (A3.1)$$

The variation in work due to load P acting on a chain that buckles into a shape described by (A3.1) was shown in reference [68] to be:

$$\partial W = \frac{P\pi^2}{4L} \sum_N n^2 a_n^2 \quad (A3.2)$$

The variation in strain energy of a chain that has a bending rigidity $k\ell$ and that buckles into a shape described by (A3.1) is:

$$\partial U_1 = \frac{\pi^4 k\ell}{4L^3} \sum_n n^4 a_n^2 \quad (A3.3)$$

To complete the equation for equilibrium (3.47), the variation in strain energy of the foundation ∂U_2 must be calculated for each of the two buckling modes.

(a) Extension Mode: For buckling within a plane, the extension mode configuration can be depicted as shown in Figure A3.1.

The deformation of the foundation is due solely to normal strains given by:

$$\epsilon_y = \frac{2v}{b} \quad (A3.4)$$

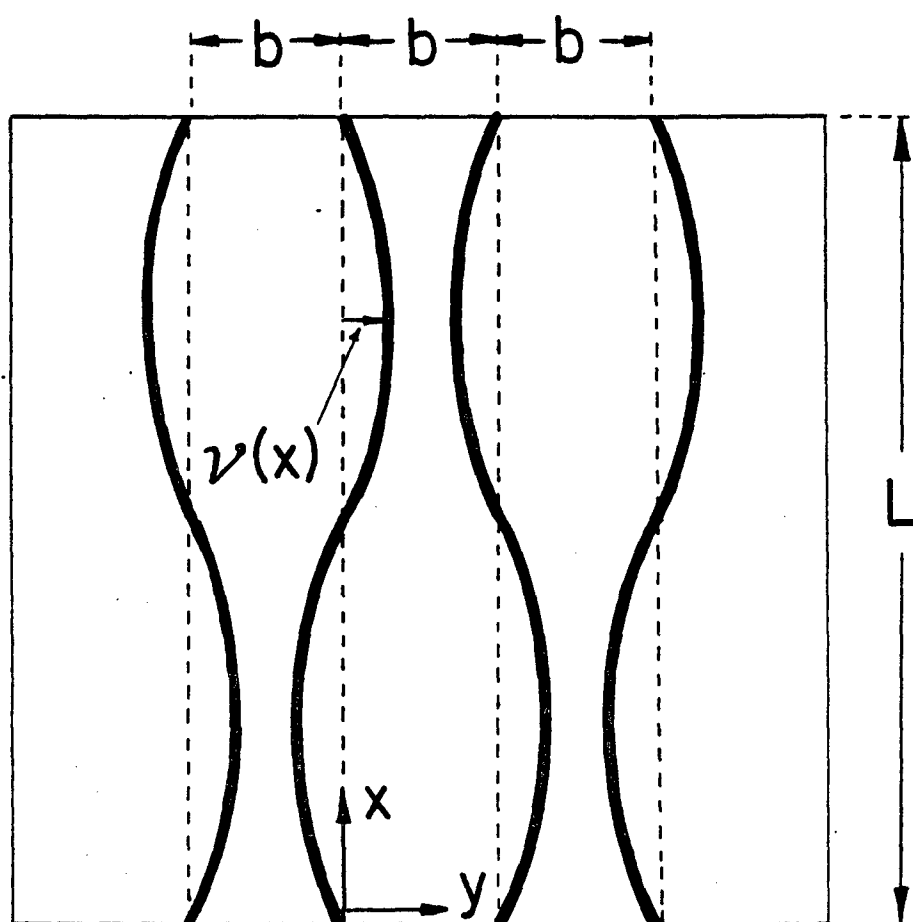


Figure A3.1. Coordinates for extension mode buckling deformation.

The strain energy change is:

$$\partial U_2^e = \frac{1}{2} \int_V \sigma_y \epsilon_y dV \quad (A3.5)$$

and for a linear elastic continuum foundation, $\sigma_y = E_t \epsilon_y$, then:

$$\partial U_2^e = \frac{2E_t}{b^2} \int_V v^2 dV \quad (A3.6)$$

The energy change per chain is therefore:

$$\begin{aligned} \partial U_2^e &= \frac{2E_t}{b^2} \int_{x=0}^L \int_{-b/2}^{b/2} \int_{-b/2}^{b/2} v^2 dz dy dx \\ &= 2E_t \int_0^L v^2 dx \end{aligned} \quad (A3.7)$$

After substitution of (A3.1):

$$\partial U_2^e = E_t L \sum_n a_n^2 \quad (A3.8)$$

The energy balance is given by substitution of (A3.2), (A3.3), and (A3.8) into (3.47) yielding:

$$\frac{P\pi^2}{4L} \sum_n^2 a_n^2 = \frac{\pi^4 k}{4L^2} \sum_n^4 a_n^2 + E_t L \sum_n a_n^2 \quad (A3.9)$$

Solving for P:

$$P^e = \frac{\pi^2 k \ell}{L^2} \frac{\sum_n^4 a_n^2}{\sum_n^2 a_n^2} + \frac{4E_t L^2}{\pi^2} \frac{\sum_n a_n^2}{\sum_n^2 a_n^2} \quad (A3.10)$$

It is shown in reference [68] that ratios of the summations appearing in (A3.10) are minimized when only one arbitrary coefficient

a_n is used. Therefore:

$$p^e = \frac{\pi^2 k \ell}{L^2} (m^2) + \frac{4E_t L^2}{\pi^2} \left(\frac{1}{m^2}\right) \quad (A3.11)$$

where $m=1,2,3,\dots$

The minimum value of P depends on the relative values of $k\ell$ and E_t . If the foundation is stiff relative to the bending rigidity of the chain (i.e., $E_t \gg k\ell$), and the chain is long, then the second term in equation (A3.11) will dominate and large values of m will be required to minimize P . For large values of the integer m , it was shown [68] that:

$$\frac{L}{m} = \pi(k\ell/4E_t)^{1/4} \quad (A3.12)$$

Substitution of this result into (A3.11) gives the relationship:

$$p_{cr}^e = 4\sqrt{E_t k \ell} \quad (A3.13)$$

For the packing arrangement shown in Figure 3.8, the compressive strength estimated for extension mode buckling is then:

$$\sigma_{cr}^e = \frac{p_{cr}^e}{A} = \frac{4\sqrt{E_t k \ell}}{A} \quad (A3.14)$$

where $A = b^2$.

This result is based on the assumption that the integer m (which corresponds to the number of half sine waves the columns buckle into) is large. Rearranging (A3.12) to give:

$$m = \frac{L}{\pi} (4E_t/k\ell)^{1/4} \quad (A3.15)$$

shows that m will take on large values for long chains and for stiff foundations as mentioned earlier.

(b) Shear Mode: The shear mode of buckling within a plane is represented in Figure A3.2. In this case the foundation experiences only shear deformations, so the strain energy change is given by:

$$\partial U_2^S = \frac{1}{2} \int_V \tau_{xy} \gamma_{xy} dV \quad (A3.16)$$

and with $\tau_{xy} = G\gamma_{xy}$ for a linear elastic continuum foundation:

$$\partial U_2^S = \frac{G}{2} \int_V (\gamma_{xy})^2 dV \quad (A3.17)$$

The linear shear strain is defined by:

$$\gamma_{xy} = \frac{\partial u_y}{\partial x} + \frac{\partial u_x}{\partial y} \quad (A3.18)$$

where u_y and u_x are the displacements in the y - and x -directions, respectively. The displacements u_y are the lateral deflections of the buckled chain. Since these deflections are independent of the y -direction and since there are no displacements u_x , (A3.18) reduces to:

$$\gamma_{xy} = \frac{du_y}{dx} = \frac{dv}{dx} \quad (A3.19)$$

Substitution into (A3.16) gives:

$$\begin{aligned} \partial U_2^S &= \frac{G}{2} \int_{x=0}^L \int_{-b/2}^{b/2} \int_{-b/2}^{b/2} \left(\frac{dv}{dx}\right)^2 dz dy dx \\ &= \frac{Gb^2}{2} \int_0^L \left(\frac{dv}{dx}\right)^2 dx \end{aligned} \quad (A3.20)$$

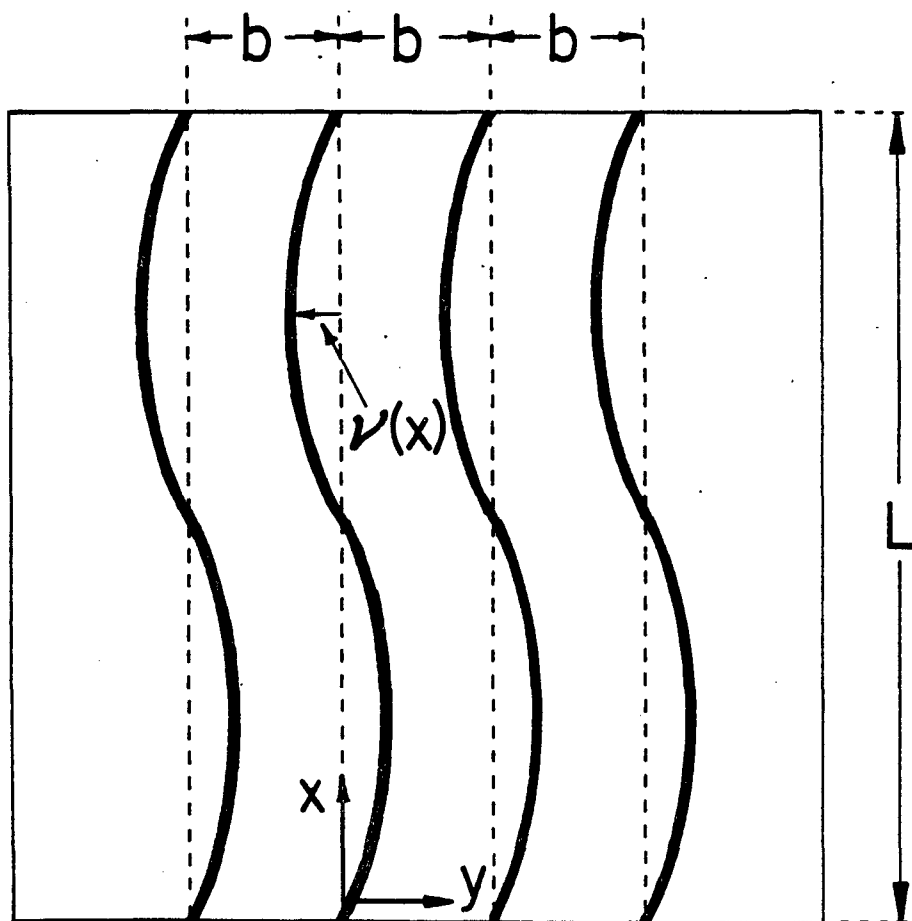


Figure A3.2. Coordinates for shear mode buckling deformation.

Substitution of (A3.1) into (A3.20) results in:

$$\partial U_2^S = \frac{\pi^2 b^2}{4L} G \sum_n n^2 a_n^2 \quad (\text{A3.21})$$

Substitution of (A3.2), (A3.3) and (A3.21) into the equilibrium equation (3.47) and minimizing the ratios of the summations as before leaves:

$$p^S = \frac{\pi^2 k \ell}{L^2} (m^2) + Gb^2 \quad (\text{A3.22})$$

where m is the integer number of half waves of the buckled column. The critical buckling load is simply:

$$p_{cr}^S = \frac{\pi^2 k \ell}{L^2} + Gb^2 \quad (\text{A3.23})$$

Note that the first term in (A3.23) is the buckling load of an unsupported link-hinge chain, a result derived in Section 3.4. The additional load required to overcome the support given by the foundation is proportional to the shear stiffness of the foundation. Because the minimum load occurs for $m=1$, the column will buckle in exactly the same pattern as an unsupported chain: a half sine wave.

For long polymer chains, the first term in (A3.23) can be neglected and the critical load is then:

$$p_{cr}^S = Gb^2 \quad (\text{A3.24})$$

and the corresponding predicted compressive strength is simply:

$$\sigma_{cr}^S = G \quad (\text{A3.25})$$

APPENDIX IV
LIST OF PUBLICATIONS

Parts of this dissertation appear in the open literature in the following publications:

1. S.J. DeTeresa, R.S. Porter, and R.J. Farris, "Behavior of an Aramid Fiber Under Uniform Compression," Polym. Comp. 2, 57 (1982).
2. S.J. DeTeresa, S.R. Allen, R.J. Farris, and R.S. Porter, "Compressive and Torsional Behavior of Kevlar 49 Fiber," J. Mater. Sci., 19, 57 (1984).
3. S.J. DeTeresa, R.S. Porter and R.J. Farris, "A Model for the Compressive Buckling of Extended-Chain Polymers," J. Mater. Sci., accepted: May 1984.